To the Graduate Council:

I am submitting herewith a dissertation written by E-Wen Huang entitled "Fundamental Mechanical-behavior Studies of Annealed and Nano-particle-strengthened Nickel-based Alloys Using In-situ Neutron-diffraction Experiments." I have examined the final electronic copy of this dissertation for form and content and recommend that it be accepted in partial fullfillment of the requirements for the degree of Doctor of Philosophy, with a major in Materials Science and Engineering.

Dr. Peter K. Liaw, Major Professor

We have read this dissertation
and recommend its acceptance:

Dr. Hahn Choo

Dr. Takeshi Egami

Dr. David C. Joy

Dr. John D. Landes

Accepted for the Council:

Carolyn R. Hodges

Vice Provost and Dean of the
Graduate Council

(Original signatures are on file with official student records)

FUNDAMENTAL MECHANICAL-BEHAVIOR STUDIES OF ANNEALED AND NANO-PARTICLE-STRENGTHENED NICKEL-BASED ALLOYS USING IN-SITU NEUTRON-DIFFRACTION EXPERIMENTS

A Dissertation Presented for the

Doctor of Philosophy Degree

The University of Tennessee

E-Wen Huang

December 2009

Copyright© 2009 by E-Wen Huang
All rights reserved

ACKNOWLEDGEMENT

I would like to thank Dr. Peter K. Liaw, my primary adviser, for continually helping and teaching me in all perspectives these years. I am grateful for Dr. Takeshi Egami's time, lectures, and instructions. Sincere thanks are given to Dr. Hahn Choo for co-advising me.

I appreciate Dr. Rozaliya I. Barabash's intensive advice and Dr. Wei-Ren Chen's comprehensive guidance at the Oak Ridge National Laboratory. I am grateful for Dr. Yandong Wang's tutoring from the Northeastern University, China.

This research is supported by the National Science Foundation-International Materials Institutes Program. I especially acknowledge the Ludo Frevel Crystallography Scholarship from The International Centre for Diffraction Data. The alloys are provided by the Haynes International Inc.

The completion of this work would not be possible without the help from Dr. Bjørn Clausen with in-situ neutron-diffraction experiments at the Los Alamos Neutron Science Center, Dr. Yang Ren for synchrotron x-ray experiments at the Argonne National Laboratory, and Dr. Yun Liu for small-angle neutron scattering at the National Institute of Standards and Technology. I am thankful for Dr. Ji-Jung Kai's support of the transmission-electron-microscopy experiments at the National Tsing Hua University, Taiwan.

I really thank Dr. Way Kuo, the former Dean of the College of Engineering, for introducing me to The University of Tennessee. I am thankful for the true

friendship with my colleagues and team members, especially Dr. Michael L. Benson, Dr. Gongyao Wang, and Mr. Kyle P. Woods.

Most of all, I would like to thank my parents, Sheng-Lo Huang and Shu-Chen Chuang, and my sister, E-Chu Huang, whose care and support are unlimited of great value.

ABSTRACT

This dissertation addresses two issues concerning the fundamental mechanical behavior of the nickel-based superalloys: (1) the deformation mechanisms and (2) the nano-precipitate-strengthening effect. The precipitates are known to fortify the mechanical behavior of the metallic alloys. These precipitates can interact with the matrix upon the applied load. While the precipitation strengthening has been facilitated for many purposes, this research puts forward the mechanistic understanding.

The dissertation considers the thesis that Deformation Mechanisms and Nano-precipitate Strengthening and their effects on the microstructure are central to the mechanical behavior of nickel-based superalloys.

The experimental methods employed in this research are in-situ neutron-diffraction measurements, in-situ thermal characterization, ex-situ small-angle neutron-scattering, and electron microscopy experiments. The microscopic structural information obtained from the diffraction profiles is compared with the electron-microscopy images to be complementary to each other. The microscopic features are connected with the macroscopic states, such as the applied stresses and temperature evolution to bridge the understanding of the bulk property.

This dissertation assumes that the macroscopic-material responses are the convolution of two contributions: the linear-elastic contribution and the plasticity-induced intra/inter-granular contribution. Within the context of this analysis, the mechanistic understanding of the deformation of the alloys is presented.

TABLE OF CONTENTS

Chapter 1: Introduction…… 1

1.1. Materials…… 3

1.2. Motivation …… 4

1.3. Outline of the Research…… 5

Chapter 2: Literature Review…….. 7

2.1. Linear-elasticity Behaviour……... 7

2.2. Dislocations in Solids and Plastic Deformation…… 10

2.3. Microstructural Evolution in the Plastically-deformed Materials…… 15

2.4. Precipitation-strengthened Nickel-based Superalloys……... 16

2.5. Diffraction Measurements and Peak-profile Analyses…….. 18

2.6. Small-angle Neutron Scattering for Nano Precipitates……..…… 22

Chapter 3: Slip-system-dependent Dislocation Study of the Annealed Single-phase Alloy under Monotonic Tension…… 27

3.1. Introduction…….……. 28

3.2. Experimental Procedures…..…….. 29

3.3. Results…….. 33

3.4. Discussion……. 42

3.5. Summary……... 45

Chapter 4: Tensile and Cyclic Loading Effects on the Annealed Single-phase Alloy……. 47

4.1. Introduction..…….. 47

4.2. Experimental Procedures……... 50

4.3. Neutron-data Analyses…… 53

4.4. Results…… 57

4.5. Discussion..…… 62

4.6. Summary…….. 68

Chapter 5: Fatigue-induced Reversible/Irreversible Structural-transformation Study of the Annealed Single-phase Alloy Using Combined In-situ Neutron-Diffraction and Thermal Characterization….. 69

5.1. Introduction…….. 70

5.2. Experimental Procedures…….. 72

5.3. Results…….. 74

5.4. Discussion……. 90

5.5. Summary……... 98

Chapter 6: The Precipitation-strengthened Aged Alloy under Tension Deformation……...…… 100

6.1. Introduction…….. 101

6.2. Materials……... 102

6.3. Experimental Results and Discussion...……... 103

6.4. Summary…….. 113

Chapter 7: Low-cycle-fatigue Experiments on the Aged Alloy…..…… 114

7.1. Introduction…….. 114

7.2. Experimental Procedures…….…. 117

7.3. Results and Discussion……. 119

7.4. Summary…….. 128

Chapter 8: Fatigue-damage Transitions of the Annealed and the Aged Alloys…..……. 129

8.1. Introduction…….. 129

8.2. Results and Discussion...…….…. 130

8.3. Summary…….. 133

Chapter 9: Conclusions……. 134

Chapter 10: Future Work……..……... 139

List of References…….. 141

Appendix……..….. 163

Vita……...……..….. 225

LIST OF TABLES

Table 1-1:	The composition of the HASTELLOY®	164
Table 2.1:	Direction cosines in cubic lattices	165
Table 2-2:	Classification of different diffraction experiments	166
Table 2-3:	Profile-shape functions of profile-fitting programs	167
Table 3-1:	Slip systems in the current study	168
Table 3-2:	Material parameters used in the texture simulation	169
Table 3-3:	The probability of the active slip systems	170
Table 3-4:	The deformation parameters of the specifically-oriented grains	171
Table 5-1:	The stresses of the specific fatigue cycles	172
Table 6-1:	The structural parameters of the nano precipitates	173

LIST OF FIGURES

Figure 1-1: The phase diagram for the precipitation and the transmission-electron diffraction of the aged alloys……...…… 174

Figure 1-2: The mechanical properties as a function of the environmental temperature of the annealed and the aged alloys……... 175

Figure 1-3: The summary of the research plans…….. 176

Figure 2-1: The outline of literature review.…… 177

Figure 3-1: The sketch of the patterned structure with dislocation walls and the randomly-distributed dislocations…….…… 178

Figure 3-2: The lattice strain-stress curves…….. 179

Figure 3-3: Stress-strain curve of the annealed alloy for a monotonic-tension experiment……. 180

Figure 3-4: The simulated inverse pole figures…….……... 181

Figure 3-5: The normalized integrated intensity……..…… 182

Figure 3-6: The selected diffraction profiles……..... 183

Figure 3-7: The dislocation-parameter evolution……..…... 184

Figure 3-8: TEM images obtained from the deformed sample……..…... 185

Figure 3-9: The measured and the simualted lattice-strain …….. 186

Figure 3-10: The schematic of the neutron-diffraction measurements…….…… 187

Figure 4-1: The geometry of the specimen and a schematic view of the neutron-beam path for measurements..…….. 188

Figure 4-2: True stress-true strain curve …….……. 189

Figure 4-3: The measurements of the low-cycle-fatigue experiments within one fatigue cycle ……..…….. 190

Figure 4-4: The synchrotron x-ray diffraction patterns…….……... 191

Figure 4-5: Full-width at half maximum (FWHM) versus $2\pi/d$ for low-cycle-fatigue and monotonic-tension experiments.…….. 192

Figure 4-6: The dislocation-parameter evolution (tension)..... 193

Figure 4-7: The dislocation-parameter evolution (fatigue)……..….... 194
Figure 4-8: Intergranular strains as a function of true stress……..... 195
Figure 4-9: The dislocation-parameter evolution within one fatigue cycle…….…….. 196
Figure 5-1: In-situ measurement configurations……..……. 197
Figure 5-2: The stress-strain curves of the monotonic tension and the seven measurement points within the first fatigue cycle……..... 198
Figure 5-3: The stress evolution at the maximum tension and compression……... 199
Figure 5-4: In-situ temperature measurements……. 200
Figure 5-5: The bulk-parameter evolution…… 201
Figure 5-6: The lattice strain-stress curves of the maximum tension and compression……... 202
Figure 5-7: The P-ratio of the tension and compression……... 203
Figure 5-8: Dislocation-structure development…… 204
Figure 5-9: The dislocation-parameter fluctuation within one fatigue cycle……... 205
Figure 6-1: The Rietveld fitting of the aged alloy…….……... 206
Figure 6-2: The peak-width evolution as a function of the true stress…..... 207
Figure 6-3: The peak-width evolution upon loading and unloading……..... 208
Figure 6-4: The distribution of the closest neighboring precipitates in the aged alloy before the deformation……..... 209
Figure 6-4: The morphology of the aged alloy after the deformation…….. 210
Figure 6-6: The true stress-strain curves of the annealed and the aged alloys…..... 211
Figure 6-7: The SANS intensity distribution of the annealed and the aged alloys…….. 212
Figure 7-1: The geometry of the PXM measurements……. 213

Figure 7-2: The microstructure shown in Laue patterns ……..…... 214
Figure 7-3: The bulk-parameter evolution of the aged alloy upon cyclic loading……... 215
Figure 7-4: The matrix-lattice strain-stress curves of the tension and compression……... 216
Figure 7-5: The nano-precipitate-lattice strain-stress curves of the tension and compression……...……. 217
Figure 7-6: The peak-width evolution of the matrix and the precipitates……. 218
Figure 7-7: The reconstructed pole figures of the PXM measurements……. 219
Figure 7-8: The reconstructed contour map…….. 220
Figure 7-9: The depth-dependent lattice rotations in subdivisions……... 221
Figure 8-1: The cyclic hardening and softening of both alloys…… 222
Figure 8-2: The temperature-difference evolution of both alloys…… 223
Figure 8-3: The fatigue-damage models……...…… 224

Chapter 1: Introduction

The design of advanced metallic alloys for structural applications requires the detailed information about the strengthening mechanisms and property evolution under different types of deformation modes (Olson 1997). The underlying deformation mechanisms depend on the dislocation multiplication and self-organization into meso-scale structures, which strongly influence mechanical behavior (Ashby 1972). The age-hardening effect has been extensively used to improve the mechanical behavior by impeding the dislocation movements in various metal-based structural materials (Ardell 1985). The strengthening mechanism relies on the precipitation of the constituent in some phases other than that of the uniform dispersion. The dislocations are localized and prevented from the continued movement by the precipitates. Logically, it is expected that the structural information of the precipitates is a key element in determining the age-hardening phenomenon to optimize the material performance.

Moreover, it is not a trivial task to determine the microscopic mechanism of the plasticity, considering the texture development with the microstructure evolution. The main objective of the dissertation work is to provide the deformation mechanisms and experimental methods to study the mechanical behavior of the alloys. The structural information is investigated, using neutron-diffraction and scattering techniques. Complementary modelings on diffraction-profile and scattering-intensity analyses are developed in order to quantify the experimental results. Electron

microscopy is applied to complement the diffraction and scattering investigations in reciprocal space.

Intellectual Merit: This research explores the mechanical behavior of annealed and nano-precipitate-strengthened alloys under different modes of deformation, including monotonic tension and cyclic loading. The present study of the nano-precipitate-strengthened alloys will (i) develop a novel approach to examine the mechanical behavior of alloys, (ii) further the fundamental understanding of the deformation mechanisms of the alloys, and (iii) promote the application of the alloys.

Broader Impacts: The dissertation work contributes to the fundamental knowledge in the growing demands on diffraction and scattering studies of materials behavior. In particular, the diffraction-peak-profile analyses for the dislocation activities and the phenomenological-statistical model on fitting the small-angle neutron scattering intensity for the structural information in a solid state are developed. Specifically, the deformations of the precipitates are investigated by incorporating the evolution of the matrix in order to properly understand the particle-strengthening effects on bulk properties. Therefore, the dissertation provides the useful information for the materials-research society, especially in the area of the mechanical behavior of the structural materials using diffraction and scattering techniques.

1.1. Materials

Corrosion-resistant nickel-based superalloys are widely used in engineering applications because of their strength and excellent resistance to a wide variety of corrosive environments (Sato *et al.* 2006). For instance, a newly-developed HASTELLOY® C-22HS™ , obtained from the Haynes International, Inc., has been used in important infrastructures, such as the metallic lining in the lower Colorado river power plant and the mixed waste incinerator system at the Los Alamos National Laboratory (HASTELLOY Manual 2005). The composition is shown in Table 1-1 (Table 1-1 and all the following tables and figures can be found in the Appendix).

After a hot-rolling process, the alloy was mill-annealed at 1,080^{o}C. In the mill-annealed condition, the alloy is in a face-centered-cubic (f.c.c.) structure with a grain size about 90 μm. A two-step heat treatment initialized by a 16-hour heat treatment at 705 ^{o}C, followed by a furnace cooling at 605 ^{o}C for another 32 hours (Lu *et al.* 2007), is applied for the precipitation process. The process is detailed in Figure 1-1. The melting point is 1,310 ^{o}C, which suggests that the precipitates are generated in a solid-state solution during the heat treatment. Arya *et al.* (2002) reported that the Ni–Mo alloys exhibit the presence of several competing superlattices during the evolutionary stages of ordering as shown in Figure 1-1.

Among these competing phases, Lu *et al.* (2007) reported that Ni_2(Cr, Mo)-phase precipitates can double the mechanical performance with the precipitates embedded in the f.c.c. matrix from the age-hardening heat treatment. Before the precipitation, the 0.2% yield strength of the alloys at room temperature is 376 MPa

and becomes 690 MPa at room temperature after the precipitation. Moreover, the elongation reaches 45% at room temperature and 50% at 600 ^{o}C (Figure 1.2). It is important to study the mechanical behavior under different deformation modes of the aged alloy, which doubles the strength, while keeping the excellent ductility for future applications and new alloys design (HASTELLOY Manual 2005).

1.2. Motivation

Nickel-based alloys are the most fascinating heat-resistant alloys, which are used in industrial reactors and aircraft engines (Sato *et al.* 2006). The understanding of the fatigue behavior of the nickel-based alloys is important for both of the daily applications and the scientific research. Because many of the safety factors designed for the superalloys are based on the engineering-phenomenal equations, it is necessary to understand the fundamental physics governing the mechanical behavior at the atomic level.

The dissertation addresses the crystal structures and physical processes governing the mechanical behavior of annealed single-phase and nano-precipitate-strengthened nickel-based alloys. The present research examines the morphology of the microstructures, the nano precipitate, and their influences on the bulk behavior of the alloys. The current work applies a combination of various scattering techniques, electron microscopy, statistical mechanics, and computational modeling. Ensemble averages are studied via in-situ neutron-diffraction and ex-situ small-angle neutron-scattering (SANS) experiments. The thermal-mechanical behavior of the alloy is

examined by in-situ temperature and stress-strain measurements to compare with the scattering results. The focus of the dissertation is the fatigue behavior of the annealed and the nano-precipitate-strengthened alloys.

The age-hardening effect, one of the most widely used means to strengthen alloys, has been extensively employed to develop various metal-based structural materials for innumerable industrial applications. The strengthening mechanism relies on precipitation. The morphology of the precipitates and their spatial arrangement in the embedded matrix are two key elements in deciding the mechanical performance. The deformation mechanisms of this type of the alloy need to be studied in order to understand the interactions between the precipitates and the matrix.

The dissertation research of the fatigue behavior of the alloys, ranging from bulk properties to their atomic structures, is a new interdisciplinary subject, incorporating aspects of physics and materials science for the future design of the structural materials. To sum up, this dissertation takes the advantages of the nondestructive property and the superior statistics offered by the in-situ neutron-diffraction experiments to study the deformation mechanisms and to identify the diffraction patterns, which can give rise to different deformation consequences.

1.3. Outline of the Research

The research plans include monotonic and cyclic deformation on the annealed and aged alloys (Figure 1-3). In-situ neutron diffraction experiments are complemented by other expeiments. The experimental methods and data-analysis

techniques are developed to address the growing demands by studying mechanical behavior of materials using diffraction and scattering. The research results are as follows: [1] diffraction-peak-profile and small-angle neutron-scattering intensity analyses, [2] the plasticity of the alloys under monotonic loading, [3] the precipitation-strengthening mechanisms, [4] the fatigue mechanisms of the annealed and the nano-precipitate-strengthened alloys, and [5] a newly-developed factor, lattice-strain anisotropy (P-ratio), for examining the irreversible fatigue damage.

Chapter 2: Literature Review

Mechanical behavior of materials is one of the most important subjects for the civilization. A central principle in understanding the mechanical behavior is the structure-mechanical property paradigm, which proposes a direct connection between the structures on different scales within a material and its properties (Hansen 2001). The increasing capabilities of the applied diffraction/scattering techniques advances the systematic examination with the connection between the microscopic states to the bulk-mechanical behavior (Egami and Billinge 2003; Hutchings *et al.* 2005; Will 2006).

In this Chapter, the material responses subjected to mechanical deformation are reviewed. This Chapter will also present how to apply the neutron-diffraction and small-angle neutron-scattering experiments to study the mechanical behavior. The literatures reviewed herein are summarized in Figure 2-1.

2.1. Linear-elasticity Behaviour

In 1678, Robert Hooke published "*Ut tensio, sic vis*," which means "*As the extension, so the force*. (Hertzberg 1983)" This classic paper characterized a linear relationship between the stress and strain. The linear stress-strain relationship, Hooke's law, presents the strength of interatomic forces between adjacent atoms. The equilibrium distance between the adjacent particles is associated with a balance of the energies of repulsion and attraction. It is found that if the load is removed before the

fracture, the corresponding strain would retrace itself along the same linear path. The reversible nature of strain is the basic element of the elastic strain.

Hooke's law can be generalized to account for multiaxial loading directions. As a stress is applied in one direction (say the Y-direction) of the materials, it could yield strains in the X, Y, and Z-directions. Hence

$$\varepsilon_{yy} = \frac{\sigma_{yy}}{E} \tag{2-1}$$

$$\varepsilon_{xx} = \varepsilon_{zz} = \left(-\frac{\upsilon \sigma_{yy}}{E} \right). \tag{2-2}$$

σ_{yy} is the stress acting normal to the Y plane and in the Y direction. ε_{xx}, ε_{yy}, and ε_{zz} are corresponding strains in orthogonal directions, υ is Poisson's ratio, and E is modulus of elasticity. The stiffness is analogous to the Young's modulus. When the elastic constants vary as a function of the crystallographic orientation, the strains in each direction subjected to three normal and six shear stress components, can be written as

$$\begin{aligned}
\varepsilon_{xx} &= s_{11}\sigma_{xx} + s_{12}\sigma_{yy} + s_{13}\sigma_{zz} + s_{14}\tau_{yz} + s_{15}\tau_{zx} + s_{16}\tau_{xy} \\
\varepsilon_{yy} &= s_{21}\sigma_{xx} + s_{22}\sigma_{yy} + s_{23}\sigma_{zz} + s_{24}\tau_{yz} + s_{25}\tau_{zx} + s_{26}\tau_{xy} \\
\varepsilon_{zz} &= s_{31}\sigma_{xx} + s_{32}\sigma_{yy} + s_{33}\sigma_{zz} + s_{34}\tau_{yz} + s_{35}\tau_{zx} + s_{36}\tau_{xy} \\
\varepsilon_{xy} &= s_{41}\sigma_{xx} + s_{42}\sigma_{yy} + s_{43}\sigma_{zz} + s_{44}\tau_{yz} + s_{45}\tau_{zx} + s_{46}\tau_{xy} \\
\varepsilon_{yz} &= s_{51}\sigma_{xx} + s_{52}\sigma_{yy} + s_{53}\sigma_{zz} + s_{54}\tau_{yz} + s_{55}\tau_{zx} + s_{56}\tau_{xy} \\
\varepsilon_{xzx} &= s_{61}\sigma_{xx} + s_{62}\sigma_{yy} + s_{63}\sigma_{zz} + s_{64}\tau_{yz} + s_{65}\tau_{zx} + s_{66}\tau_{xy}
\end{aligned} . \tag{2-3}$$

Where s_{ij} is elastic compliances and τ_{ij} is stress acting on ***I*** planes and in the ***J*** direction. The reversibility of elastic strains leads to the fact that $s_{ij} = s_{ji}$. As a result of symmetry considerations, the elastic compliance matrix for cubic crystals reduces to

$$s_{ij} = \begin{pmatrix} s_{11} & s_{12} & s_{12} & 0 & 0 & 0 \\ s_{12} & s_{11} & s_{12} & 0 & 0 & 0 \\ s_{12} & s_{12} & s_{11} & 0 & 0 & 0 \\ 0 & 0 & 0 & s_{44} & 0 & 0 \\ 0 & 0 & 0 & 0 & s_{44} & 0 \\ 0 & 0 & 0 & 0 & 0 & s_{44} \end{pmatrix}. \tag{2-4}$$

For the cubic crystals, the modulus of elasticity in any given direction can be described as Equation 2.5 in terms of three independent elastic constants and the direction cosines of the crystallographic direction as following

$$\frac{1}{E} = s_{11} - 2\left[(s_{11} - s_{12}) - \frac{1}{2}s_{44}\right]\left(l_1^2 l_2^2 + l_2^2 l_3^2 + l_1^2 l_3^2\right). \tag{2-5}$$

l_1, l_2, and l_3 are direction cosines, such that $l_1 = \cos(\alpha) = \frac{v \cdot \hat{x}}{|v| \cdot |\hat{x}|}$. The direction cosines for principal directions in a cubic lattice can be referred to Table 2.1, as shown in the Appendix.

Later on, the neutron-diffraction results are interpreted in terms of the lattice-strain evolution, based on the generalized Hooke's law discussed above.

The state of solids can be described by the strain (ε) or stress (σ) and temperature (T). Under the Hooke's law, the stress- or strain-temperature relation can be derived from the laws of thermodynamics (Stanley and Chan 1985) as

$$\Delta T = \left(-K \frac{ET}{1-2\upsilon} \Delta\varepsilon \right) \text{ or} \tag{2-6}$$

$$\Delta T = \left(-KT\Delta\sigma \right). \tag{2-7}$$

T is the absolute temperature of the current state, and K is a material constant [$K = \overline{\alpha} / \rho C_V$]. Other parameters, reported from the Manual of the HASTELLOY® C-22HS™ alloy (2005), include $\overline{\alpha} = 11.6 \mu m / m - {}^0C$, the coefficient of the linear thermal expansion, $\rho = 8.6 g / cm^3$, the mass density, and $C_V = 412 J / kg - {}^0C$, the specific heat at a constant volume. $\Delta\varepsilon$ is the change of the strain, and $\Delta\sigma$ is the change of the stress. υ is the Poisson's ratio. In Equations 2-6 and 7, the temperature response is negatively proportional to the change in the stress or strain states of a homogenous elastic solid.

2.2. Dislocations in Solids and Plastic Deformation

The primary interests of the dissertation research focus on the thermo-mechanical properties of the materials. Though many properties of the materials involve complex interactions of different defects, the initial considerations of such defects will be carried out on the basis of their underlying arrangements, such as the

dislocations (Ashby 1972; 1989; Hansen 2001). With these features, the diffraction profiles can be obtained with the statistical models of the convoluted structural and form factors (Ungar *et al.* 1993; 1999; Barabash and Krivoglaz 1982; Balzar *et al.* 2004).

For a perfect crystal, the structure is treated to be perfectly continuous-repeating units. The deviations from the regularity can be thought of as defects. The microstructures with the defects can manipulate the strengths of the materials (Haasen 1996).

In this dissertation, the microstructure represents the perspectives to conclude both the bulk and the microscopic mechanical properties. In this setting, we broaden the perspectives to investigate the microstructures and address its functions. More specifically, the investigated alloys are polycrystalline, with grains of many different orientations meeting to form an array of grain boundaries. In addition, the aged alloy contains the precipitates, which influence the mechanical properties of the alloys. The material's microstructure must account for the dislocations which populate the grains themselves.

In a broad term, the dislocations play the main role of the permanent deformation of crystalline solids largely because the dislocations are the primary means of the plastic deformation (Dieter 1986). The attempt to monitor such plasticity can be based upon different methods. At the smallest scales, the morphology can be observed by the atomic structure of dislocations via transmission-

electron microscopy (TEM) (Kuhlmann-Wilsdorf 1999). It can also suggest other features, such as the flow stress as the bulk property (Hertzberg 1983).

The following literature review is to introduce the essential information used in dealing with the plastic deformation in crystalline solids. The plasticity represents multiple dislocations activities interacting with other microstructures, such as substitutional impurities, grain boundaries, and inclusions.

One of the examples for the plastic deformation in crystals is the stress-strain curve (Hertzberg 1983). Once the stress exceeds the elastic limit, the stress-strain curve of the permanently-deformed crystal deviates from the linearity. When the crystal is subsequently unloaded, there is a residual plastic strain. The crystal is hardened accordingly. With the deformation, there is a large dependence of that stress on a material's cold working. The dependence of the yield stress on a material's grain size is revealed in the Hall-Petch relation, which notes that the yield stress (σ_y) with the grain size (d) as (Haasen 1996)

$$\sigma_y \propto d^{-1/2}. \tag{2-8}$$

Finally, depending upon the extent of prior working of a material, the preexisting dislocation density can vary the yield point on the stress-strain curve.

However, there are more subtle structural changes, such as slip and shearing mechanisms for dislocations. Each dislocation carries an elementary unit of lattice translation in terms of the Burgers vector. If such dislocations cross the surface in the

same vicinity, the surface shows the slip traces. The shearing mechanism relates how slip is transmitted from favorably oriented grains to their less favorably oriented partners (Haasen 1996). In single crystal tensile tests, the loading axis is oriented with respect to the crystal at an angle, ϕ, relative to the normal of the slip plane. Similarly, the angle, λ, characterizes the relative orientation of the loading axis and the slip direction within the slip plane. These relative orientations are changed incrementally to a certain critical value. The resolved shear stress (τ_{rss}) can be found by projecting the traction vector on the plane, with normal, $\boldsymbol{n}$, onto the slip direction as Schmidt factor:

$$\tau_{rss} = s \cdot \sigma n = \sigma_0 \cos\phi \cos\lambda, \tag{2-9}$$

where $\boldsymbol{s}$ is a unit vector in the slip direction and σ_0 is the magnitude of the externally applied tensile load (Dieter 1986).

The crystal, slipped relatively to another crystal, is determined by the periodicity of the underlying lattice. Since dislocations are often primary agents of plasticity, it is necessary to consider the geometric features implied by their presence. The atoms shift relative to each other by the Burgers vector. The Burgers vector from the existence of a series of lattice invariant shears and leaves the overall lattice unchanged. In addition, a dislocation can also be thought of cutting the crystal over some part of the slip plane. Dislocations translate and rejoin the cut region on the slip plane

Although dislocations are independent of the crystal-structure type, the effects of the dislocations on the stresses depend upon the crystallographic features of different materials (Humphreys 2001).

From the perspective of the above discussion, the key objective is the slip system. The notion of a slip system refers to the slip-plane normal and the slip direction. The basic idea is that the net plastic strain may be thought of as an accumulation of the contributions arising on all of the relevant slip systems.

The dislocations-mediated plastic deformation is characterized by two crystallographic features: the slip plane with a vector (n) and the Burgers vector (b), which characterize the direction of slip associated with the passage of a given dislocation.

For the dislocation line itself, we can consider the local tangent vector (ξ). The angle between the Burgers vector and this local tangent is another important character of a given dislocation. The simplest dislocations are those in which the dislocation line is either parallel to, $b//\xi$, (a screw dislocation) or perpendicular to (an edge dislocation) the slip direction (Hertzberg 1983).

In face-centered-cubic (f.c.c.) metals, the dominant slip system is that in which slip occurs along <110>-type directions with corresponding Burgers vector $b=(a_0/2)\langle 110\rangle$ and is associated with {111}-type planes (Haasen 1996). The nature of the crystalline slip is described as the followings. First, the slip planes are those of closest packing. Secondly, the direction of slip is that along which the packing is again closest, which agrees with this empirical observation based on the energetic

arguments (Dieter 1986). Because of the high symmetry of cubic crystals, there are a wide variety of equivalent slip systems. In the f.c.c. case, each of the four {111} planes supports three distinct Burgers vectors, resulting in a total of twelve distinct slip systems (Haasen 1996).

2.3. Microstructural Evolution in the Plastically-deformed Materials

The hardening mechanisms on the material can be controlled by the microstructures. From a mechanistic perspective, the creation of obstacles to the dislocation motion can enhance the strengthening mechanisms. These obstacles provide additional resisting force above the intrinsic lattice friction. The strengthening mechanisms are revealed macroscopically through a larger flow stress (Dieter 1986). Hence, it is important to examine how the microstructures create the obstacles to the motion of the dislocations.

The cold work on the material can be present by the microstructural changes at the dislocation level. The increase in the dislocation density can alter the mechanical properties. From the basic observation of generic crystalline solids, the polycrystalline materials are composed of many different grains, each with a particular crystalline orientation and separated by grain boundaries (Humphrey 2001). The grains and the associated boundaries make up the polycrystalline microstructure, such as the grain size and patterned-dislocation structures (Barabash and Krivoglaz 1982). In a worked material, the microstructure is characterized by a series of heavily dislocated grains (Ashby 1989).

Indeed, the control of the relative proportions of different phases within a material is one of the primary ways that the microstructural control is exercised. For example, there is an application of the precipitation due to an overabundance of some foreign atoms upon heating. With increasing the temperature, the likelihood of diffusion increases, and the atoms can organize into precipitates (Ardell 1985). With the increasing time at elevated temperatures, the size of such precipitates can increase due to coarsening effects.

2.4. Precipitation-strengthened Nickel-based Superalloys

If there is a supersaturation of substitutional impurities, subsequent annealing will lead to the formation of precipitates (Hansen 2005). The precipitates can act as the obstacles to the dislocations.

Specifically, the equilibrium of two-phase coexists between the matrix phase and a second phase. The presence of such second-phase particles makes itself known through a substantive change in the mechanical properties of the material. Observations on precipitation hardening make it evident that the key microstructural features in this context are the mean particle radius and the volume fraction of such precipitates (Dieter 1986). In particular, the variation in the flow stress is a function of particle size. The particle-cutting mechanism is dominant at small radii. The Orowan process is easier at large particle radii (Hassen 1996).

The age-hardening effect, one of the most widely used means for strengthening alloys, was discovered by Wilm (1911). Since then, it has been

extensively used for developing various metal-based structural materials for innumerable industrial applications (Olson 1997; Hornbogen 2001; Hollingsworth 2002). The strengthening mechanism relies on the precipitation in some phases other than that of uniform dispersion. The dislocations are localized and prevented from continued movements by the strain field introduced by the lattice mismatch between the precipitates and the homogeneous matrix. The morphology of the precipitates and their spatial arrangement in the embedded matrix are two known key elements in deciding the mechanical performance.

Nickel-based superalloys have undergone the extensive development in terms of the alloy chemistry and single-crystal processing technology (Gell and Duhl 1986) and are used as structural components for the high-temperature applications and chemical resistance to oxidation, such as the turbines. These superalloys are known for their excellent high-temperature strength and creep resistance.

Nickel-based superalloys are strengthened to impart resistance to the dislocation motion. The microstructure consists of the precipitates of an intermetallic compound (γ') with a stoichiometric composition Ni_3(Al, Ti), in a nickel-rich nickel-chromium solid-solution matrix (γ). The matrix phase has a space group of $Fm\bar{3}m$, while that of the γ' phase is $Pm\bar{3}m$, and involves ordering of the (Al, Ti) atoms. The γ/γ' interface is often coherent. Because the lattice constants of the two phases may be different, coherent γ' particles can have associated strain fields. These strain fields can interact with dislocations so as to inhibit the dislocation motion. Thus, coherent precipitates generally serve to strengthen the alloy. In some superalloys, the lattice-

constant mismatch is more severe, and the γ/γ' interfaces are semicoherent, thereby relieving some of the strain by the incorporation of dislocations in the particle/matrix interface. Because the geometry of the undeformable precipitates blocks the unimpeded glide of dislocations on *{111}* planes, dislocation motion in the γ channels involves a considerable climb and is necessarily slow, leading to the excellent dislocation creep resistance of the superalloy (Allen and Thomas 1999).

2.5. Diffraction Measurements and Peak-Profile Analyses

The dissertation research focuses on the powder diffraction, which is a powerful nondestructive testing method for determining a range of physical and chemical characteristics of materials. For example, the X-ray diffraction results from the interaction between X-rays and electrons of atoms. Depending on the atomic arrangement, interferences between the scattered X-rays are constructive when the path difference between two diffracted rays differs by an integral number of wavelengths. This selective condition is described by the Bragg equation:

$$2d_{hkl}\sin\Theta_{hkl} = n\lambda. \tag{2-10}$$

λ is the wave length, d_{hkl} is the d-spacing, and Θ_{hkl} the Bragg angle, which is half the angle between incident and reflected beam. hkl describes the Miller indices of each plane (Will 2006).

Three sources of radiation are introduced below: X-rays, synchrotron radiation, and neutrons. The laws of diffraction, i.e., the interference of diffracted beams holds equally well for all radiations. Electron diffraction is not considered here. Furthermore, in this monograph, only structural aspects are considered, which are independent of radiation. The discussion is also limited to coherent and elastic scattering.

X-rays: used in laboratories, where data are collected with sealed X-ray tubes or from rotating anode tubes.

Synchrotron radiation: a beam of charged electrons is strongly accelerated in an electric field. The beam is deflected in magnetic fields. The beam emits a continuous spectrum of X-rays, that is as much as 10^{13} times as brilliant as from sealed X-ray tubes. This radiation is called "synchrotron radiation." The increased brilliance relates to the total energy spectrum (Will 2006).

Neutrons: A neutron is an elementary particle with a finite mass (*m*, about 1.67×10^{-27} *kg*) and spin, without an electron charge. It carries a magnetic moment, and according to *de Broglie* law, the neutrons behave like waves with a wavelength (λ) at the levels of Å and gives rise to diffraction (Lindner and Zemb 2002). Neutron diffraction is based on the nuclear interaction between neutrons and the matters and on magnetic interaction with magnetic moments of the atoms due to its magnetic moments.

The term "powder", as used in powder diffraction, is important. The concept of a powder for a diffraction experiment is that the number and size of the individual

crystallites of the specimen, but not their degree of accumulation. An "ideal" powder for a diffraction experiment consists of a large number of small randomly oriented crystallites (Will 2006). If the number is sufficiently large, there are always enough crystallites in any diffracting orientation to give reproducible diffraction patterns.

Diffraction-peak Intensity and Measurement

Any diffraction is a Fourier transformation from the direct or crystal space into the reciprocal space, yielding intensity data in the reciprocal space. Detectors register intensities *I(hkl)*, which are directly proportional to the squares of the crystallographic structure factors *F(hkl)*. The intensity (*I*) is proportional to $|F|^2$. F is a complex quantity

$$F(hkl) = \sum_j f_j \exp(hx_j + ky_j + lx_j) \tag{2-11}$$

with f_j, the form factor or atomic scattering factor of atom, *j*. *h k l* are the Miller indices and *x y z* is the relative atomic positions in the unit cell. The summation *j* runs over all atoms in one unit cell. Consequently, we observe intensities only at the reciprocal lattice points.

Peak-profile Analyses

The Rietveld method (1967) is very useful for the full pattern profile refinement and the simultaneous crystal structure refinement. This is a least-squares

fit of a (given or known) profile function to the diffraction pattern by minimizing the function:

$$\phi = \sum_i w_i \left(y_i(observed) - y_i(calculated) \right) = Minimum . \qquad (2\text{-}12)$$

The $y_i(observed)$ and the $y_i(calculated)$ are the measured and the calculated intensities, respectively, at each step. The summation index (i) is running over the section of the pattern selected for fitting. The classification of different methods is listed in the Table 2-2.

The profile-shape functions: Three functions are widely used as the Gaussian, the Lorentzian, and the Pseudo-Voigt function. They are listed in Table 2-3 (Will 2006).

In the neutron case, the instrumental factors are dominant, while the X-ray profiles are determined by the size and strain of the particles. Suortti *et al.* (1979) reveals that the true Voigt function, besides extensive mathematical programming, is not useful for structure analytical purposes. It can be successfully used only for a profile, which can be completely resolved. In neutron diffraction, the peak shape is the predominant Gaussian.

Factors, which do influence the line shape, are the crystalline size and microstrain contributions. The crystalline-size broadening produces Lorentzian distribution-type-shaped intrinsic tails in the peak profile, while microstrains produce

Gaussian distribution-type-shaped contributions. Full-width-at-half-maximum (FWHM) values are significantly affected with such samples.

Line broadening: crystalline size, strain, and stress: The important application is the analysis of the profile. The key is microstructure. Polycrystalline materials invariantly contain imperfections that modify the intensity of the Bragg reflections, and also the peak shape, which are concluded in Table 2-3.

The main deviations observed in the profiles are from very small particles and from the strain and stress in the sample. As a general rule, the contribution of a crystalline size is approximated by the Lorentzian function of a width proportional to $1/\cos(\Theta)$. Strain broadening is covered by the Gaussian, which has a width proportional to $\tan(\Theta)$ (Ungar and Wilkins 1989). The determination of a particle size is treated by the Scherrer equation (Will 2006). The Scherrer equation gives a rough estimate of the broadening caused by the crystalline size.

2.6. Small-angle Neutron Scattering for the Nano Precipitates

The small-angle neutron scattering (SANS) approach presents a complementary tool to the microscopy technique. It can provide the nano-scale information via the measurement of the Fourier transform of the spatial correlation function. The collected scattering intensity, *I(Q)*, is presented in reciprocal *Q* space. Therefore, to obtain quantitative real-space information, model fitting is usually required. In the study of nano-precipitates, the data analysis is inevitably compounded

by the thermodynamically-driven polydispersity in the size of precipitates and the anisotropic inter-precipitate interference.

The focus of this dissertation research is to present a model for SANS *I(Q)* to facilitate the application of SANS for the study of precipitation strengthening. A recently-developed nickel-based alloy (Lu *et al.* 2007) with an exceptional mechanical performance due to the presence of the $Ni_2(Cr,Mo)$ precipitates is selected as an example to demonstrate the applicability of our proposed model.

Our methodology is briefly described as follows. In general, *I(Q)* obtained from a system consisted of nonspherical particles can be expressed as

$$I(Q) = \frac{N|\Delta\rho|^2}{V_S} P(Q)\{1 + \beta(Q)[S(Q) - 1]\} + I_{\mathrm{INC}} \qquad (2\text{-}13)$$

where $\Delta\rho$ is the difference in scattering-length densities between the particle and the dispersion medium; V_S, the sample volume illuminated by neutron beam; N, the number of precipitates in V_s; $P(Q)$, the average form factor given by the shape and density profile of particles; $S(Q)$, the effective one-component inter-precipitate structure factor, which is a measure of the inter-particle interference; $\beta(Q)$ the decoupling constant dependent on both the size polydispersity and intra-precipitate density profile (Chen 1986), and I_{INC} the incoherent background.

In the practical implementation of our model fitting, $\frac{N|\Delta\rho|^2}{V_S}$ is treated as a fitting parameter suggested by Pedersen (1993). To minimize the interfacial energy influenced by the strain energy, it is found that $Ni_2(Cr,Mo)$-type precipitates are shaped in the form of polydisperse ellipsoids (Kumar and Vasudevan 1996). Therefore, *P(Q)* is modeled as

$$P(Q) \equiv P(Q,R) = \int P(Q,x,\delta)N(x,R,\delta)dx / \int N(x,R,\delta)dx \qquad (2\text{-}14)$$

where

$$P(Q,R,\varepsilon) = (\frac{4\pi}{3}R^3\varepsilon^2 \int_0^{\pi/2} \frac{3j_1[Q\cdot r(R,\varepsilon,\alpha)]}{Q\cdot r(R,\varepsilon,\alpha)}\sin\alpha d\alpha)^2 \qquad (2\text{-}15)$$

is the form factor of ellipsoids.

$$r(R,\varepsilon,\alpha) = R(\sin^2\alpha + \varepsilon^2\cos^2\alpha)^{1/2} \qquad (2\text{-}16)$$

where R is the long axis, ε is the aspect ratio, and α is the polar angle from 0 to $\pi/2$. The effect of polydispersity is incorporated through the decoupling approximation (Chen 1986) and a standard Gaussian law (Soisson and Martin 2000)

$$N(x,R,\delta)=\frac{1}{\sqrt{2\pi\delta^2}}\exp\left[\frac{-(x-R)^2}{2\delta^2}\right] \qquad (2\text{-}17)$$

where δ is chosen to describe the size distribution (δ^2 is the variance).

It is not innovative to apply the scattering techniques to obtain the structural information of colloidal suspensions. The inter-colloid structure factor, *S(Q)*, from the Ornstein-Zernike (OZ) integral equation, is in virtue of that colloidal particles are equilibrated through Brownian motions, with a suitable closure whose choice is essentially decided by the effective inter-particle interaction, *V(r)*. This approach has been used previously to provide the structural information of the age-hardened alloys, such as Al-Li alloys (Pedersen 1993). However, in our system, the precipitates are formed during a two-step heat treatment initialized by a 16-hour annealing at 705 ^{o}C and followed by a 32-hour cooling at 605 ^{o}C (Lu *et al.* 2007). The melting point is found to be 1,310 ^{o}C. Therefore, the precipitates are generated in a solid-state solution during the heat treatment. Due to the lack of Brownian motion of precipitates, the validity of the OZ-closure approach is, therefore, questionable. To bypass this difficulty, the inter-precipitate structure factor, *S(Q)*, is calculated via a stochastic phenomenological model. It is assumed that precipitates are partially ordered and separated from the nearest neighbors with a preferred distance, *L*, with a deviation measured by the root-mean square denoted by σ. The inter-precipitate structure factor (Giordano *et al.* 1991), *S(Q)*, is expressed as a function of *Q*, *L*, and σ

$$S(Q,L,\sigma) = 2 \cdot \left\{ \frac{1 - \exp\left[-\left(Q^2\sigma^2\right)/4\right]\cos(QL)}{1 - 2\exp\left[-\left(Q^2\sigma^2\right)/4\right]\cos(QL) + \exp\left[-\left(Q^2\sigma^2\right)/2\right]} \right\} - 1 \quad (2\text{-}18)$$

The incoherent scattering, I_{INC}, is mainly determined by the measure of *I(Q)* in a high *Q* region. Based on a gradient-searching nonlinear least-squares fitting method, the SANS data is analyzed with the inclusion of instrumental resolution. It is important to note that the coherent SANS intensity distributions obtained from the alloy can be fitted by the current proposed model uniquely with five parameters: *R, ε, δ, L*, and σ. With that, this proposed model is applied in the current study.

Egami and Billinge (2003), in speaking of the state of research, noted "..... *As we go through our lives, we experience a huge number of events. Experiences themselves, however, would not make us wise. Only after reflecting upon the experience and deducing the essential message from these experiences, do we learn something from life.*" In that vein, the literature review written here has certainly raised some questions for me to answer as my dissertation research.

One of my impressions while reviewing the literatures is that I do appreciate the cleverness of those who developed the fundamental knowledge that I have tried to apply in my research. From the fundamental physics to the elegant engineering, at every turn, I am reminded of why I wanted to study *Materials Science and Engineering* after majoring other subjects.

With that in mind, I am going to undertake my dissertation research in the following Chapters.

Chapter 3: Slip-system-dependent Dislocation Study under Monotonic Tension on the Annealed Single-phase Alloy

As we already discussed in our consideration of slip activities associated with dislocations, this Chapter deals with the annealed alloy subjected to the tensile deformation. We develop a systematic method to analyze the neutron-diffraction results herein and for the rest of the Chapters.

In this Chapter, a combined experimental/computational approach is employed to study slip-system-related dislocation substructure formation during uniaxial tension of a single-phase, face-centered-cubic, nickel-based alloy. In-situ neutron-diffraction measurements were conducted to monitor the peak-intensity, peak-position, and peak-broadening evolution during a displacement-controlled, monotonic-tension experiment at room temperature. The measured lattice strain evolution and the macro stress/strain curve were used to obtain the material parameters required for simulating the texture development by a Visco-plastic self-consistent (VPSC) model. The simulated texture compared favorably with experimentally determined texture results over a range of 0% to 40% engineering strains. The grain-orientation dependency, which was input into the Debye intensity ring, was considered. Grains favorably oriented relative to the two detector banks in the geometry of a neutron experiment were indicated. For the favorably-oriented grains, the simulated slip-system activity was used to calculate the slip-system-dependent, dislocation-contrast factor. The combination of the calculated contrast

factor with the experimentally-measured peak broadening allows assessing the parameters of the dislocation arrangement within the specifically-oriented grains.

3.1. Introduction

In polycrystalline materials, mechanical properties are related to texture, especially under plastic deformation: Slip on specific crystallographic planes during the plastic deformation may produce lattice rotations, and, hence, develop texture. However, Heidelbach comments that it is not a trivial job to reveal the plastic flow, considering the texture development with the microstructure evolution (Heidelbach 2001; Hansen 2001).

Hill's (1965) and Hutchinson's (1970) self-consistent (SC) models have been applied very successfully to simulate the micromechanical behavior of polycrystalline materials (Holden *et al.* 1998) by the lattice-strain evolution based on neutron-diffraction measurements via the Elasto-plastic self-consistent (EPSC) model for several metallic materials (Clausen *et al.* 1997; 1998). The intrinsic assumptions of the EPSC model consider the active inelastic-deformation mechanisms, and, hence, the stiffness/compliance constants are important for simulations (Peng *et al.* 2000; Daymond *et al.* 2000; 2007). The present study extends SC modeling to moderate-to-large deformation strain, considering the grain rotation for describing preferred grain-orientation distributions. In the current work, a visco-plastic self-consistent (VPSC) model is applied to simulate the texture development, based on the measured lattice strains and macro stress-strain responses from a nickel-based alloy. The VPSC model

considers the activity of slip systems and its influence on grain rotation (Kocks *et al.* 1998). The VPSC code used in this study is based on previous work (Wang *et al.* 2001; 2002; 2005). Experimental macro/lattice stress-strain curves are used as an input to simulate the texture and the probability of the active-slip systems from the multiple *hkl*-reflections. Moreover, a peak-width analysis is applied to combine the texture-evolution information for the slip-system-dependent, dislocation-contrast factor. The peak profiles are measured at a time-of-flight (TOF) neutron-diffraction instrument. The contrast factors are used to determine the direction of the active dislocations moving on the slip planes, relative to the specimen-coordinate system of the instrumental environment. This demonstration as in-situ experiment offers new insights about evolving dislocation arrangements and serves as a reference for further dislocation investigations.

3.2. Experimental procedure

Materials and In-situ Neutron Experiments

The HASTELLOY® C-22HS™, a nickel-based alloy, (Ni-21Cr-17Mo in weight percentage) was selected as the sample material. The alloy was annealed to dissolve most precipitates, and showed a texture-free condition from previous neutron-diffraction measurements (Huang *et al.* 2007) in axial and transverse directions. The average starting grain size was about 90 μm, and the texture-free condition made the alloy a good specimen to interpret peak-refinement results: There were no initial texture and second-phase precipitates. Lu *et al.*'s transmission-

electron-microscopy (TEM) study (2007) confirmed that the alloy had a single-phase f.c.c. structure. The room-temperature, in-situ neutron measurements were conducted with the Spectrometer for MAterials Research at Temperature and Stress (SMARTS) beamline of the Los Alamos Neutron Science Center (LANSCE) (Bourke *et al.* 2002). The gauge volume was 120 mm^3 for the measurements of the monotonic tension. The strain rate was 0.001 per second.

Neutron-Data Analyses

The neutron-diffraction profiles were refined by the General Structure Analysis System (GSAS) (Larson and Von Dreele 2004) for investigating the peak-position, intensity, peak profiles and width, respectively. A pseudo-Voigt function (GSAS function #3) was fit to the data and used to distinguish different sources of peak broadening.

The refined peak positions of each *hkl* were calculated during the evolution of lattice strain (ε_{hkl}), based on the change in the *d*-spacing (d_{hkl}) as a function of the stress, relative to the initial *d*-spacing (d^0_{hkl}) as shown in Equation 3-1

$$\varepsilon_{hkl} = \frac{d_{hkl} - d^0_{hkl}}{d^0_{hkl}} \tag{3-1}$$

The lattice-strain evolution was used as an input for fitting the compliance within the elastic region, for the VPSC simulations.

The peak intensity was fitted for the individual *hkl* peaks. The normalized intensity evolution as a function of stress was calculated using Equation (3-2) to monitor the texture development through the tensile test, which was further used to compare with the VPSC-simulated texture development.

$$I_{hkl} = \frac{I^{deformed}{}_{hkl}}{I^{0}_{hkl}} \tag{3-2}$$

The peak-width was decomposed into the Gaussian and Lorentzian broadening components as a full-width half-maximum (FWHM). The profile shape functions used in profile fitting programs are shown in Equations (3-3) and (3-4) for Gaussian and Lorentzian, respectively.

$$G = I_0 \exp\left(-\ln 2 \left(\frac{2\Theta - 2\Theta_0}{w} \right)^2 \right) \tag{3-3}$$

$$L = I_0 \left(1 + \left(\frac{2\Theta - 2\Theta_0}{w} \right)^2 \right)^{-1} \tag{3-4}$$

Here I_0 is peak intensity; w is half FWHM, and 2Θ is the peak position.

Model of Dislocation Arrangements

We assume the formation of a hierarchical dislocation structure in the plastically-deformed material when some part of a dislocations group within dislocation walls and some part remain randomly distributed. The formation of the hierarchical dislocation structure in many metallic polycrystalline materials under different deformation has been previously reported (Mughrabi 1983; Levine *et al.* 2006; Kuhlmann-Wilsdorf 1999; Hansen 2005; Nix *et al.* 1985). Similar to Zehetbauer (1993), Schafler *et al.* (2005), and Hughes and Hansen (1993), we consider the formation of the hierarchical dislocation structure with dislocation walls creating certain misorientations/tilt/twist between the neighboring regions of the same grain with some random portion of the dislocation population randomly distributed between the walls. There is practically no misorientation/tilt/twist in the interior. For simplicity, we assume that the dislocation walls are composed from the equidistant-edge-dislocations, and screw dislocations remain randomly distributed in the cell interior, as shown in Figure 3-1. As presented previously (Krivoglaz *et al.* 1970; Barabash and Klimanek 1999; Barabash *et al.* 1999; 2003; Read and Shockley 1950) equidistant-dislocations walls result in the Lorentzian type of broadening. The randomly-distributed or weakly correlated dislocations in the interior result in the Gaussian type of broadening. Further details on the model and calculations are described in the next session.

Transmission-electron microscopy (TEM)

Complementary TEM analyses were performed at 200kV in a TECHNAI 20 electron microscope. Samples for TEM were prepared from a slice cut at 45° to the loading direction to have the slip plane parallel to the surface of the TEM sample.

3.3. Results

Tensile Tests and Fitting Parameters for Simulation

The 0.2% yield strength of the alloy is about 370 MPa. Lattice-strain versus stress curves for *hkl*s: {111}, {200}, {220}, {311}, {331}, {420}, and {422} in loading and transverse directions are shown in Figures 3-2(a) and (b), respectively. The measurements made at 20, 30, 40, 50, 60, 70, 80, 90, 110, and 120 MPa are used to calculate the compliance of the materials for texture simulations. The linearity of the different lattice strain (ε_{hkl}) versus stress curves shown in Figure 3-2 suggests that the alloy intrinsically follows a generalized Hooke's law[31], with {111}, the stiffest plane (Hertzberg 1983), and {200}, the least stiff plane[31] within the elastic region (up to120 MPa).

Visco-Plastic Self-Consistent (VPSC) Simulation

A VPSC model was implemented for estimating the distribution of microstresses and texture evolution for the alloy. The Self-Consistent (SC) approach developed by Hutchinson (1976) was used here with an extension of the Eshelby inclusion tensor to macroscopically anisotropic materials (Lebensohn and Tome

1993). In the model, a total number of 2,592 grains were simulated through the VPSC model (Jia *et al.*2008). The lattice-strain (ε_{hkl}) distribution was simulated at different loading levels. The grains used for modeling are based on the microstructural characteristics obtained from the neutron-diffraction data. The lattice-strain (ε_{hkl}) distribution was simulated at different loading levels. For simplicity, only grain-to-grain interactions existing within the respective phase and the influence of texture on the plastic deformation were considered. The applied method determined the stress needed to give a strain field at each loading level. The strain field was simulated to match the measured lattice-strain distribution for each load. An empirical Voce-hardening rule [Equation (3-5)], was used in the simulation to describe the critical resolved shear stress (CRSS) evolution of individual deformation modes,

$$\tau = \tau_0 + (\tau_0 + \theta_1\Gamma)\{1 - \exp(-\theta_0\Gamma / \tau_1)\}. \quad (3\text{-}5)$$

Here, τ is the instantaneous flow stress, τ_0 and $\tau_0 + \tau_1$ are the initial and final back-extrapolated CRSS, respectively, θ_0 and θ_1 are the initial and asymptotic hardening rates, and Γ is the accumulated plastic shear in the grain. All the parameters were derived by fitting the model to the experimental neutron measurements of the different {*hkl*} lattice-strain evolution and to the laboratorial macroscopic stress-strain curve of the material (Bacmanski and Braham 2004).

The compliances used in the simulations were fitted to the measured lattice-strain (ε_{hkl}) at different load levels within 120 MPa, in the elastic region. Since the

studied material has an f.c.c. structure, 12 cubic slip systems of {111}<110>-type were considered as shown in Table 3-1 (Haasen 1996). The critical resolved stress and the hardening parameter for different slip systems and the elastic constants used in the simulation of this alloy are listed in Table 3-2. In Figure 3-3, the uniaxial monotonic-tensile experiments are presented as a stress-strain curve in open symbols, and the VPSC simulations are shown in a solid line. The simulations agree with the measurements in both the elastic and the plastic regions. The onset of the plastic deformation (370 MPa) is fitted, too. The simulated inverse-pole figures along the loading direction are plotted in Figure 3-4. Figure 3-4(a) demonstrates that the initial texture is practically random. Figure 3-4(b) shows the VPSC simulated texture under the large plastic deformation at 825 MPa using the measured random texture as the input. The simulated results show a preferred texture in {100} and {111} poles, but not in {110} pole.

In-Situ Neutron-diffraction Measurements

To further compare the simulations and experiments, the measured in-situ neutron-diffraction experimental data along the loading direction were used, as shown in Figure 3-5(a). The results are normalized with respect to the intensity at the undeformed status, as calculated by Equation (3-2). The intensity evolution demonstrates that the texture gradually develops as the material plastically deforms. The intensity does not vary before the 0.2% yield strength of about 370 MPa. When the tensile stress reaches 825 MPa, the intensity of the {111} peak increases more

than 1.5 times, comparing to the undeformed state. The {200} peak intensity increases by a factor of ~ 1.5. The {311} has the smallest deviation, and the intensity decreases about 20%, while the {220} almost disappears. These measured, intensity-evolution results demonstrate that {111} and {200} gradually develop the texture along the loading direction as open square in Figure 3-5(b), but {220} intensity disappears from the loading direction. Similar trends are reported from other f.c.c. polycrystalline alloys (Wenk and Grigull 2003), and the effect of the grain orientation on the deformation structure in cold-rolled polycrystalline materials (Liu *et al.* 1998).

The VPSC-simulated results on {111} and {100} at 825 MPa are presented in Figure 3-5(b) as open circle. The simulated texture of both {111} and {100} and there is a stronger {111} texture component than {100}. As a result, there is a qualitative agreement between the simulations and the in-situ neutron measurement.

However, the amplitude of the simulated texture is larger than the measured one at 825 MPa. In Figures 3-5(b), the measured {111} texture increases by 1.5 times, while the simulated one rises by 3 times. The same difference is seen in the {200} texture: The measured intensity rises about 0.5 times and the simulated enlarges almost 1.5 times. The discrepancy between the simulated and the measured intensities shows an overestimation in the texture simulation. The overestimation indicates that the work hardening should be considered with the microstructure evolution, as discussed below.

Microstructure-evolution Estimation via Peak-profile Analyses

Work hardening, which relates to the flow stress, was first derived by Taylor (1938) to link the microstructure evolution to material-mechanical properties under the plastic deformation. Our analysis of the microstructure evolution during the deformation is based on peak broadening observed from the in-situ neutron measurements [Figures 3-6(b)]. The mechanically-induced stored energy in the deformed specimen has been reported to generally derive from the randomly-distributed dislocations, the cellular-dislocation structure, and the heterogeneous elastic-energy contribution of the mean stresses (Biermann *et al.* 1993; Borbely *et al.* 2000; Ungar *et al.* 1989; Will 2006). As a result, changes of the microstructures cause most of the observed peak-broadening. To distinguish the physical contribution to broadening, Γ_{phys}, induced by the microstructure evolution, the instrumental broadening, Γ_{ref}, needs to be taken into account. Γ_{ref} was obtained by measuring the reference sample. The raw data, Γ_{Exper}, shown in Figures 3-6 (a) and (b) were further adjusted to take into account the instrumental broadening ($\Gamma_{phys} = \Gamma_{Exper} - \Gamma_{ref}$). As a result, the physical broadening is more than half smaller then broadening of the raw experimental curves, Γ_{Exper} (Figure 3-6b).

It is known that the randomly-distributed and/or weakly correlated dislocations yield the Gaussian peak broadening (Barabash and Krivoglaz 1983; Krivoglaz 1969; 1996). The dislocation-wall structures, aggregated by the equidistant-edge-dislocations, cause the Lorentzian peak-broadening. Such equidistant-dislocation walls result in local pair wise tilts between the two adjacent

regions of the crystal. We note that stacking faults also result in Lorentzian-type broadening. However staking faults additionally cause distinct anisotropic shift of different (*hkl*) reflections, and their input can be separated from the one caused by equidistant-dislocation-walls (Groma 1998).

In the regions close to the boundaries at distances L, smaller then the distance, h, between the dislocations within the wall ($L < h$), the strain fields from individual dislocations forming the boundary become significant. This is extremely important for the detailed analyses based on the shape of the tails of the peak developed by Ungar *et al* (1989) and Groma (1998). Such analyses of the shape of the tails of diffraction peaks provide the most direct information about the dislocation density. However the signal-to-noise at the tails of the neutron intensity profiles in our measurements was low and the analysis of the shape of the tails could not be reliably used for the analysis of dislocation substructure. For this reason, in the present paper, we used the central part of the peak broadening for the characterization of dislocation parameters, which depends mainly on displacement fields in the regions remote from the wall at the distances exceeding $L>>h$.

For example, assuming a dislocation density of 10^{15} m^{-2} density within the dislocation wall, the distance, h, between the dislocations within the wall becomes h = 30 nm. The strain fields appear in the diffraction profiles at values of $\Delta d^* \cong 0.03$ nm^{-1}. In our experimental data, the region $\Delta d^* \cong 0.03$ nm^{-1} is located in the tails of the peak intensity and does not influence the central part of the peak, which was used for the analysis.

According to Balzar *et al.* (1993; 2004), it is "generally accepted that a Voigt-function approximation for both size and strain broadened profiles is a better model than simplified integral-breadth methods". A detailed description of the profile analysis for neutron time-of-flight (TOF) measurements is given in the GSAS manual (Larson and Von Dreele 2004). To distinguish these two broadening components, similar to the approach of Balzar *et al.* (1993; 2004), the pseudo-Voigt function [Equation (3-6)] is applied. It corresponds to *GSAS* profile function #3.

$$V = \eta L + (1-\eta)G\,, \qquad (0 \le \eta \le 1) \tag{3-6}$$

A parameter (η) is introduced as a variable proportion of pure Lorentzian (L) to pure Gaussian (G), where L and G are defined as Gaussian and Lorentzian peak-widths in Equations (3-3) and (3-4), respectively. The pseudo-Voigt function is fit to each individual {*hkl*} peaks to study these two sources of broadening by *GSAS* with Equation (3-7). Total 7 different (*hkl*) peaks were fitted. For better statistics the results were then averaged over all measured (*hkl*) peaks.

$$\Gamma = \sqrt[5]{\Gamma_g^5 + 2.69269\Gamma_g^4\gamma + 2.42843\Gamma_g^3\gamma^2 + 4.47163\Gamma_g^2\gamma^3 + 0.07842\Gamma_g\gamma^4 + \gamma^5} \tag{3-7}$$

The measured peak width (Γ) is composed by the Gaussian broadening (Γ_g) as shown in Equation (3-8) and Lorentzian broadening (Γ_L), shown in Equation (3-9).

$$\Gamma_g = \sqrt{8(\ln 2)\sigma^2} \tag{3-8}$$

$$\Gamma_L = \gamma \tag{3-9}$$

σ and γ are the standard deviations of the Gaussian and Lorentzian profile components, respectively.

Based on the described model, the dislocation density (n) of the randomly-distributed dislocations from each $\{hkl\}$-reflection can be estimated from the Gaussian peak-width component ($\Delta FWHM_G$), which depends on the Burgers vector (b), the contrast factor (C_r) for randomly-distributed dislocations and/or dislocations with weak correlation, and the d_{hkl}-spacing as presented in Equation (3-10).

$$n_{hkl} \sim \left(d_{hkl} \times \frac{\Delta FWHM_G}{|b| \times C_r} \right)^2 \tag{3-10}$$

The calculation of the contrast factors for a randomly-distributed portion of the dislocation population is performed using the formalism described in the Refs. (Barabash *et al.* 1983; 1999; 2003), and similar to the method developed by T. Ungar group (1989; 1993)

The Lorentzian peak-broadening components ($\Delta FWHM_L$) are used to calculate the equidistant-dislocation-wall spacing (D), as exhibited in Figure 3-6(d), with the contrast factor (C_{EW}) in Equation (3-11),

$$D \sim \frac{\pi C_{EW}}{\Delta FWHM_L} \tag{3-11}$$

where C_{EW} is the contrast factor for the equidistant-edge-dislocation wall. Assuming that all probable slip systems for the f.c.c. material are equally activated, the total dislocation density, *n*, and the distance between the equidistant-dislocation-walls, *D*, were determined using Equations. 3-10 and 11 (Figure 3-7). For the first approximation, the VPSC-simulated active slip systems are proportional to those of the measured dislocation-structure evolution in Figure 3-7. The experimentally-determined equidistant-dislocation-wall spacing is shown with hollow symbols: square (□) for the loading and circle (○) for the transverse directions, respectively. The dislocation density is presented in solid symbols, square (■), for the loading direction and circle (●) for the transverse direction. The dislocation density changes slowly within the 0 to 370 MPa, as elastic region. With the onset of the plastic deformation, the dislocation density starts to increase. The dislocation density slowly saturates after 870 MPa, but the equidistant-dislocation-wall spacing keeps on decreasing to the final measurement. The current results, shown in Figure 3-7, are

qualitatively similar to the previous calculations, with the assumption of the equal-dislocation activity from all primary slip systems (Huang *et al.* 2008).

Complementary TEM analyses confirm the formation of the hierarchical dislocation structure with a part of the dislocations grouped within the walls and part remained randomly distributed between them (Figure 3-8). Both images in Figure 3-8 are taken from same area of the sample deformed at 40%, but at different diffraction vectors, **g**. Diffraction at two different **g** changes invisibility conditions for some dislocations. For this reason, some of the dislocations are visible only at one of the images. Some dislocation debris is visible between the walls. The "blocky" structure showed typical dimensions of less than 0.5 microns. The walls are aligned along {110} not {100}. The distance between the walls estimated from the TEM data are surprisingly close to the average data obtained from neutron diffraction.

Motivated by Heidelbach's comments (2001) and based on the experimental results above, an attempt to track the microstructure of the single grains inside a polycrystal during the deformation is discussed.

3.4. Discussion

The lattice strain-stress relationships measured from 7 different {*hkl*} planes shown in Figure 3-2 demonstrate a clear linear response within the elastic region, especially below 300 MPa. Beyond the 0.2% yield strength, the slope of the stiffest {111} direction becomes smaller due to load sharing with the other grain orientation. The peak-intensity evolution in Figure 3-5(a) shows a clear onset of texture

development, once the alloy was plastically deformed beyond the 0.2% yield strength. Note that the input of the simulation is based on our measured data: The comparison between the experimental measurement and the simulated results is based on the macro stress-strain curve (Figure 3-3), and the lattice-strain evolution along the loading direction (Figure 3-9), respectively. The measured stress-strain points are located on the simulated stress-strain curve from 0% to 20% strain. The simulated and the experimental results practically coincide for strains up to 25%. At higher strains, the simulation gives slightly larger stress values then those measured. For the lattice-strain comparison, it can be seen that the VPSC simulations capture the characteristics of the lattice-strain distribution for most {*hkl*} within 370 MPa in the elastic region. It also shows the different slopes of each {*hkl*} corresponding to the respective elastic modulus according to the generalized Hooke's law. The measured {111} and {220} lattice-strain evolution is practically reproduced from the simulation. The deviation of the slopes is found on the {200} and {311}, which may be attributed to the hardening parameters influenced by the microstructure.

Based on the above comparison and the agreement of the texture development from the measured to the simulated results, the simulated slip-system activity could be used for calculating the dislocation-contrast factor. Moreover, since the simulated grains contain information of the grain orientation, single grains with specific orientations can be selected.

The reason to select the specifically-oriented grains is to consider the specimen-coordinate system confined by the setup of the two-direction detection

banks during the in-situ measurements. Figure 3-10 shows the details of this consideration. The specimen geometry is shown at the top of the Figure 3-10. The incident beam can be diffracted in several directions. Only diffraction from grains along the loading (in black arrow), and transverse (in red arrow) directions can be collected from the detection banks. However, during the plastic deformation, the grains can rotate their local grain-coordinate system, as shown in the bottom-left of Figure 3-10. As grains rotate, the materials' response can be measured only when these grains are reoriented into align planes in the loading and transverse directions of the specimen (Figure 3-10).

As a result, a search of the simulated grains is based on the relative orientation of the grains with respect to the specimen-coordinate system. Although there are only few grains oriented along these two directions, the grains that do reorient to the detector directions can be used to study the slip-system evolution in these specifically-oriented grains embedded within our 2,592-grains, polycrystalline models. The simulated slip-system activity is shown in Table 3-3.

From 2,592 grains used in the simulation, only two grains are favorably oriented to diffract in the direction of detection banks (Table 3-3). The first grain is nearly exactly oriented for diffraction into both banks. The accumulated probability for the two most favorable slip systems in the loading direction is approximately 57% and the accumulated probability with an additional slip system is approximately 72%. In a second grain, favorably oriented for diffraction in the transverse direction, we also observe that the accumulated probability for three slip systems reaches 92%. The

results suggest that the number of the active slip systems with the probability (from 15 to 40%) for different grains is between 2 and 3. This result agrees with Fleischer's TEM investigation of brass crystals (1987), showing that the average number of active slip planes is about 2.5.

If slip systems with a 5 - 15% probability are included, about 5 systems are predicted by the model. The results agree with the observations of Margulies *et al.*'s (2001).

For most probable slip systems, the slip-system-dependent contrast factors were calculated (Table 3-3) for the grain with the best orientation for diffraction into each detection bank (Figure 3-10). The parameters of dislocation arrangements calculated, based on Equations (3-10) and (3-11), are presented in Table 3-4. The estimated dislocation density and dislocation-wall spacing obtained from the loading and the transverse directions are essentially the same (Table 3-4) and agree with TEM observations.

As a result, our method demonstrates a new approach to the study of the microstructure evolution during tension. Overall, the discussed results are used to understand the slip-system-related microstructure evolution during the tensile deformation. The good agreement between simulated and experimental results arises from the properties of the superalloy, which obey the assumptions of the VPSC model. In the future, this method will be applied to other cubic materials.

3.5. Summary

The present study reports combined effects of experiments and simulations of plastic deformation in an f.c.c. nickel-based single-phase superalloy under tension. Texture simulations beyond 30% deformation with the VPSC model were performed. The simulations were based on the lattice strains measured by in-situ neutron-diffraction experiments at room temperature during tension experiments. The preferred orientations were simulated for the ensemble of 2,592 grains. The gradual development of the texture is both simulated and measured by in-situ neutron experiments. The agreement between the experimental measurements and simulated results demonstrate that the assumed crystallographic slip systems are the major contributors during the plastic deformation of the superalloy. A possible contribution of each grain into the Debye diffraction intensity ring was determined, and the two grains with specific orientations, diffracting neutrons in the directions of two detection bank were found. For the above two grains, the dislocation-contrast factor has been updated with the simulated probability of the active slip systems. The slip-system-dependent contrast factors are used to calculate the parameters of the dislocation arrangement for the specifically-oriented grains.

Chapter 4: Tensile and Cyclic-loading Effect on the Annealed Single-phase Alloy

This Chapter presents the intimate relation and the differences between tensile and cyclic deformation, based on the neutron-diffraction-profile-analysis methods developed in Chapter 3.

The plastic behavior of an annealed alloy, a face-centered cubic (f.c.c.), nickel-based superalloy, was examined by in-situ neutron-diffraction measurements at room temperature. Both monotonic-tension and low-cycle-fatigue experiments were conducted. Monotonic tension straining and cyclic-loading deformation were studied as a function of stress. The plastic behavior during deformation is discussed in light of the relationship between the stress and dislocation-density evolution. The calculated dislocation-density evolution within the alloy reflects the strain hardening and cyclic hardening/softening. Experimentally-determined lattice strains are compared to verify the hardening mechanism at selected stress levels for tensile and cyclic loading. Combined with calculations of the dislocation densities, the neutron-diffraction experiments provide the direct information about the strain and cyclic hardening of the alloy.

4.1. Introduction

The design of advanced metal alloys requires the detailed information about the mechanical behavior and property evolution in service beyond elasticity, which is roughly independent of defects. Plasticity and the underlying deformation

mechanisms evolve during service. In metals, dislocations are responsible for most of the plastic deformation. During deformation, these dislocations multiply and self-organize into mesoscale structures that strongly influence future deformation. However, Guinier (1989) has pointed out the challenge of studying dislocations, especially for fatigue, in light of the sample preparation. In the present work, monotonic tension and cyclic-loading during in-situ neutron experiments have been used to compare and study the fatigue behavior of a superalloy. Understanding the plastic behavior of this newly-designed nickel-based superalloy is important for applications in extreme environments. In-situ neutron-diffraction experiments provide non-destructive, volume-averaged bulk characterization of the atomistic mechanisms with qualitative trends for studying the plastic deformation of the alloy. The focus of the current research is associated with the dislocation evolution during the plastic deformation.

Transmission-electron-microscopy (TEM) (Hirsch *et al*., 1960; Howie and Whelan *et al*. 1962) is well established for the study of local structures and the internal stresses contributed by dislocations. However, in my current study, only a small amount of material is observed with each thin specimen, and the statistics and the response of the experimental are limited by the demanding sample preparation. X-ray experiments provide an alternative method for studying dislocation structures, which complement TEM experiments. X-ray diffraction experiments with advanced analyses have characterized different types of dislocations (Mughrabi 1983, Ungar *et al.*, 1999 and Barabash *et al*., 2003). Anisotropic-strain accommodations by different

grains were considered by Stephen (1999). Recently, Jakobsen *et al*. (2006) and Levine *et al*. (2006) report the use of the synchrotron x-ray accompanying TEM results to study local dislocation behavior during plastic deformation. These studies illustrate the potential of diffraction techniques for the investigations of dislocation behavior in plastic deformation. The current study reports in-situ neutron-diffraction measurements that utilize the advantage of the diffraction experiments for examining dislocation statistics associated with plastic deformation. The advantages of the present neutron measurements are:

- The high penetration of neutrons characterizes the bulk behavior with large gauge volumes, and, hence, good statistics. Although the divergence of the neutron beams is higher than that of high-energy synchrotron x-rays, the typically lower resolution of neutron measurements is sufficient for our research, which focuses on statistical averages.
- The Spectrometer for MAterials Research at Temperature and Stress (SMARTS) (Bourke *et al*., 2002) at the Los Alamos Neutron Science Center (LANSCE) can be used to conduct in-situ measurements to observe the behaviors of the deformation from a single specimen. The in-situ measurement eliminates confusion from ex-situ experiments that require several specimens and associated sample preparations.

The current study focuses on the plastic behavior of a nickel-based alloy under tension and cyclic loadings. To address this problem, the in-situ neutron measurements were designed with these components.

[1] Tension experiments were conducted to study strain-hardening mechanisms and the associated dislocation-density evolution;

[2] Low-cycle-fatigue experiments were performed to study cyclic hardening and softening, and the dislocation density evolution;

[3] Dislocation densities as a function of the true stress from strain hardening, cyclic hardening, and cyclic softening are compared with the lattice-strain evolutions to examine the plastic behavior of the alloy.

4.2. Experimental Procedures

The HASTELLOY® C-22HS™ alloy is a nickel-based superalloy (Ni-21Cr-17Mo in the weight percentage). The alloy is intended to be used under corrosive environments and where high strength is demanded. The alloy is mill annealed at 1,080^{o}C to minimize the formation of precipitates and to achieve a single-phase, face-centered cubic (f.c.c.) alloy, as characterized by transmission-electron-microscopy (TEM) (Lu *et al*., 2007). The average grain size of this alloy is about 90 μm.

Two sets of the specimens, one for tension and the other for fatigue were cut from the same cylindrical alloy bar. The dimensions of the dog-bone shape specimens were selected according to the standard ASTM/E 606 as shown in Figure 4-1a. In-situ neutron measurements were used to monitor the monotonic-tension and low-cycle-fatigue experiments. A gauge volume of about 120 mm^3 from the center of the specimen was used through both the measurements of monotonic-tension and low-cycle-fatigue experiments. The tests were carried out with the SMARTS

beamline of LANSCE and the environment is at room temperature (Benson *et al*. 2006). The specimens were aligned 45° to the incident neutron beam with two detector banks fixed at $2\theta = \pm 90^{o}$. Hence, one detector bank collected diffraction data along the loading direction ($Q_{//}$), and the other collected the diffraction data in the transverse direction ($Q_{\perp}$) as shown in Figure 4-1b. The Q directions are associated with two distinct sets of grains: $Q_{//}$ measures the lattice strains for {*hkl*} planes parallel to the strain; and $Q_{\perp}$ measures the lattice strains perpendicular to tension load. Practically grains with surface normals in the interval of $\pm 4^{\circ}$ relative to the exact Bragg condition give input to the diffraction.

Since the beam paths are slightly different for loading to transverse directions (Figures 4-1b and 1c), we use reference points accordingly for peak-profile analyses. For the tension experiment, the sample was loaded in the strain control using a strain rate of 0.001 per second with intermittent holds at constant strain levels to allow for neutron-diffraction measurements. The specimen was elongated to a strain of about 45% and then failure. The closest measurement before necking is at about 32% strain. The stress-strain curve of the in-situ tension experiments is presented in Figure 4-2. The onset of the plastic deformation is marked in the green region and is enlarged as the inset plot. The 0.2% yield stress is around 370 MPa, which will be a reference for the evolution of dislocations. Load drops are seen in the plastic region during the constant strain holds due to room-temperature relaxation. The count time for a single neutron diffraction measurement is about 10 minutes.

The low-cycle-fatigue experiments were conducted with a minimum strain ($\varepsilon_{min.}$) and maximum strain ($\varepsilon_{max.}$) of -1% and +1%, respectively ($R = \varepsilon_{min.} / \varepsilon_{max.} = -1$). The frequency of the loading cycle was 0.5 Hz. The neutron-diffraction data were collected at different cycles during the fatigue experiments: 1st, 4th, 8th, 12th, 30th, 50th, 100th, 250th, 500th, 1,000th, 1,250th, and 1,500th cycles. The cyclic-loading sequence in Figure 4-3a shows the deformation status during the measurements.

The specimen was loaded to a maximum engineering strain of 1% at Measurement 1. At Measurement 2, the sample was unloaded to 0 MPa. At Measurement 3, the sample was compressed to a macro strain of 0%. At Measurement 4, the sample was compressed to an engineering strain of - 1%. At Measurement 5, the sample was unloaded from the compression to 0 MPa. At Measurement 6, the sample was loaded to 0% engineering strain. The 7th measurement (Measurement 7) is made at the 1% engineering strain again to compare with Measurement 1 for cyclic effects within one fatigue cycle. Neutron measurements were performed at these 7 measurement points as a function of fatigue cycles. The macroscopic stresses at Measurement 1 as a function of the fatigue cycles are presented in Figure 4-3b (Huang *et al.*, 2007). The experiments conducted at Measurement 1 of the fatigue cycles mentioned above are compared with the results from the monotonic-tension experiments.

Synchrotron x-ray diffraction (XRD) experiments were conducted to complement the neutron measurements. The high-energy (115 keV) X-ray diffraction experiments were performed at the 11-ID-C beamline of the Advanced Photon

Source, Argonne National Laboratory. The size of the X-ray beam was controlled to 1.0×1.0 mm^2 to collect diffraction data with good statistics. Undeformed, tension-failed, and cyclically-failed specimens were prepared for the synchrotron experiments. Slices were cut from the center of the mechanically-tested specimens, which were deformed under the monotonic tension and low-cycle-fatigue tests. The cut materials were, then, polished to remove the oxides and other additives to eliminate contaminations associated with the sample preparation. The diffraction patterns were recorded using a two-dimension (2-D) image plate detector (Mar345). The symmetry of the diffraction rings, as shown in Figure 4-4, indicates that the textures of the undeformed, tensioned, and cyclically-deformed specimens were symmetrical, and, hence, the depiction of the two-detector-banks data from the SMARTS measurements is representative for describing the evolution of the elastic/plastic response of the material during the deformation. The most distinguished difference from monotonic-tension to cyclic deformation is that there is texture developed after the monotonic-tension (Wenk *et al*., 2003) but texture development is not seen during cyclic deformation [compare solid and spotty characters of the diffraction rings in Figures 4-4b and 4c.] Turkmen's modeling work (Turkmen *et al*., 2002) also finds little texture evolution under cyclic loading.

4.3. Neutron-data Analyses

The current in-situ neutron-diffraction profiles are refined by the General Structure Analysis System (GSAS) (Larson and Von Dreele 2004), which is based on

full-pattern Rietveld analysis method (Rietveld, 1967). The changes in the peak positions and the peak widths are determined from the diffraction patterns and presented as the lattice strain and full-width-half-maximum (FWHM), respectively.

For the profile analyses, there are several sources of diffraction-peak broadening, such as instrument broadening, the size of the coherently scattering domains, dislocations (defects) (Ungar *et. al*. 1999, Balzar *et al*. 2004, Barabash 2001, Ice and Barabash 2007), and the anisotropic strain distribution (Stephens 1999). For the current study, since the same alloys are tested with the same instruments, the instrumental broadening was measured from the diffraction profile of a reference sample (before the deformation) and was used to remove instrumental broadening from the total broadening.

As shown in Figure 4-1b, the diffracted beam path is shorter in the transverse direction ($Q_{\perp}$) than that in the loading direction ($Q_{//}$). Since the difference of the beam path might alter the diffracted peak-profile, the peak-profile analyses used different references with respect to different directions according to account for this geometry anisotropy. However, since correlation between the neutron-beam path to the peak-width is not necessary linear, there is no universal equation to normalize the geometrical anisotropy.

We use two distinct approaches to describe the appearance of line broadening: phenomenological and atomistic lattice level. In the phenomenological approach, the shift of the peak depends on the macroscopic stress, and the broadening of the peak is related to micro strains/stresses that change from grain to grain. Measurements of the

peak shift during the deformation allow us to follow the evolutions of such phenomenological parameters as macro stresses and strains. There are several types of strains that could contribute to the peak-width broadening, such as intergranular and intragranular strains. Different types of strains arise from the various microstructures, such as different types and densities of dislocations. The lattice or atomistic approach can be used to understand the dependence of the broadening on the particular dislocation/defect distributions within the grain. Peak-profile analysis provides statistical information about the dislocation-density evolution under deformation.

To decompose the broadened asymmetric peaks into two broadened symmetric sub-peaks, the pseudo-Voigt function is applied to carry out single-peak fitting to distinguish the different diffraction patterns by GSAS (Balzar *et al*. 2004). The Lorentzian and Gaussian peak broadening components were de-convoluted by a pseudo-Voigt function in GSAS (Larson and Von Dreele 2004). The FWHM of Gaussian ($FWHM_G$) and Lorentzian ($FWHM_L$) components were characterized as a function of the stress, respectively, because the integrated intensities of these two sub-peaks (Gaussian and Lorentzian) are related by random dislocations and dislocation walls, respectively. The procedure is similar to size/strain separation (Balzar *et al.* 2004). As a result, the smaller sub-peak is diffracted by the cell walls, and the larger one comes from the cell interiors as homogenously distributed dislocations (Levine *et al.* 2006). $FWHM_G$ represents the input, which can be generated by the uniform randomly distributed dislocations, while $FWHM_L$ indicates the input from the non-

uniform patterned dislocations substructures, such as the dislocation walls (Mughrabi 1983, Barabash *et al*. 2001). The spacing between dislocation walls (D) is calculated, according to Equation (4-1) (Barabash *et al*. 2001; Ice and Barabash 2007).

$$D \sim \frac{\pi\zeta}{\Delta FWHM_L} \tag{4-1}$$

Here ζ is the contrast factor, used to calculate the Lorentzian part, from the whole powder-pattern fitting of peak profile. As a first approximation, the dislocation density is calculated, assuming equal dislocation activity for all primary slip systems. The density (n) of the randomly distributed dislocations is calculated according to Equation (4-2) (Barabash *et al*. 2001; Ice and Barabash 2007):

$$n \sim \left(\frac{\Delta FWHM_G * d_{hkl}}{C * |b|} \right)^2 \tag{4-2}$$

Here the Burgers vector (b), the contrast factor (C) for the Gaussian component, the d_{hkl}-spacing for each $\{hkl\}$ plane, and the $FWHM_G$ of all $\{hkl\}$ planes are considered.

The lattice strains, ε_{hkl}, are calculated by the changes in the d-spacing, d_{hkl}, at different applied loads during the monotonic-tension experiment or at different number of fatigue cycles for low cycle fatigue experiments with respect to that of the reference d-spacing, d^0_{hkl}, as shown in Equation 4-3 (Daymond *et al.* 1997).

$$\varepsilon_{hkl} = \frac{d_{hkl} - d^0_{hkl}}{d^0_{hkl}} \tag{4-3}$$

The reference lattice spacing, d^0_{hkl}, was determined from the measured lattice spacing before deformation.

4.4. Results

Plots of the FWHM versus $2\pi/d$ as a function of stress for tension experiments and low-cycle-fatigue experiments are shown in Figure 4-5. Here d is the d-spacing. In the monotonic experiments, correlations between the FWHM and $2\pi/d$ deviates from linearity as the strain increased, while the applied stress increased. For the low-cycle-fatigue experiments, the correlations changed as a function of fatigue cycles, where the engineering strain was controlled at 1% at Measurement 1, the applied stress varies as a function of fatigue cycles. FWHM for both types of loading are markedly anisotropic depending on $\{hkl\}$ which is in agreement with the previous observations of Ungar T. *et al.*, 1999. This is an indication of the formation of the patterned cell-wall dislocation substructure.

Dislocation-density and Dislocation-wall Spacing Evolution

For the monotonic-tension experiment, the dislocation density as a function of the true stress is shown in Figure 4-6a. The following three regions are distinct:

- Stage I (0 to 370 MPa): the region of the elastic straining is a stage where stresses increased as the strain increased, as shown in the stress-strain curve (Figure 4-2), while the dislocation density practically does not change too much (Figure 4-6a). The calculated dislocation-wall spacings are large (> 1,500 nm) and fluctuate in both $Q_{\perp}$ and $Q_{//}$ directions in Figure 4-6b. However, the accuracy of the neutron-diffraction measurements is inadequate for characterizing cell size larger than 1,500 nm, hence, larger symbol sizes are plotted for the calculated values at Stage I.
- Stage II (370 to 750 MPa): the dislocation-strengthening region where the dislocation density is proportional to the true stress. In this region, the stresses are high enough so that dislocations start to multiply and pile up, and, hence, increase the back stress, which resist the motion of additional dislocations. The dislocation density starts to increase rapidly at about 370 MPa. At this stress value, the dislocation sources became activated meanwhile the dislocation-wall spacings decreased in $Q_{\perp}$ and $Q_{//}$ directions simultaneously and reached 800 nm.
- Stage III (above 750 MPa): the dislocation density gradually saturated with the increasing stress in $Q_{\perp}$ direction but not too much in $Q_{//}$ direction. The dislocation-wall spacing in $Q_{\perp}$ and $Q_{//}$ directions decreased from 800 nm to 400 nm, where the sample is close to necking. At the point of *macro yielding*, the dislocation-wall spacings

possess the essential trend of the stress-strain curve, which does not change slope from 370 to 1,200 MPa (Figure 4-2). The value of the domain size is 400 nm (30% strain of the stress-strain curve), which is comparable to what is observed by Valiev (Valiev *et al*., 2000). The reasonable mechanism is Mughrabi's cell-wall structure (1983), which views the evolution from homogeneous dislocation distribution to the heterogeneous dislocation cell-wall structure consisting of the soft channels and the periodic array of the hard walls. The reason for this evolution trend is the compatibility to the changing shear strain fields, which is a continuum manifestation of the change of the heterogeneous channel-cell wall structure. It also suggests that the dislocation arrangements develop to lower-energy heterogeneous configurations compared to homogeneously distributed dislocations.

For low-cycle-fatigue experiments, at the 1% strain level, cyclic hardening started around 370 MPa until about 600 MPa, and is, then, followed by cyclic softening. Figure 4-7a shows the dislocation density as a function of fatigue cycles. The dislocation density increased as the stress increased and, then, saturated and mildly decreased as a function of fatigue cycles. The dislocation density of low-cycle-fatigue experiments has approximately the same value as the monotonic experiments around the same true stress level as shown in Figure 4-6a. The true stress region at 1% strain (Measurement 1) within 1,500 fatigue cycles (Figure 4-3b) corresponds to

the interval of 400 ~ 600 MPa. For comparison between cyclic loading and monotonic tension, the same stress range is highlighted in the Stage II of the monotonic experiments. A comparison of the two experiments will be made within 400 ~ 600 MPa for lattice strain in the next section. The calculated dislocation-wall spacings evolved in a reverse relation to the dislocation density as shown in Figure 4-7b. Again, for dislocation-wall spacings exceeding 1,500 nm, the larger legend-symbol size indicates larger error bars. A clear anisotropic quantitative difference of dislocation density from the loading to the transverse directions under tension is due to the fact that intensity distributions for loading and transverse directions come from two orthogonal sets of grains as shown in Figure 4-1c. Only grains, which satisfy Bragg's condition, will contribute to diffraction. For example, grains with {200} planes perpendicular to loading direction will give {200}-diffraction peaks into loading direction (Q_{ll}). Grains with the same planes {200}, but oriented orthogonal to the loading direction, diffract neutrons into the transverse-direction ($Q_{\perp}$) detectors. These two sets of grains are orthogonal to each other and have different Schmidt factors where Schmidt factor is distinct to different slip system, and, hence, resulted in different dislocation density in the grains with different orientations (Liu *et al*., 1998 and Margulies *et al.,* 2001).

Lattice-strain Evolution

Single-peak fitting was applied to study "lattice-strain" evolution. The lattice strains of the monotonic-tension experiment, ε_{hkl}, are calculated from changes in the

d-spacing, d_{hkl}, at different applied loads with respect to the reference *d*-spacing, d^0_{hkl} in Equation (4-3). The reference lattice spacing, d^0_{hkl}, was determined from the measured lattice spacing before the deformation (a nominal tensile load of 0.099 MPa to ensure that the sample did not sag in the horizontal loading geometry).

$$\varepsilon_{hkl} = \frac{d_{hkl} - d^0_{hkl}}{d^0_{hkl}} \tag{4-3}$$

The evolutions of the lattice strains of the monotonic-tension experiment showed that the response of the lattice strains in the elastic region of the applied load (region I in Figure 4-6a) followed Hooke's relationship, and the stiffness of {111} plane is the largest, {200} is the least, and {220} and {311} are in between. Similar trends were observed during in-situ neutron-diffraction measurements on a face-centered-cubic (FCC) stainless steel by Daymond *et al*. (1997). For the low-cycle-fatigue experiments, the lattice strains, ε_{hkl}, are calculated in the same fashion as the monotonic-tension experiment at different fatigue cycles with respect to that of the reference d-spacing, d^0_{hkl}. The reference lattice spacing, d^0_{hkl}, was determined from the measured lattice spacing before the cyclic loading. A similar response was observed (Huang *et al*., 2007) from low-cycle-fatigue experiment although the whole measurements were conducted at a 1% engineering strain. Lattice strains increased as the cyclic hardening continued until an apex stress at 600 MPa where the stress began to decrease as softening starts to take place, and, hence, the lattice strains decreased.

To clarify the effects of the plastic deformation from two experiments, the elastic portion of the lattice strains were subtracted from the lattice strains as in the Figure 4-8a for low-cycle fatigue and Figure 4-8b for monotonic-tension experiments, respectively. The {111} and {200} of two different experiments have the comparable trends and levels while the {220} and {311} are not as alike. This difference may be caused by the texture formation during monotonic tension experiments, which is in agreement with our XRD results (Figure 4-4). More details of the strain-related texture formation have been reported (Miller *et al.*, 2005 and Bernier *et al.*, 2006). From the current study, the evolutions of lattice strains during both cyclic loading (up to 100^{th} cycle) and tension experiment (Stage II) reached similar values at the same true stress levels, which suggest further study. Since the true stress level of the Stage III of monotonic tension experiments was beyond that of the low-cycle fatigue experiments, more research is needed to discover the different failure mechanisms.

4.5. Discussion

For monotonic experiments, the dislocation density is a good reference for the deformation process. The onset of Stage II is very close to the 0.2% yield strength, which supports the dislocation-density calculation (Figure 4-6a). The peak-broadening indicates intensive plastic deformation which resulted from an increase of the dislocation density. The inverse behavior between dislocation-density (Figure 4-6a) and dislocation-wall spacing (Figure 4-6b) as a function of stress are similar to the observations of Hansen (2005). When the dislocation density as a function of the

stress starts to transit to Stage III, there is a slowdown in the rate of the dislocation density multiplication in both directions. Moreover, it saturates in $Q_{\perp}$ direction (Figure 4-6a) around 700 MPa, which indicates that the multiplication of dislocation density decelerates. However, the dislocation-wall spacings decrease at the same rate in both Stages II and III, which indicates that the dislocations pile-up as stress increases and self-organize as a function of the stress. A similar statement has been proposed by Kuhlmann-Wilsdorf's TEM works (1962 and 1999), which suggests that the character of the dislocation distribution remains unchanged, only the scale of the distribution changes. With further deformation, beyond Stage II, the number of free dislocations within the cells gradually keeps steady to the point where glide dislocations may move relatively unhindered from one cell wall to other cell walls (Kuhlmann-Wilsdorf, 1962 and 1999).

For the low-cycle-fatigue experiments, since the cyclic hardening starts around 400 MPa and is about to end at the 100^{th} fatigue cycle around 600 MPa, the peak widths broaden accordingly, and, then, the widths reduce, with the cyclic softening. The calculated dislocation density is shown in Figure 4-7a. The dislocation density of the monotonic tension experiments under same true stress region is shown in Figure 4-6a for comparison.

It is interesting to compare the intergranular strains (ε^{I}_{hkl}) of the two types of deformation. The lattice strains (ε_{hkl}) after subtracting the elastic part for both experiments are calculated, where the elastic strains are calculated based on the elastic modulii (E_{hkl}) and the true stress (σ). The evolutions of ε^{I}_{hkl} under the

monotonic tension for all {*hkl*} planes in $Q_{\perp}$ direction (Figure 4-8a) are compared to those of the low-cycle-fatigue experiments at 1% strain as shown in Figure 4-8b. These calculated lattice strains from Eq. (4-4) are intergranular strains (ε^{I}_{hkl}) from the combined effects of the elastic anisotropy, thermal anisotropy, and plastic anisotropy (Brown *et al*., 2003). Here, the elastic response is subtracted from measured lattice strains.

$$\varepsilon^{I}_{hkl} = \varepsilon_{hkl} - \frac{\sigma}{E_{hkl}} \tag{4-4}$$

The comparison of intergranular strains (ε^{I}_{hkl}) matches the stress and plastic strains (ε_p) relationship as shown in Equation (4-5), which concerns the effects of the dislocation density (Dieter 1986).

$$\sigma \propto \alpha G b \sqrt{M} \sqrt{\varepsilon_p} \tag{4-5}$$

Here the true stress (σ) is proportional to the shear modulus (G), Burgers vector (b), the multiplication factor (M), and the plastic strain (ε_p). The trend and quantity of ε^{I}_{hkl} from these two experiments are similar as shown in Figures 4-8a and b, which suggest that under the current experimental parameter, for this alloy, the hardening mechanism is mainly dominated by *dislocation hardening* in the true stress region (370 ~ 600) MPa. The following conclusion can be made for *dislocation hardening*:

After the elastic region (Stage I), the increase of the true stress followed by the increase of the lattice strain, results in the plastic deformation accompanied by the increase of the dislocation density and decrease of the dislocation-wall spacing. The decrease of the dislocation-wall spacing indicates the formation of a self-organized cell-wall structure, where more dislocations start to accumulate within dislocation walls. More specifically, during the plastic deformation, the energy of the alloy is partially stored as dislocations, which are not randomly distributed but accumulate in dislocation boundaries. Moreover, the FWHM versus $2\pi/d$ relationship associating with the stress reflects that the dislocation hardening is the major strengthening mechanism within these stress levels.

The reason for the different quantities of both the dislocation density and dislocation-wall spacings from two types of deformation at the similar stress levels is discussed below. In fatigue experiments, it seems that the dislocations may annihilate each other during the course of cycling. The mutual annihilation of dislocations can take place during cyclic loading, which results in a smaller dislocation density but wider dislocation-wall spacing (Figures 4-6 and 7). As a result, even at the similar stress levels, the different quantities of dislocation densities and dislocation-wall spacings could indicate two types of loading. Further research is following up now for distinguishing the difference for more details.

Although the differences of the dislocation density and wall spacing from two types of deformations are recognized, the comparisons of the dislocation characteristics within a fatigue cycle during low-cycle-fatigue experiments are still

plausible in statistics point of view. The symmetrical stress-strain response under tension and compression in the 1st fatigue cycle (Figure 4-3a) for the low-cycle-fatigue experiments is in agreement with earlier observations of Mughrabi 1983 and Ungar *et al.* 1993.

For the dislocation characteristics from the low-cycle-fatigue experiments, the evolution of the dislocation density and dislocation-wall spacing are shown in Figures 4-9(a) and (b), respectively. Seven measurements within one fatigue cycle are presented to address Guinier's (1989) question of the atomic mechanisms during fatigue deformation. At the 1st cycle, the Measurements 1, 4, and 7 have the higher dislocation density than the other measurements, which are in proportion to their stresses.

And the Measurement 7 has higher dislocation density than that of the Measurement 1, which shows the dislocation hardening even within the 1st cycle. However, at the 100th fatigue cycle, where the cyclic softening was about to occur, the dislocation density decreases from Measurements 1 to 7 within one fatigue cycle. A relative little decreasing of dislocation density of the 1,500th cycle in Figure 4-9a agrees with the very little cyclic softening as shown in Figure 4-3b. The comparisons of the dislocation density at the 7 measurements for 3 different fatigue cycles are shown in Figure 4-9a. Although the same engineering strains/stress were controlled for the 1st, 100th, and 1,500th fatigue cycles during the measurements, the observed dislocation density within the 1st cycle is several times less than that of the 100th and the 1,500th cycles, which shows the accumulation of the dislocation density during

cyclic hardening. Figure 4-9b shows the dislocation-wall spacing. The dash line and larger legend size in Figure 4-9b are used for the 1st fatigue cycle, where the calculated values are greater than 1,500 nm (similar to Figures 4-6b and 7b). The evolutions of dislocation-wall spacing in Figure 4-9b show the reverse trends where the spacing decreased during cyclic deformation after the 100th and 1,500th cycles. The similar inverse relationship between dislocation density and dislocation-wall spacing was reported by Hansen (2005).

Within one fatigue cycle, the dislocation-wall spacings of Measurements 1 (maximum tension strain), 4 (maximum compression strain), and 7 (maximum tension strain) were smaller than those of the other measurements, which were the inverse trends of the dislocation density as shown in Figure 4-9(a). The inverse relationship demonstrates that while the dislocation density increased under the cyclic effects in the most strained/compressed status, the accumulation of the dislocation density and their rearrangement shortened the dislocation-wall spacing. The natural exception is the 1st measurement of the 1st fatigue cycle, where the monotonic tension was just applied from 0 MPa to 1% engineering strain, but the cyclic deformation did not start yet. The variation between different Measurements gradually decreases as the number of fatigue cycles increased. It seems that as the fatigue cycles increases within 1,500 cycles, dislocation-wall spacing between dislocation multiplication and annihilation gradually reaches equilibrium.

4.6. Summary

In-situ neutron-diffraction results were refined by GSAS. The pseudo-Voigt function was applied to distinguish between Gaussian and Lorentzian peak components. The density of dislocations and the average distance between dislocation walls were calculated accordingly to characterize the bulk response during the plastic deformation. Hence, the neutron-diffraction profiles were used to characterize the dislocation distributions. For this alloy, there was practically no accumulation of dislocations in the elastic region (Stage I). Within 370 ~ 600 MPa, the dislocation hardening was the major strengthening mechanism of the monotonic tension and low-cycle-fatigue experiments. The dislocation density and the dislocation-wall spacing evolved accordingly within one fatigue cycle. Above 750 MPa, the dislocation-wall spacing evolved differently with the dislocation density because the mechanical properties of dislocations within the walls are stiffer than those of inside the cells as described by Mughrabi's composite model. The same analysis method is applied to study the cyclically-deformed alloy. Different quantities of the dislocation density and dislocation-wall spacings demonstrate the ability of the diffraction profiles to distinguish different types of loading at similar applied loads. For low-cycle-fatigue experiments, the calculated dislocation density and dislocation-wall spacing are promising indicators for characterizing the cyclical hardening and early softening phenomena within 1,500 fatigue cycles of the alloy.

Chapter 5: Fatigue-induced Reversible/Irreversible Structural-transformation Study of the Annealed Single-phase Alloy Using Combined In-situ Neutron-Diffraction and Thermal Characterization

After discussing the differences between the tensile and cyclic deformation in Chapter 4, this Chapter focuses on the deformation mechanism subjected to cyclic loading only. Moreover, the relation between microscopic and macroscopic states is investigated via the thermal mechanical observations connecting neutron-diffraction and bulk-parameter measurements.

Cyclic loading and the subsequent fatigue damage have been investigated with the in-situ neutron-diffraction and thermal characterization for a single-phase, polycrystal nickel-based alloy. The lattice-strain evolution is compared with the bulk parameters, such as the applied stress and the thermal response as a function of the fatigue cycles. The in-situ neutron-diffraction and thermal-evolution results identify the development of the three fatigue-damage stages. Fatigue damage is observed with bulk hardening, softening, and eventual saturation evident in both of the diffraction patterns and the thermal-evolution features. An increase in the dislocation density and the formation of the patterned-dislocation structure are responsible for hardening within the early cycles. With further cyclic loading, the rearrangements of the dislocations result in the cyclic softening. The transition to saturation cycles is characterized by the anisotropy of the lattice-strain evolution. The non-monotonic thermal response and the irreversible anisotropy of the lattice-strain evolution are

observed in the final saturation fatigue cycles. The fatigue-damage microstructure and dislocation-substructure evolution are studied with diffraction-profile analyses. The fluctuations of the differential dislocation density and size of the patterned substructure with fatigue cycles along with the in-situ thermal measurements reveal a second-order structural transition and indicate the development of the irreversible fatigue-induced microstructure.

5.1. Introduction

Fatigue is used widely to describe the metallurgical-cyclic-deformation process. Cyclic loading is the major cause of fatigue failures in mechanical components (Mughrabi, 2009). Fatigue failures resulting from the accumulated plastic deformation have been extensively observed via the electron microscopy (Kuhlmann-Wilsdorf, 1999; Zhang et al., 2008) and discussed in many other approaches (Mott, 1958; Neumann, 1977; Kim and Laird, 1978; Essmann and Mughrabi, 1979; Essmann *et al*., 1981; Davidson and Lankford, 1992; Dingli *et al*., 2000; Turkmen *et al.,* 2002; Jiang *et al*., 2005; Cantrell, 2006; Kang *et al*., 2009; Taleb and Hauet, 2009; Tahara *et al*., 2009; Bridier *et al*., 2009). Moreover, to assess the fatigue damage, Mughrabi (2000) has pointed out the important aspects of the fatigue-induced plastic deformation, such as cyclic hardening, softening, and saturation. The cyclic softening and saturation processes, which directly result in the final failure, draw much attention because of the complicated plastic mechanisms (Mughrabi and Pschenitzka 2005; Brown 2006). Cyclic softening engages a wide

range of the physical metallurgical phenomena of the dislocations. There are complicated softening mechanisms in the polycrystalline alloys (Doherty et al. 1997; Agnew and Weertman 1998). In reality, it is not easy to clearly define the governing processes because of the challenges in the experimental approaches. It is also not trivial to obtain the actual interactions at the atomic levels because of the obvious complexity of the microscopic fatigue damages involved (Suzuki and Egami, 1985; Abdu-Latif and Saanouni, 1996; Wang *et al.* 2003; Bian *et al*., 2008). To investigate the microscopic interactions, based on atomic properties, is important to obtain the macroscopic quantities (Nix *et al.* 1985; Ashby 1989; Jiang *et al*. 2003; Tomota *et al*. 2004; Jia *et al*. 2008). In view of these considerations, two kinds of thermodynamics quantities (Girifalco 2000) were measured in this study, such as the external pressure and temperature together with microstructural parameters, including the lattice-plane spacing and the dislocation-substructure parameters in terms of the density and the size of the patterned-dislocation-wall structure. The measurements were restricted within the macroscopic strain levels at fixed tension (+ *1%*) and compression (- *1%*) strains, respectively, during the fatigue cycles.

In order to bridge the connections of the macroscopic and microscopic descriptions, in-situ neutron diffraction and in-situ thermal experiments were performed simultaneously. In particular, a nickel-based polycrystalline superalloy is subjected to cyclic loading in this study. The in-situ neutron and thermal measurements were applied to monitor the fatigue damage on an identical specimen until the final cyclic failure. The relationships between the bulk property and

microscopic-level-structure development are explicitly examined to further study the fatigue features at different damage stages.

5.2. Experimental Procedures

The nickel-based (Ni-21Cr-17Mo in weight percentage) sample used in this study was machined from a commercial alloy. The ternary element, Cr, added to the Ni-Mo binary system is to improve the oxidation resistance for high-temperature applications. The alloys were annealed to dissolve most precipitates with an almost texture-free condition in a face-centered-cubic (f.c.c.) structure (Huang *et al.* 2008a). The alloy is designed to improve the resistance to both uniform and localized corrosion as well as to a variety of mixed industrial chemicals. The tensile data for hot-rolled and annealed bar at the room temperature are: 0.2%-offset-yield-strength is 380 MPa, ultimate-tensile-strength is 800 MPa, and elongation is about 60%.

In-situ neutron-diffraction measurements were conducted on the Spectrometer for MAterials Research at Temperature and Stress (SMARTS) of the Manuel Lujan Jr. Neutron Scattering Center, Los Alamos Neutron Science Center (LANSCE). Details of applying in-situ neutron diffraction with the Spallation Neutron Source for low-cycle-fatigue experiments can be found elsewhere (Lorentzen *et al.* 2002; Wu *et al.* 2008). A short description here is to clarify the deformation procedures on the specimen for the later discussions. The cylindrical sample has a 19.05-mm length with a 6.35-mm diameter for the gage section. It was mounted in the hydraulic load frame, relative to two banks of the detectors. These two detector banks

simultaneously record complete diffraction patterns with diffraction vectors of the gauged polycrystalline grains parallel (loading direction) and perpendicular (transverse direction) to the applied load, respectively, as illustrated in Figure 5-1. The time-of-flight diffraction was acquired with a count time of about 15 minutes for statistically-sufficient-intensity scattering to analyze the diffraction profiles. For the diffraction-profile fitting, a pseudo-Voigt function is applied, based on Mughrabi's composite model (1983). Mughrabi (1983) concluded that, after cyclic loading, the energetically-preferred dislocation-pattern structures co-existed with the softer randomly-distributed dislocations.

The single-peak fitting (Daymond *et al*., 1997) with the General Structure Analysis Software (GSAS) is performed (Larson and Von Dreele, 2004). At room temperature, cyclic testing was performed using the high-precision extensormeter under fully-reversed cyclic-loading conditions at constant maximum (ε_{max}) and minimum strain (ε_{min}) amplitudes of + *1%* and - *1%*, correspondingly. The cyclic frequency was *1 Hz*. The initial loading was tensile, which resulted in the plastic deformation, as pointed in Figure 5-2. The following fatigue data was collected at different cycles of the 1^{st}, 10^{th}, 100^{th}, 250^{th}, 500^{th}, $1{,}000^{th}$, $1{,}500^{th}$, $2{,}000^{th}$, and $2{,}500^{th}$ cycles, respectively.

Within these specific fatigue cycles, *seven points* along the hysteresis loop for a given cycle were chosen for the neutron-diffraction measurements, as exhibited in Figure 5-2. These *points* coincide with the maximum tensile (*Pts 1 and 7*) and the maximum compressive strain *point* (*Pt 4*), the two zero-strain *points* (*Pts 3 and 6*),

and the two zero-stress *points* (*Pts 2 and 5*). The applied stresses at the maximum tension (*Pt 7*) and the maximum compression (*Pt 4*) as a function of the fatigue cycles are presented in Figure 5-3 to distinguish the hardening (1^{st} ~ 100^{th} cycles), softening (100^{th} ~ $1{,}000^{th}$ cycles), and saturation ($1{,}000^{th}$ ~ $2{,}500^{th}$) fatigue cycles. The detailed stress evolution is discussed later.

The fatigue-life time of this specimen was 2,925 cycles, as shown in the inset of Figure 5-3.

The high-resolution thermocouples were attached to simultaneously measure the heat generation and absorption corresponding to the external stress controlled by the load frame. The data recording synchronizes with the in-situ stress-strain curves and neutron-diffraction measurements. The thermocouples are highlighted by the dashed arrows in Figure 5-1. The thermocouples were attached on the sample out of the neutron-gauge volume to avoid the additional scattering for the neutron-diffraction profile analysis.

5.3. Results

Low-cycle-fatigue Experiments

The strain amplitudes were held constant during cycling. Figure 5-2 illustrates a stress-strain loop under strain-controlled cycling. During initial loading, the stress-strain curve is marked as monotonic tension, where yielding is observed before the 1^{st}-fatigue cycle. On unloading, the plastic strain is seen at *Pt 2* (*0 MPa*). The compression to a - *1%* strain (*Pt 4*) shows a nonlinear stress-strain response. In

reloading in tension through *0 MPa* (*Pt 5*), *0%* (*Pt 6*), and + *1%* strain (*Pt 7*), the hysteresis loop develops. Kuhlmann-Wilsdorf and Laird (1976) emphasized the importance to investigate the fatigue progress within one fatigue cycle. Thus, the in-situ measurements of both the neutron diffraction and the bulk stress/temperature were conducted to study the microstructural evolution upon the loading paths between the *points* within one specific fatigue cycle, which is discussed later.

Since the fatigued-induced-plastic deformation is not completely reversible (Dieter, 1986), modifications to the structure occur during cyclic deformation resulting in the local stress-strain redistribution. The stresses of the + *1%* tension (*Pt 7*) and - *1%* strain (*Pt 4*) at the selected fatigue cycles in Figure 5-3 show roughly the following five stages:

(1) Stage 1: initially, the increase of peak stresses in both tension and compression with escalating fatigue cycles demonstrates cyclic hardening up to the 100^{th} cycle. At the 100^{th} fatigue cycle, the peak stresses of tension and compression are + *591* and - *587 MPa*, respectively.

(2) Stage 2: the specimen, then, undergoes cyclic softening, which leads to a continuous decrease of the stress from the 100^{th} to the $1{,}000^{th}$ cycles.

(3) Stage 3: after the $1{,}000^{th}$ fatigue cycle, the stress-strain curves stabilize, and the specimen arrives at steady stresses. The averages of the stresses at + *1%* (*Pt 7*) and - *1%* (*Pt 4*) strains during fatigue cycling are + *543* ± *2* and -*537* ± *1 MPa*, respectively. The specific stresses are shown in Table 5-1.

(4) Stage 4: from the inset of Figure 5-3, a very slight secondary cyclic-softening region can be observed within the $2{,}800^{th}$ fatigue cycle. The applied tensile stress, then, decreases sharply after the $2{,}800^{th}$ cycle due to the nucleation and the advancement of the macrocracks. There is a tension-compression asymmetry of the stress levels, as marked in dashed arrows of the inset in Figure 5-3. With the same $|1\%|$ strain, the stress levels of tension become much smaller than those of the compression at each identical fatigue cycles. The result suggests that the fatigue cracks reach a certain critical length so that the remaining cross section cannot support the applied load evenly.

(5) Stage 5: Failure, the final fatigue fracture happened at the $2{,}925^{th}$ cycle, marked in the inset of Figure 5-3.

Heat Generation and Absorption within One Fatigue Cycle

It has long been recognized that the mechanical energy can be separated into the stored energy of cold work and thermal energy (Dieter, 1986). Einstein's, Debye's, and Grüneisen's (Girifalco 2000) models unify the elastic deformation with thermodynamics. New approaches are proposed to model the stored energy of the deformed microstructure (Wong *et al.*; Rittel *et al.* 2006; Huang *et al.* 2009). More specifically, the thermal-mechanical behavior of the low-cycle-fatigue experiments on the metallic alloys has been well documented (Jiang *et al.* 2004; Chen *et al.* 2004, Yang *et al.* 2005).

In this study, a different temperature measurement is applied to investigate the temperature evolution upon the monotonic tension and within the specific fatigue cycles, coupled with in-situ neutron-diffraction measurements. When the specimen is held for collecting the statistically-sufficient neutron-diffraction data, the temperature of the gauged region reaches the thermally-balanced states with the equilibrium among the heat conduction, convection, and radiation. The temperature evolution within one fatigue cycle is shown in Figures 5-4a, b, c, and d of the 1^{st}, 10^{th}, 250^{th}, and $2{,}500^{th}$ fatigue cycles, respectively. The measurements from both thermocouples practically show the same features. The data of the thermocouple away from the hydraulic system, which controlled the loading states, is described in detail below.

As shown in Figure 5-4a, the increase of the temperature is first noticed when the monotonic tension strain is applied in the range of *0.8%* to *+ 1%*. It is not surprising that after the yielding point, within the initial monotonic-tension region (path *OA* in Figure 5-2), the microscopic inhomogenieties from tensile-deformation-induced dislocations, coupled with the stress-stain curve of the monotonic tension shown in Figure 5-2, result in the internal friction (Zener 1937). The monotonic-tension-induced microstructure developing during the initial-monotonic-tension load can be understood from the earlier reported results (Huang *et al.*, 2008b).

When the strain reached *+ 1%* (Point 1) at about the $5{,}100^{th}$ second, the specimen is, then, held for about *15 minutes* for the neutron measurements. Meanwhile the temperature fluctuations reach the steady state. The specimen is, then, unloaded to *0 MPa* (*Pt2*) at about the $6{,}000^{th}$ second. There is a corresponding instant

peak-temperature increase to *304.29K*. The temperature profile, then, decreases to the equilibrium at about *304.2K*. It is due to the heat conduction of the stress inhomogenieties (Zener, 1938). The same inhomogeneous temperature distribution for heat conduction has been recorded by the high-spatial-resolution, infrared-thermography camera on the same alloy (Huang *et al.* unpublished) and the other alloys (Jiang *et al*. 2004; Yang *et al.* 2005). In the current study, using the thermocouples, the time-dependent temperature evolution reveals the similar heat-conduction feature in all the measurements. As a result, during cyclic deformation, the specimen expansion and contraction under the external stress is accompanied by the localized elastic/plastic strains. They are related to cyclic deformation due to the constraint effect of the larger surrounding mass of essentially elastically-deformed neighboring grains (Dieter 1986). The grains, then, absorb and/or generate the heat. Within the compression paths of the 1st-fatigue cycle, the highest increase of the temperature reaches *304.75K* at the maximum compression (*Pt 4*) of about the *7,700th* second.

Upon the subsequent tension loading to *0 MPa* (*Pt 5*) at about *8,400th* second, the temperature drops to a local minimum at *304.38K*. The decrease of the temperature (ΔT) occurs due to the increase of the tension stress ($\Delta\sigma$). The correlation qualitatively appears as the thermoelastic effect corresponding to the equation of

$$\Delta T = -KT\Delta\sigma\,, \tag{5-1}$$

where T is the temperature (degree Celsius, ^0C) of the current state, and K is a material constant ($K = \bar{\alpha}/\rho C_V$). The parameters are reported in the manual of the HASTELLOY® C-22HS™ alloy: $\bar{\alpha}(= 11.6 \mu m/m - ^0C)$ is the coefficient of the linear thermal expansion, $\rho = 8.6 g/cm^3$ is the mass density, and $C_V = 412 J/kg - ^0C$ is the specific heat at a constant volume. The cooling of the specimen upon tension is also found from *0 MPa* to *0%* strain at *Pt 6* and at about the $9{,}200^{th}$ second. A more profound temperature decrease is observed, while the specimen is pulled to + *1%* strain (*Pt 7*) at about $10{,}000^{th}$ second. Within the 1^{st} cycle, there is a clear negative relationship between the applied stress and the temperature response according to Equation (5-1). With the same tensile loading, the heat absorption upon cyclic loading (*Pt 7* at the $10{,}000^{th}$ second) contrasts to the heat generation during the monotonic tension (*Pt 1* at the $5{,}100^{th}$ second). The different temperature evolution reflects the deformation mechanisms changing from the initial-monotonic-tension region at the $5{,}100^{th}$ second to cyclic tension at the $10{,}000^{th}$ second. At the 10^{th} cycle, as shown in Figure 5-4b, the temperature-stress correlation, within one fatigue cycle and in other higher-number cycles, follows the similar thermoelastic response as the deformed specimen generates the heat upon compression (*Pts 2, 3, and 4*) and absorbs the heat during the tension (*Pts 5, 6, and 7*). There are only two distinguishable features found in the tension portion of the hysteresis loop (upper part) after the 250^{th} cycle. The difference shown in Figure 5-4c is described below:

(1) The major heat absorption is found within the range of *0 MPa* to *0%* strain at *Pt 6* and at about the $33{,}000^{th}$ second, but not at *Pt 7* and at about the $34{,}200^{th}$ second.

(2) There is a heat generation observed as a temperature peak during the strain increase from *0%* to *+ 1%* strain at *Pt 7*, which would be discussed in terms of the generation of the randomly-distributed dislocation as a function of the fatigue cycle later.

The same features are found in the rest of the fatigue cycles. The details are described later in terms of the microstructure evolution. The $2{,}500^{th}$ cycle, shown in Figure 5-4d, is selected because it's the last measurement before the final failure at the $2{,}925^{th}$ cycle.

A summary of the bulk-parameter evolution within one cycle as a function of the fatigue cycle is presented in Figure 5-5. The differential stress (square) and the temperature (circle) from compression (*Pt 4*) to tension (*Pt 7*) are calculated using Equations (5-2) and (5-3), respectively:

$$\delta\sigma = \sigma_{+1\%}^{Pt7} - \sigma_{-1\%}^{Pt4} \tag{5-2}$$

$$\delta T = T_{+1\%}^{Pt7} - T_{-1\%}^{Pt4}. \tag{5-3}$$

Here the stresses (σ_{strain}^{Point}) and the temperatures (T_{strain}^{Point}) are recorded at the moments when the temperature fluctuations reach the steady state. A transition, at the 100^{th} fatigue cycle, from hardening (stage 1) to softening (stage 2) cycles is seen in both the

stress and temperature evolution. The ideal thermoelastic response (blue solid line) is calculated in proportion to the deformed fraction of the specimen using Equation (5-1). The experimentally-measured temperature evolution (red circles in Figure 5-5a) has the same trend as the ideal thermoelastic response. However, the absolute values of the experimental-temperature changes are smaller than those calculated for ideal thermal responses (a blue solid line) in Figure 5-5a, up to the 500^{th} fatigue cycle. While the specimen is subjected to cyclic loading, both the elastic and plastic deformations take place simultaneously. The stress responses from the elastic components are indeed lower than the measured stress changes (squares). It is important to note that cyclic loading shows the intrinsic thermoelastic trend except for the stage 3 ($1{,}000^{th} \sim 2{,}500^{th}$ cycles). During stage 3, the temperature change does not correlate to the steady stresses, as shown in Table 1 and Figures 5-3, which are discussed in terms of the microstructure below.

The above results of correlating the thermal-mechanical responses have centered on the observation of the steady plastic deformation that is undisturbed in stage 3, as shown in Figure 5-3, of the fatigue deformation. Practically, the thermo-mechanical relationships are inevitably affected by defects. The foreseeable different types of the lattice imperfections, isotropic inhomogenieties, and other types of the fatigue damage can degrade the thermal current. The aim to assess the fatigue-induced plastic deformation can also be estimated by the thermal conductivity (λ), which is calculated from the data concluded from both thermocouples. As shown in Figure 5-1, one thermocouple is attached at the hydraulic-motor side, and the thermo-

data presented above is from the other side. There is a constant heat flux between these two thermocouples from the hydraulic-motor side, as calculated below.

$$Q_x = -kA\frac{dT}{dX} \tag{5-4}$$

Q_x is the heat-transfer rate (W); $k = 11.8W/m-^0C$ is the thermal conductivity of the alloy; A is the cross-sectional area of the current specimen; dT is the temperature difference measured from the two thermocouples; dX is the length of the heat transfer between two thermocouples. As already shown in Figure 5-2, with a 0% strain, the heat-transfer length (dX), and, hence, the cross section (A) are identical. The temperature profiles of *Pt 6* are calculated, and *Pt 6* is at the fixed strain level at 0%. The temperature differences between two thermocouples (Figure 5-1) of Pt 6 (dT_{Pt6}) are used to calculate the effective-heat-conduction rate ($\lambda_{Effective}$) as

$$\lambda_{Effective} = \frac{Q_x^{Pt6}}{Q_x^0} \times 100\% . \tag{5-5}$$

Q_x^0 and Q_x^{Pt6} are heat-transfer rates, defined in Equation (5-4), before and during the cyclic loading, respectively. The evolution of $\lambda_{Effective}$ is shown in Figure 5-5b. The results can be interpreted with Ashby's (1989) conclusions of the thermal conductivity for the metals,

$$\lambda = \frac{1}{3} \times C_e \times \bar{c} \times l \,. \tag{5-6}$$

C_e is the electron-specific heat per volume, $\bar{c}$ is the electron velocity, and l is the electron mean-free path, which relates to the microstructures. When the disordered atoms scatter the electrons, the decrease of l reduces λ.

Together with the ideal thermoelastic prediction (solid blue line) in Figure 5-5a, $\lambda_{Effective}$ reflects the transitions of the measured temperature changes (red circles) at the 100th and the 1,500th cycles. The scheme in the Figure 5-5c concludes that these features as the bulk stress and temperature are the sum of the concurrent elastic and plastic deformation upon cyclic loading. Moreover, the simultaneously-collected neutron-diffraction data are analyzed to further address these characteristics in terms of the microstructural features, such as the lattice strain and the dislocation parameters.

In-situ Neutron-diffraction Measurements

The key to understand the macroscopic temperature-stress relationship is to study the fatigue-induced microstructure development (Girifalco, 2000), such as the lattice-strain and the dislocation-structure evolution as a function of the external stress and the number of fatigue cycles. The in-situ neutron-diffraction results allow the determination of these microscopic parameters.

Lattice-strain Evolution

Peak positions (d^{hkl}) of specific lattice planes are refined for the calculations of the lattice strain, ε^{hkl}, as shown in Equation (5-7):

$$\varepsilon^{hkl} = \frac{d^{hkl} - d^{hkl}{}_0}{d^{hkl}{}_0} \times 10^6 (\mu e). \qquad (5\text{-}7)$$

d_0 is the peak position before the deformation as the reference. The lattice-strain evolution of the *111* plane under + *1%*-tension (*Pt 7*) in both transverse and loading directions is presented in Figures 5-6a and b, respectively. In the early fatigue cycles, the lattice strain and stress show an essentially linear behavior. The evolution of other face-centered-cubic (f.c.c.) peaks, such as 200, 220, and 311, at a + *1%*-macroscopic strain follows the similar linear relationship (Huang *et al*. 2007). This characteristic agrees with the thermoelastic trends shown in Figures 5-4a, b, and 5a up to the 500th cycle.

The lattice strain-stress dependence, in the loading direction in Figure 5-6b, starts to deviate from linearity after the 250th-fatigue cycle, when it is *8.5%* of the fatigue life (*2,925* cycles). Comparing to the lattice-strain development in the transverse direction (Figure 5-6a), the Poisson relationship (υ) can be found within the hardening cycles, where

$$\upsilon = \left(\frac{-\varepsilon_{transverse}}{\varepsilon_{loading}} \right). \quad (5\text{-}8)$$

$\varepsilon_{loading}$ and $\varepsilon_{transverse}$ are the strains of the identical specimen in the loading and in the transverse directions, respectively. The same trend is seen in a stainless steel (Lorentzen *et al.* 2002). However, as enlarged in the inset of Figure 5-6, the strain-stress relationship deviates from linearity at the 250^{th}-fatigue cycle. Two detector banks collect the neutron diffraction from two mutually orthogonal sets of the grains with different orientations. The lattice-strain anisotropy related to the orientations of the gauged grains is found for these two sets of the grains. In the final saturation cycles, the lattice strain decreases in the both groups of the grains in the loading and transverse directions. The intrinsic difference of such a decrease in the lattice strain-stress dependence is that the additional compression is found in the transverse direction, as shown in the inset of the Figure 5-6a. The lattice strain in the transverse direction changes from $-830.4 \pm 45.0 \mu e$ ($1{,}000^{th}$ cycle) to $-864.0 \pm 45.0 \mu e$ ($2{,}500^{th}$ fatigue cycle), indicating higher compression with increasing the cycles from 1,000 to 2,500th cycles. However, there is less and less tensile lattice strain in the loading direction, as enlarged in the inset of Figure 5-6b. The lattice strain reduces from $2{,}105.9 \pm 33.6 \mu e$ of the $1{,}000^{th}$ cycle to $2{,}019.6 \pm 35.0 \mu e$ of the $2{,}500^{th}$ fatigue cycle in the loading direction. The lattice-strain ratio for the loading direction after 500 cycles does not follow the earlier Poisson's relationship of nickel, which is about 0.31 (Kumar *et al.* 2003).

Similar to the tension part of the fatigue cycles, there are linear lattice strain-stress dependencies for the compression (*Pt 4*), following the Poisson's relationship in the loading directions presented in Figures 5-6c and d, respectively. In stage 3 ($1{,}000^{th} \sim 2{,}500^{th}$ cycles), the additional lattice-strain compression can be found in the loading direction from $-2{,}201.9 \pm 32.6\,\mu\varepsilon$ at $1{,}000^{th}$ cycle to $-2{,}221.0 \pm 33.1\,\mu\varepsilon$ at the $2{,}500^{th}$-fatigue cycle (inset of the Figure 5-6c). However, in the transverse direction, there is less tension i.e., the lattice strain is declining from $561.6 \pm 20.6\,\mu\varepsilon$ ($1{,}000^{th}$ cycle) to $504.0 \pm 19.2\,\mu\varepsilon$ ($2{,}500^{th}$ fatigue cycle), as shown in the inset of Figure 5-6d.

The anisotropy of the lattice-strain responses of individual fatigue cycle subjected to grain orientations, relative to the loading direction, is calculated as P_{ratio}, which is defined as:

$$P_{ratio} \equiv P_{Tension/compression} = \frac{-\left(\varepsilon_{transverse\ direction}\right)}{\varepsilon_{loading\ direction}}. \tag{5-9}$$

Note that P_{ratio} is defined to easily distinguish the lattice-strain evolution subjected to different loading types (tension/compression) and different groups of the grains (loading/transverse directions). As will be discussed in more detail below, the loading-direction dependence shows the asymmetry of tension-compression responses in Figure 5-7a. It is evident that the Bauschinger effect occurs upon the fatigue damage. The upper part of Figure 5-7b is the evolution of the lattice strains in

the loading direction for both tension (blue-solid line), and compression (red-dotted line). The bottom part shows the evolution of the tension (blue line and symbol) and compression (red-dashed line), respectively, in the transverse direction. The bulk cyclic hardening-softening transition is clearly visible from the lattice-strain evolution within *250*-fatigue cycles. At higher-cycle numbers during Stage 3, the large variations of the lattice strain are observed during $1{,}000^{th} \sim 2{,}500^{th}$ cycles, as indicated by dashed green squares in Figure 5-7b, although the stresses are macroscopically steady (Table 1 and Figure 5-3). The details are discussed later. For further understanding, the dislocation-structure development determined via the neutron-diffraction-profile analyses is described below.

Evolution of the Dislocation-structure Parameters

It seems almost certain that there are two types of dislocation structures developing in our case close to Mughrabi's composite model (1983). There are hard patterned-dislocation groupings and the soft interiors with the randomly-distributed dislocations. The formation of the hierarchical dislocation structure in many metallic polycrystalline materials under the fatigue damage has been previously described (Kuhlmann-Wilsdorf and Laird, 1977; Laird *et al.,* 1986). It is known that the randomly-distributed dislocations correspond to the Gaussian-broadening components in the reciprocal space (Zehetbauer, 1993; Hughes and Hansen, 1993; Krivoglaz, 1996; Barabash; 2001, and Schafler et al., 2005). Meanwhile, the patterned-dislocation structure with the planar-dislocation walls could be detected by the

Lorentzian-broadening components. To distinguish these two broadening components, Balzar *et al.*-like approach (2004) was used to deconvolute the broadening components. The pseudo-Voigt function is applied for the profile analysis as

$$V = \eta L + (1-\eta)G\,. \qquad (0 \le \eta \le 1) \qquad (5\text{-}10)$$

A parameter (η) is introduced as a variable portion of the pure Lorentzian (L) to pure Gaussian (G), where L and G are defined as Gaussian and Lorentzian peak widths, respectively. The equations to quantify the dislocation evolution are documented (Huang *et al.* 2008a), based on Barabash's (2001, 2003) and Krivoglaz's (1996) methods. More specifically, the dislocation calculations set forth in this section are based on the peak-width change of the (*200*) peaks, which is known to be most sensitive to the plastic deformation (Hutchings *et al.* 2005). In Figure 5-8c, the dislocation density (n) and the distance between the patterned-dislocation planar-wall structures (D) are estimated at the maximum tension of *+ 1%* (*Pt 7*). D is defined in Figures 3-1 and 4-6b. The approach is similar to the procedures described by Huang *et al.*, 2008a. Upon cyclic hardening, the dislocation density increases accordingly in both directions. The formation of the new patterned-dislocation-planar walls also decreases the average-distance (D) between them. After the 100^{th} cycle, the invariant of D indicates that the average size of the patterned-dislocation-planar-wall structure start to stabilize. However, the density of the randomly-distributed dislocations (n)

keeps fluctuating during the fatigue cycles. These trends are further discussed later by demonstrating the dislocation-parameter changes from the adjacent macroscopic stress/strain states within one fatigue cycles.

Dislocation-structure Evolution as a Function of Fatigue Cycles

Up to the 100th-fatigue cycle, cyclic hardening is accompanied with the increase of the randomly-distributed-dislocation density (n). The decrease of the distance (D) between the patterned-dislocation-wall structures is observed, too. The maximum densities are $1.77 \times 10^{9} cm^{-2}$ at the 100th-fatigue cycle and $1.95 \times 10^{9} cm^{-2}$ at the 250th cycle in the loading and transverse directions, respectively. Upon cyclic softening, the opposite trends indicate the annihilation and the rearrangement of the dislocations. Although the estimated amount of the dislocation density is slightly smaller than other fatigued polycrystal-nickel alloys (Segall *et al*., 1961), the randomly-distributed-dislocation-density evolution correlates with the macroscopic-temperature evolution in Figure 5-5a, the effective heat conduction ($\lambda_{effective}$), as shown in Figure 5-5b, and the lattice-strain evolution of Figure 5-7b of the transitions between the fatigue stages. Unlike the fluctuating dislocations density subjected to cyclic loading, the patterned-dislocation-structure size (D) almost stabilize. The evolution of the dislocation-structure parameters agrees with Essmann and Mughrabi's conclusions (1979) about the formation of the stabilized dislocation-wall structures during fatigue. In the discussion section, we will explicitly study the evolution of the dislocation-structure parameters within one fatigue cycle. To do so,

the fundamental property of the diffraction experiments is established on the recognition that the quantitative estimations of the dislocation structures demonstrate the evolution.

5.4. Discussion

Anisotropy of Lattice-strain Evolution

The lattice-strain evolution reveals the fatigue-damage development. Observations of the lattice-strain evolution in different stages in this study are compared with the others' investigations of the fatigue-mechanism transitions. Thompson (1959) reported that the earliest time for the fatigue crack nucleation, as the transition of the fatigue-damage stages, could range from 1% to 10% of the fatigue life. Later on, in the earlier analyses of the fatigue behavior, Tompkins (1968) also described the fatigue damage via the formation of the fatigue cracks. In the current study, the deviation of the linear lattice strain-stress evolution occur during stage 2, approximately within the range of the $100^{th} \sim 250^{th}$ fatigue cycles, which are within the range of 3.5% ~ 8.5% of the fatigue life (2,925 fatigue cycles). The cyclic-softening region during stage 2 is comparable to the above Thompson's observations (1959) in terms of the portion of the fatigue life. Laird and Smith (1962) describe the anisotropy of the fatigue damage as the fatigue-crack growth nucleating in the transverse direction, perpendicular to the principal tensile stress, which releases the tensile load without the re-cohesion.

In this study, to quantitatively compare the lattice strain-stress anisotropy in the loading direction, the (ε^{111}) lattice-strain evolution with the number of cycles is presented in Figure 5-7b. The lattice strains for the tension (*Pt 7*) and compression (*Pt 4*) are shown in blue and red, respectively. The upper part of Figure 5-7b shows ε^{111} in the loading direction for tension (*Pt 7*) and compression (*Pt 4*) in solid and dotted lines, respectively. The right-hand-side y-axis of Figure 5-7b has an opposite sign shown in red of the ε^{111} under the compression (*Pt 4*) for the convenience. At the 2,500th cycle, $\varepsilon^{111}_{Tension}$ and $\varepsilon^{111}_{compression}$ are $+2{,}019.6 \pm 35.0(\mu e)$ and $-2{,}221.0 \pm 33.1(\mu e)$, respectively.

In Figures 5-7b, the bottom part is the ε^{111}-strain in the transverse direction for tension (line and square symbols) and compression (dashed line), respectively. At the 2,500th cycle, $\varepsilon^{111}_{Tension}$ and $\varepsilon^{111}_{compression}$ are $-864.0 \pm 45.0(\mu e)$ and $+504.0 \pm 19.2(\mu e)$, respectively. The similar fatigue-damage anisotropy can be calculated in terms of the greater disparity of the lattice strain in the transverse direction ($\left\|\varepsilon^{Transverse}_{compression}\right| - \left|\varepsilon^{Transverse}_{tension}\right\| = 360\mu e$) than that of the loading direction ($\left\|\varepsilon^{Loading}_{compression}\right| - \left|\varepsilon^{Loading}_{tension}\right\| = 201\mu e$), developed gradually from stages 2 into 3, as shown in Figure 5-7b.

A more clear tension/compression anisotropy can be seen in the evolution of the P_{ratio} (Figure 5-7a). $P^{Tension}_{ratio}$ and $P^{Compression}_{ratio}$ are the P_{ratio} under + *1 %* tension (*Pt 7*) and – *1%* compression (*Pt 4*) deformation, respectively. Within the 250th fatigue

cycles, both $P_{ratio}^{Tension}$ and $P_{ratio}^{Compression}$ are close to the Poisson ratio of the pure nickel ($\upsilon = 0.31$) in Figure 5-7a.

However, when the number of the fatigue cycles exceeds the 500th cycle, $P_{ratio}^{Tension}$ grows and becomes higher than the $P_{ratio}^{Compression}$ of the 1st cycle. On the other hand, $P_{ratio}^{Compression}$ decreases. At the 1,000th-fatigue cycle, $P_{ratio}^{Compression}$ becomes smaller than $P_{ratio}^{Tension}$ of the 1st-fatigue cycle. The decrease of $P_{ratio}^{Compression}$ is understood from Equation (5-9): the $\left|\varepsilon_{loading}\right|$ becomes larger, which can be seen as the greater compression of *Pt 4* in the loading direction (Figure 5-6c). Similarly, $P_{ratio}^{Tension}$ turning out to be greater because $\left|\varepsilon_{transverse}\right|$ develops into larger compression of *Pt 7* in the transverse direction (Figure 5-6a).

From the standpoint of the above discussion, the irreversible anisotropy of the P_{ratio} observed during the stages 2 and 3 (Figure 5-7a) suggests that the fatigue-damage stages should be discussed in terms of the plastic deformation and the evolution of the dislocation substructure.

Dislocation-parameter Evolution within One Fatigue Cycle

To understand the above models, the knowledge about the changes of the dislocation-structure parameters within one-fatigue cycle is crucial. The fluctuations of the differential changes in dislocation-structure parameters within each fatigue cycle are summarized in Figure 5-9. The evolution of the patterned-dislocation-wall-structure spacing (δD) in loading and transverse directions are demonstrated in

Figures 5-9a and b, respectively. The changes of the differential random-dislocation density (δn) of the loading and transverse directions are presented in Figures 5-9c and d, respectively. Here, four paths are selected to be compared, as emphasized by Kuhlmann-Wilsdorf and Laird (1976), to present the detailed evolution within one fatigue cycle as

(1) Compression from zero stress (*Pt 2*) to zero strain (*Pt 3*) shown as black solid lines in Figure 5-9;

(2) Compression from zero strain (*Pt 3*) to maximum compression (*Pt 4*) (red dashed lines in Figure 5-9);

(3) Tension from zero stress (*Pt 5*) to zero strain (*Pt 6*) (blue dashed-and-dotted lines in Figure 5-9), and

(4) Tension from zero strain (*Pt 6*) to maximum tension (*Pt 7*) (green dotted lines).

The differences of the averaged patterned size (δD) and the differences of the dislocation density (δn) of these macroscopic paths between the nearby *points* within one fatigue cycle are written in Equations (5-11) and (5-12), respectively, as

$$\delta D = D^{Point(N)} - D^{Point(N-1)} \tag{5-11}$$

$$\delta n = n^{Point(N)} - n^{Point(N-1)}. \tag{5-12}$$

Figure 5-9a shows the evolution of the quantities of δD in the loading direction. The fluctuations are greater in the earlier hardening cycles, which converge in the later

cycles. The comparison of the differential parameters before and after the hardening cycles indicates that the patterned-dislocation structure becomes more and more stable with greater fatigue cycles in the loading direction. Statistically, from *Pts 3 to 4* in compression (red dashed lines), *Pts 5 to 6* in tension (blue dashed-and-dotted lines), and *Pts 6 to 7* in tension (green dotted lines), the negative value of the differential patterned-dislocation-wall spacing (δD) indicates the number of planar-dislocation-wall structures increases, resulting in the decrease of the size, *D*. On the other hand, the positive value of δD observed from *Pts 2 to 3* (black solid line) demonstrates that the distances (*D*) between the patterned-dislocation structures increase. The greater average *D* values suggest the decrease of the total amount of the patterned-dislocation structure. The evolution of the dislocation substructure accumulated within one fatigue cycle results in the overall decrease of *D* in the loading direction up to the 500^{th} cycle, as shown in Figure 5-8c. In Figure 5-9c, the positive values of (δn) from *Pts 2 to 3* (black solid lines) and *Pts 3 to 4* (red dashed lines) in compression show the dislocation generation. There is practically no dislocation-density generation ($\delta n \sim 0$) until the 10^{th} cycle of *Pts 6 to 7* in tension (green dotted lines). However, the annihilation of the randomly-distributed dislocations is observed as *Pts 5 to 6* in compression (blue dashed-and-dotted lines). The more progressive dislocation generation (δn) is observed after the 10^{th}-fatigue cycle. The dislocation annihilation (δn) is not observed from *Pts 2 to 3* in compression (black solid lines) and *Pts 5 to 6* in tension (blue dashed-and-dotted lines), respectively, until the 100^{th}-cycles. Similarly, the accumulation of dislocation-

density differential changes (δn) within each cycle causes the increase of the total dislocation density (n) in Figure 5-8c. Figures 5-9b and d show the evolution of the parameters (δn and δD) in the transverse direction, respectively. These Figures 5-5 demonstrate that the patterned structure also becomes more stable upon greater fatigue cycles in the transverse direction. The change of the randomly-distributed-dislocation-density differential (δn) is shown in Figure 5-9d. Unlike in the loading direction, the generation of the random dislocations from *Pts 6 to 7* (green dotted lines) in tension does not decrease after cyclic hardening. The increase of the differential dislocation density (δn) from *Pts 3 to 4* (red dashed lines) in compression is also much greater than that in the loading direction. In the transverse direction a local minimum is observed in the dislocation density fluctuations at the 1,500th-fatigue cycle. The minima in fluctuations of the dislocation parameters are observed for the paths of *Pts 3 to 4* (red dashed lines) in compression and *Pts 5 to 6* in tension (blue dashed-and-dotted lines). The minima are correlated with the local lattice-strain fluctuations, marked in green boxes, in stage 3 (Figure 5-7b). According to Szekely *et al*. (2001) and Schafler *et al*. (2005), the occurrence of the minimum/maximum in the differential-dislocation-density fluctuations is characteristic of the second-order structural transformation taking place in the dislocation substructure. Such a transformation indicates that the reduction of the randomly-distributed-dislocation density may come from the self-organization and the formation of the patterned-dislocation-wall structure. The later is accompanied by the reduction of the average distances (δD) observed in Figure 5-9b. The transitions of the dislocation-structure

parameter fluctuations within one fatigue cycle and their accumulation in the overall fatigue cycles lead to the irreversible fatigue damages upon different fatigue levels.

Anisotropy of the Dislocation Parameters

The anisotropy between the dislocation-parameter evolution within one fatigue cycle for two distinct orthogonal groups of grains diffracting in the two detector banks is discussed below. There are more profound fluctuations (both generation and annihilation) of the randomly-distributed dislocations (δn) found in the transverse direction (Figure 5-9d) than those of δn in the loading direction (Figure 5-9c). The greater generation and annihilation of the random-dislocation density in the transverse direction coincide with the greater disparity of the lattice-strain evolution in the transverse direction (Figure 5-7b). The above microscopic-dislocation-structure-parameter anisotropy in the transverse direction correlating with the lattice-strain anisotropy in stage 3, and agrees with Laird and Smith's (1962) anisotropic-decohesion description for the crack-propagation direction. The comparison given here relates the microscopic-dislocation-structure parameters with the thermodynamics quantities, such as the temperature and external pressure during fatigue cycles.

Correlation between the Dislocation-density and Temperature Fluctuations

As discussed above, the heat-absorption changes under tension within one fatigue cycle as shown in Figures 5-4a, b, c, d, and 5a. The corresponding dislocation-

density fluctuations (δn) between *Pts 5 to 6* (tension) and *Pts 6 to 7* (tension) correlates with the observed changes in thermal responses. As shown in the Figures 5-9c and d, the random-dislocation density only slightly increases from *Pts 6 to 7* within the first few cycles. A slight annihilation of the randomly-distributed-dislocation density is observed from *Pts 5 to 6*. These fluctuations of δn lead to the heat absorption at the *Pts 7* at the 1st and 10th fatigue cycles as shown in Figures 5-4a and b. However, upon the greater fatigue cycles in stages 2 and 3, the higher dislocations generation from *Pts 6 to 7* (tension) and the higher annihilation from *Pts 5 to 6* (tension) might cause the change in the overall heat absorption within one fatigue cycle from *Pts 7* to *Pts 6* of the fatigue cycles, shown in Figures 5-4c and d, and other fatigue cycles. It is known that stored energy is associated with dislocations (Mughrabi 1983; Biermann *et al.* 1993; Krivoglaz 1996, Kuhlman-Wilsdorf 1999). Regrouping of the dislocations within different kinds of dislocation-wall-patterned structures is favored by the reduction of the free energy per unit length of the dislocation line, E, due to the decrease of the upper cut-off radius determined by the characteristic size, D, of such a patterned dislocation structure:

$$E = \frac{Gb^2(1-\nu/2)}{4\pi(1-\nu)} Ln\, D/b \tag{5-13}$$

where G is a shear modulus and b is the dislocation Burgers vector. Moreover, the microstructure induces the residual-stress evolution upon cyclic loading (Quinn *et al.*

2004). This explains the observed correlation between the dislocation-density fluctuations and thermal response of the material.

The model presented in this paper gives a qualitative description of the reversible/irreversible-structure transitions during the fatigue-induced-plastic deformation. More detailed work with the spatially-resolved information is under way to reveal the local fatigue damages at the micro-scales.

5.5. Summary

(1) The microscopic ensemble-averaged neutron results and the bulk-property evolution upon cyclic loading show the non-monotonic development of the fatigue-induced dislocation sub-structures.

(2) The evolution of the dislocation structure and lattice strain reflects three distinct stages in the fatigue-damage development.

(3) The bulk cyclic hardening is the consequence of the increase of the dislocation density and the formation of the patterned-dislocation structures. The lattice-spacing development during fatigue is accompanied by the thermoelastic effect on the heat absorption and generation.

(4) The subsequent temperature evolution shows a non-monotonic behavior during the saturation cycles.

(5) The anisotropy between the loading and the transverse direction and the dislocation-structure parameters demonstrate the irreversible fatigue-deformation activities.

(6) The tension-to-compression asymmetry of the lattice-strain and dislocation-substructure-parameter evolution in the stage 3 ($1{,}000^{th}$ ~ $2{,}500^{th}$ cycles) reveals a significant Bauschinger effect.

(7) The lattice-strain evolution together with the change of the dislocation parameters and temperature dependence suggest that the second-order-type structural transformation occurs in the dislocation substructure during stage 3 (the saturation cycles within the $1{,}000^{th}$ ~ $2{,}500^{th}$).

Chapter 6: The Precipitation-strengthened Aged Alloy under Tension Deformation

The analysis methods studying the mechanical behavior, proposed in Chapter 2, have been established via investigating the annealed alloys, documented in Chapters 3, 4, and 5. The developed method is now applied to study the nano-precipitate effect on the aged alloy. In this Chapter, we investigate the aged alloy subjected to tensile deformation. The tensile behavior of the aged alloy was examined by in-situ neutron-diffraction, small-angle neutron-scattering (SANS) and transmission-electron microscopy (TEM) at room temperature.

For in-situ neutron diffraction experiments, the peak-width of the *hkl* planes from both the nano precipitates and the matrix were determined as a function of the stress. The evolution of the peak widths from the matrix and the precipitates, during the tension-loading experiments, demonstrated that the particle-shearing-mechanism effect strengthens the aged alloy.

The ex-situ SANS experiments and a theoretical model for SANS absolute intensity distribution, *I(Q),* were presented to extract the structural properties of the particle-shearing mechanisms. During the deformation process, a change in the morphology of precipitates was discovered. This microstructural information resolved by SANS is in a good agreement with the results obtained from the quantitative TEM image analysis. The TEM results and the irreversible precipitate-peak broadening, obtained from the in-situ neutron-diffraction experiments, are also consistent.

6.1. Introduction

In coarse-grained polycrystalline metals, dislocation activities, such as generation, propagation, interaction with microstructure, and even annihilation by other dislocations, govern the plasticity. The plastic structural consequences are accumulated, and, hence, can be measured by refining the Bragg peaks. However, the critical length scale to activate the dislocation is calculated based on the theoretical shear stress (Weertman 2002). The critical grain size for face-centered-cubic (f.c.c.) metals is about 20 to 40nm (Budrovic *et al.* 2004). The plasticity mechanism of the nanocrystalline metals, with mean-grain size below 100 nm, remains unsolved.

On the other hand, for the plastic deformation of the electrodeposited nanocrystalline nickel, Budrovic *et al.* (2004) reported that the peak broadening is reversible upon unloading. Their results suggest a different deformation mechanism acting in the nanostructured materials other than the dislocation activities in the coarse grains.

In this study, we show that upon the plastic deformation, a nano-particle-strengthened nickel alloy has the peak broadening from both of the nano particles and the coarse-grained matrix. Both of the nano and matrix grains show irreversible peak broadening. The results were acquired using in-situ neutron diffraction experiments. The diffraction peak-profile analyses are used to explain the interactions between the nano particles and the coarse-grained matrix. Small-angle neutron-scattering experiments with a stochastic phenomenological model fitting are applied to

quantitatively explain the morphology and structure information of the nano particles upon plastic deformation.

6.2. Materials

Corrosion-resistant nickel-based superalloys are widely used in engineering applications because of their strength and excellent resistance to a wide variety of corrosive environments. For instance, a newly-developed HASTELLOY® C-22HS™ Alloy obtained from the Haynes International, Inc. has been used in important infrastructures, such as the metallic lining, lower Colorado River power plant, and the mixed waste incinerator system, at the Los Alamos National Laboratory.

After a hot-rolling process, the alloy was mill annealed at 1,080^{o}C. In the mill-annealed condition, the alloy is in a face-centered-cubic (f.c.c.) structure with a grain size about 90 μm. A two-step heat treatment initialized by a 16-hour heat treatment at 705 ^{o}C, followed by a furnace cooling at 605 ^{o}C for another 32 hours (HASTELLOY Manual 2005), is applied for the precipitation. Note that the melting point is found to be 1,310 ^{o}C, which suggests that the precipitates are generated in a solid-state solution during the heat treatment (Arya *et al.* 2002).

It has been reported for doubling their mechanical performance with these $Ni_2(Cr,Mo)$ precipitates embedded in the f.c.c. matrix from the age-hardening heat treatment (Lu *et al.* 2007). Before the precipitation, the 0.2% yield strength of the alloys at room temperature is 376 MPa and becomes 690 MPa at room temperature after the precipitation. It is important to study the mechanical behavior of the aged

alloy, which doubles the strength while keeping the excellent ductility for more applications and new alloys design.

6.3. Experimental Results and Discussion

In-situ Neutron-diffraction Experiments

The room-temperature, in-situ neutron measurements were conducted with the Spectrometer for MAterials Research at Temperature and Stress (SMARTS) beamline of the Los Alamos Neutron Science Center (LANSCE). The gauge volume was 120 mm^3 for the measurements of the monotonic-tension experiments. The strain rate was 0.001 per second.

The neutron-diffraction profiles were refined by the General Structure Analysis System (GSAS) (Larson and Von Dreele 2004) for investigating the peak-position and peak width in this Chapter. A Gaussian function was used to fit each single peak. The refined peak positions of each *hkl* were calculated for lattice strain (ε_{hkl}), based on the change in the *d*-spacing (d_{hkl}) and the relative initial *d*-spacing (d^0_{hkl}) as shown in Equation 6-1:

$$\varepsilon_{hkl} = \frac{d_{hkl} - d^0_{hkl}}{d^0_{hkl}} \tag{6-1}$$

The peak-width was considered as the Gaussian broadening components. The profile shape functions used in profile fitting programs are shown in Equation 6-2:

$$G = I_0 \exp\left(-\ln 2\left(\frac{2\Theta - 2\Theta_0}{w} \right)^2 \right) \tag{6-2}$$

Here I_0 is peak intensity; w is half FWHM, and 2Θ is the peak position.

The fitted results of an aged specimen before deformation are shown in Figure 6-1. The fitted curve (line) described the observed data (cross) very well, assuming a face-centered-cubic (f.c.c.) matrix and Ni_2 (Mo, Cr) particles. Diffraction peaks from both phases were monitored. Among the whole diffraction pattern, the 011-peak of the precipitates does not overlap with other diffraction peaks from the other respective phase. As a result, this peak is better for monitoring the behavior of the precipitates.

Figure 6-2 shows that the *hkl* neutron-diffraction peak widths change as a function of the stress level during the tensile experiments. The peak width in Figure 6-2 is described by the Gaussian standard deviation of each individual peak. The scatter of the peak-width data from the precipitates, shown as hollow dots, comes from the relatively smaller diffraction intensity as shown in Figure 6-1. The peak-widths of the matrix diffraction peaks are depicted as solid symbols in Figure 6-2. The entire matrix peaks start to broaden at the 0.2% yield strength, where the true stress is 625 MPa. The peak width of the precipitates-011 peak remains constant until 1,025 MPa.

The intrinsic peak-shape broadening of neutron-diffraction peaks can have several origins. Hutchings (2005) and Šittner *et al.* (2002) reported that the evolution of the peak-width is due to the change of the number of scattering sites. Jakobsen *et al.* (2006) reported that changes of the peak-widths come from the changes of the substructures of the grains. To sum up, the start of the peak-width broadening reflects the beginning of the plastic deformation.

More specifically, the peak-width observed in this study is mainly due to two reasons: first, the increase of the intergranular strains due to elastic and plastic anisotropy, and secondly the intragranular strains due to dislocation density.

In fact, because dislocations can produce severe short-range elastic strains, the peak-width could infer the dislocation density unless they are clustered into cells or at boundaries. Hence, we can assume that the increase in peak-width as shown in Figure 6-2 indicates the plastic deformation in both of the matrix and the particles.

Based on the different onsets of the peak-width broadening from the matrix and the precipitates, we can conclude the present study herein. When the true stress level is less than 625 MPa, both the matrix and the precipitates are elastically deformed. At the stress level between 625 MPa and 1,025 MPa, the matrix starts to plastically deform while the precipitates remains elastically deformed. Above 1,025 MPa, both of the matrix and the precipitates exhibit the plastic deformation.

These $Ni_2(Cr, Mo)$ precipitates as the strengthening particles plastically deformed at greater stress levels than those of the matrix. These particles could

involve the interaction between mobile dislocations in the soft matrix and the tougher $Ni_2(Cr, Mo)$ particles that act as obstacles to the motion of dislocations.

Below a true stress of 1,025 MPa, the particles were not cut so that the strain distribution might remain homogenous within the precipitates. Note that the bulk 0.2% yield strength is at 625 MPa. Hence, we cannot observe the peak-width broadening of the precipitates before the stress level of 1,025 MPa was reached. When the applied stress reached 1,025 MPa, the particle-shearing mechanism started. The nano particles, then, plastically deformed.

To sum up, these particles strengthen the aged alloy over the annealed condition. When the nano particles plastically deform, the particle-shearing mechanism leads to the broadening of their diffraction peaks.

A loading-unloading experiment was made to verify the particle-hearing mechanism described above. Again, we simultaneously measured all the peak widths as a function of the applied stress. Matrix-*111* and *311* peaks [Figures 6-3(a) and (b)] and precipitate-*101* and *011* peaks are plotted in Figures 6-3(c) and (d), respectively. The solid black squares are the peak widths (the full widths at half maximum, FWHM) measured when the specimen was under loading. On the contrary, the red hollow circles show the peak widths upon subsequently unloading.

From Figures 6-3(a) and (b), within 600 MPa, there is no peak broadening, under both loading and unloading-conditions, because it is the elastic-deformation region of the aged alloy. The same results are observed above when the aged alloy is subjected to the monotonic-tension experiments (Figure 6-2).

The onset of peak broadening and the irreversible peak-width evolution are then noticed beyond 700 MPa, which is the plastic-deformation region. The good agreement from monotonic tension and loading-unloading experiments demonstrate that the plastic deformation of the coarse-grained matrix was dominated by the dislocation activities.

Moreover, comparing to Figure 6-2, an identical onset of the peak broadening and the irreversible peak broadening of the precipitate peaks are also confirmed in Figures 6-3(c) and (d). The results suggest that the plastic deformation of the matrix and the precipitates are detected. Direct evidence was perceived by the transmission electron microscopy as described in below.

Transmission-electron-microscopy (TEM) Experiments

Complementary TEM analyses were performed at 200kV in a TECHNAI 20 electron microscope. Deformed samples for TEM were prepared from a slice cut at 45° to the loading direction to maximize the odds of having the slip plane parallel to the surface of the TEM sample. All the slices with a thickness of approximately 0.3 mm were cut. These slices were ground to a thickness of about 0.1 mm. Disks with a diameter of 3 mm were punched out for TEM. Electron-transparent thin foils were prepared by the twin-jet electro-polishing technique (T = 15^{o}C, Voltage = 25 V, and Current = 0.6 A), employing a solution containing 640 ml orthophosphoric acid, 150 ml concentrated sulfuric acid, 35 ml concentrated hydrochloric acid, and 210 ml

distilled water. The foils were observed in bright fields (BF), dark field (DF) and selected area electron diffraction (SAED) modes.

Lu *et al.* reported (2007) that the average size of the particles was 12 ± 10 nm. The volume fraction was about 25%. The recorded Cartesianized coordinates of the particles, as shown in Figure 6-4, are further analyzed to resolve the spatial distribution. The results will be compared with the SANS results in Table 6-1.

One slice was cut from the deformed sample after 30% monotonic-tension experiment as shown in Figure 6-5. The DF image in Figure 6-5 indicates that the dislocations cut some of the particles. Hence, the local inhomogeneous of the precipitate strains, introduced by the matrix dislocation, may cause the irreversible nano-particle-peak-broadening results discussed above. Note that only part of the precipitates located on the dislocation lines were cut.

TEM results have offered extensive direct observations of local structural characteristics for materials (Gleiter and Hornbogen 1967). However, in my current study, due to the finite sampling space, special care is required to extract the ensemble-average information from the taken image. Hence, small-angle neutron scattering experiments were introduced to follow up the TEM observations in next section. A quantitative comparison will be made.

Small-angle Neutron-scattering Experiments

The small-angle neutron-scattering (SANS) approach presents a complementary tool to the microscopy technique: It can provide nano-scale

information via the measurement of the Fourier transform of the spatial correlation function. However, the collected scattering intensity, *I(Q)*, is presented in reciprocal *Q* space and, therefore, to obtain quantitative real-space information, model fitting is required. In the study of nano-precipitates, the data analysis is inevitably compounded by the thermodynamically-driven polydispersity in the size of precipitates and the anisotropic inter-precipitate interference.

The focus of this Chapter is to present a model for SANS *I(Q)* to facilitate the application of SANS for the study of alloy precipitation strengthening. Our methodology has been described in Chapter 2 and is briefly shown as follows. In general, the inter-precipitate structure factor, *S(Q)*, is calculated via a stochastic phenomenological model. It is assumed that precipitates are partially ordered and separated from the nearest neighbors with a preferred distance, *L*, with a deviation measured by the root-mean square denoted by σ. The inter-precipitate structure factor (Giodano *et al.* 1991), *S(Q)*, is expressed as a function of *Q*, *L*, and σ

$$S(Q,L,\sigma)=2\cdot\left\{\frac{1-\exp\left[\frac{-(Q^2\sigma^2)}{4}\right]\cos(QL)}{1-2\exp\left[\frac{-(Q^2\sigma^2)}{4}\right]\cos(QL)+\exp\left[\frac{-(Q^2\sigma^2)}{2}\right]}\right\}-1 \tag{6-3}$$

The incoherent scattering, I_{INC}, is mainly determined by the measure of *I(Q)* in a high *Q* region. Based on a gradient-searching nonlinear least-squares fitting method, the SANS data is analyzed with the inclusion of instrumental resolution. It is

important to note that the coherent SANS intensity distributions obtained from the alloy can be fitted by the current proposed model uniquely with five parameters: R, ε, δ, L, and σ.

SANS measurements were carried out at the NG-7 SANS instruments in the National Institute of Standards and Technology (NIST) Center for Neutron Research. The wavelength (λ) of the incident neutrons was selected as 6.0 Å, with wavelength spreads, $\frac{\Delta\lambda}{\lambda}$, of 15%. The scattering wave vector, Q, ranges from (0.006 to 0.32) $Å^{-1}$. The samples were kept at a constant temperature of (23.0 ± 0.1) ^{o}C. For the present SANS-intensity distribution functions placed in an absolute scale, the corrections for detector background and sensitivity have been taken into account.

Figure 6-6 gives the evolution of true stress as a function of true strain for the alloys before and after the thermal treatment. The true stress-strain curves of the alloys are calculated from the engineering stress-strain curves to discriminate the interrelation between the gauge length and diameter change related to plastic deformation (Dieter 1986).

Due to the additional strengthening introduced by the presence of the nano-precipitates interacting with the dislocation activities, at the same strain level the mechanical property is seen to be enhanced markedly for the aged sample in comparison to the annealed one. For example, the 0.2% yield strength is seen to increase from 376 MPa to 690 MPa.

The corresponding SANS data for the alloys (blue symbols) along with their theoretical fits (red curves) incorporating a Q^{-4} contribution at small Q are shown in the top panel of Figure 6-7.

Unlike bottom two curves, a lack of the interaction peak centered at $Q \approx 0.03$ $Å^{-1}$ for the *I(Q)* obtained from the annealed sample prior to the aging processes is foremost noticed. Compared to the evolution of the mechanical properties presented in Figure 6-6, this observation clearly indicates that the establishment of the interaction peak is due to the precipitates developed during the thermal treatment. The bottom two curves, with the interaction peak at $Q \approx 0.03$ $Å^{-1}$, were measured from the aged alloy containing the nano precipitates. The coherent scattering intensity obtained from the aged alloys is presented in the bottom panel. When $Q > 0.03$ $Å^{-1}$, a clear difference is observed.

The quantitative structural information obtained from the SANS-model fitting is given in Table 6-1. It is noticed that, within the experimental error, the inter-precipitate distance, L, is seen to remain invariant before and after the deformation. The major structural change resulting from the applied stress is the morphological change of the precipitate. After the deformation, the long axis, R, of the ellipsoidal precipitate is found to increase from (58 to 64) Å, while the aspect ratio, ε, decreases from 0.67 to 0.58. As a result, the average shape of a single precipitate becomes more ellipsoidal.

The fact that the applied external stress shows little impact on the average volume of the precipitate (357 ± 35.7 and 370 ± 66.6) nm^3 deserves a special

attention. It has been well accepted, as proposed by Eshelby (1957), that the invariance of the volume of precipitates suggests no exchange of atoms between the precipitates and their embedded matrix during the deformation process.

One well-known characteristics of this diffussionless interface is the discrete change in the density when crossing from one phase to another. Based on this picture, it is conjectured that the change in the precipitate morphology is not from the grain growth but due to the spatial rearrangement of the intra-precipitate constituent elements. This hypothesis is not without any physical basis: The aforementioned invariance in L, as shown in Table 6-1, implies that there is no substantial creation or annihilation of precipitates during the deformation process to alter the average distance between the precipitates.

Moreover, during the deformation process, a discernable increase in σ, the variance of L, from (81 to 95) Å, is also noticed. This observation is believed to be the manifestation of the stress-enhanced shape anisotropy of precipitates, as indicated by the increase in the aspect ratio, ε.

As seen from Table 6-1, the results obtained from SANS-model fitting are quantitatively consistent with those computed from TEM image analysis. This agreement verifies the applicability of our proposed SANS methodology in exploring the structural properties of nano precipitates.

6.4. Summary

In conclusion, we present a SANS *I(Q)* model, combining the *P(Q)* for polydisperse ellipsoids and a stochastic phenomenological model of *S(Q)*, for studying the structural properties of a nickel-based alloy. Based on our model, a clear deviation in morphology of precipitates is found when a stress is applied. However, the average precipitate volume and inter-precipitate distance are seen to remain invariant, suggesting no significant diffusion involving during deformation process.

The validity of this proposed model is verified and backed by TEM experiments. The major contribution of this Chapter is that it provides an alternative route for exploring the microstructure of nano-precipitates embedded in a superalloy.

Moreover, in this Chapter, in-situ neutron-diffraction experiments were applied to characterize the strengthening mechanism from the nano particles of the age-hardening nickel-based superalloy. The irreversible of peak broadening of the nano particles was found. TEM results confirm that the peak broadening is in virtue of the dislocation-mediated activities with the nano particles.

The current observation shed light on the nano precipitates, plastically deformed with the surrounded matrix. The results suggest that the dislocation activities are the dominant mechanism on both nanocrystalline precipitates and the coarse-crystal matrix.

Chapter 7: Cyclic-deformation Mechanisms in Precipitated Nickel-based Superalloy

In this Chapter, we report the deformation mechanism of the aged alloy, with nano precipitates, subjected to cyclic loading. The fatigue-induced microstructure is characterized by novel polychromatic X-ray microdiffraction (PXM) together with in-situ neutron diffraction. In-situ neutron-diffraction measurements reveal two distinct stages of the fatigue damage, such as cyclic hardening and the following cyclic softening.

The similar residual-stress effect upon cyclic loading on temperature evolution of the aged alloy is observed, as detailed in Chapter 5 of the annealed alloy. With that, three-dimensional (3D) spatially-resolved PXM micro-Laue measurements are applied to demonstrate the development of the local texture and formation of geometrically necessary dislocations (GND) near the grain boundaries. The local GND is accompanied by lattice rotations and grain subdivisions. The PXM results are in agreement with the in-situ neutron-diffraction results.

7.1. Introduction

Superalloys are a group of nickel and cobalt-based materials that show exceptional strength for high-temperature applications. These materials are designed for the uses in the aircrafts, turbo blades, and many other high-temperature purposes (Erickson 1990). Typically, precipitate-strengthened nickel-based superalloys have

higher strengths than the cobalt-based superalloys (Sato e*t al.* 2006). The precipitate-strengthened nickel-based superalloys are widely used in the chemical and transportation industry, especially with the cyclic-loading environments, such as in the pistons, turbines, and engines. Metal fatigue is one of the most emergent damages because it promotes premature failure.

The research on the fatigue damage draws great attentions from both of the industry and the research communities because of its practical importance and complicated behavior (Agnew and Weertman 1997). An important step to understand the fatigue mechanism is to characterize how different microstructures respond to cyclic deformation. Recently, Gopinath *et al.* (2009) reported the low-cycle-fatigue behavior of a precipitation-strengthened nickel-based superalloy. Their transmission-electron microscopy (TEM) studies revealed that, besides the precipitate shearing, the dislocation activity of the matrix plays an important role for the fatigue damage. During fatigue of the polycrystalline materials, grains may deteriorate into practically regular deformation structures with different crystallographic orientations on a micrometer scale (Bay *et al.* 1992).

As mentioned in Mughrabi's latest review article (2009), "*…Today, it is clear that mechanisms of cyclic microplasticity, based on the glide of dislocations, are responsible for the fatigue phenomena.…*" In this study, we investigate the cyclic-loading-induced microplasticy in a nickel-based superalloy, resulting in the fatigue failure with the focus on the geometrically-necessary-dislocation (GND) accumulation near the deformation-induced grain boundary.

The current approach benefits from the latest development of the one-of-the-kind three-dimensional (3D) polychromatic X-ray microdiffraction (PXM). PXM has the unique possibility to obtain the spatially-resolved information. More specifically, the depth-resolved technique allows investigating the depth-dependent strain and dislocation gradients at the micro-scale. It is known that the spatially-resolved 3D X-ray investigations can explore the microstructural heterogeneity and the complicated hierarchical dislocation sub-structure in the depth of the materials (Barabash *et al.* 2001; 2009; Larson *et al.* 2002; 2008; Levine *et al.* 2006).

Besides the precise local strain and dislocation mapping with PXM at the microscale, the neutron-diffraction experiments were performed to obtain the ensemble-averaged structural information during fatigue experiments with a greater gauge volume at the macroscale (Huang *et al.* 2007; 2008). The in-situ neutron-diffraction measurements at the spallation neutron source make it possible to monitor the microstructural-parameter evolution of both the matrix and the precipitates. The in-situ neutron-diffraction experiments connect the bulk property and the lattice-strain evolution during cyclic loading.

The combination of these two novel techniques provides the unique information about the fatigue-induced microstructure evolution at the micro and macro scales.

7.2. Experimental Procedures

Material

An aged nickel-based superalloy (Ni-21Cr-17Mo in weight percentage) is used. The alloy contains about a 25% volume of the nano-precipitates. These $Ni_2(Cr,Mo)$-phase nano-precipitates are embedded in the faced-centered-cubic (f.c.c.) matrix. TEM (Lu *et al.* 2007) and small-angle neutron scattering (SANS) experiments (Huang *et al.* 2008) elucidate the size of the ellipsoidal precipitates to be about 10 nm in diameter.

Low-cycle-fatigue Experiments and In-situ Neutron-diffraction Measurements

The aged alloy is machined in a dog-bone shape for in-situ neutron-diffraction measurements as shown in Figure 7-1a. A gauge volume about 60 mm^3 from the center of the specimen was used through the low-cycle-fatigue experiments. The tests were carried out with the stress-rig at ENGIN-X, the ISIS spallation source in the Rutherford Appleton Laboratory, UK (Santisteban *et al.* 2006). Time-of-flight diffraction patterns were acquired with a count time of 40 minutes during straining for the statistically sufficient diffracted intensity to analyze the diffraction profile. Rietveld method was applied to fit the diffraction patterns.

The neutron-diffraction profiles were refined by the General Structure Analysis System (GSAS) at the macroscale (Von Dreele *et al.* 1982; Larson and Von Dreele 2004).

The low-cycle-fatigue (LCF) experiments were conducted under fully-reversed (R = -1) loading conditions with a strain range = ±1%. The frequency was 0.5 Hz. The neutron-diffraction data were collected at different cycles (N) during the fatigue experiments at N = 1, 5, 10, 25, 50, 100, 200, 500, 750, and 1,000. The specimen was loaded to a maximum engineering strain of 1%, and, then, measured for studying the cyclic effects as a function of fatigue cycles.

Synchrotron X-ray Microbeam Experiments

In this study, we employed a polychromatic 3D X-ray microdiffraction (PXM) with the energy range of 5 – 25 keV, developed by Oak Ridge National Laboratory (ORNL) at the Advanced Photo Source (APS) with the point-to-point submicron spatial resolution using the differential-aperture depth profiling and the depth-resolved analysis technique (Bei *et al.* 2008).

The primary advantage of PXM is the ability to determine crystalline structure without sample rotations. PXM using high-energy X-rays facilitates the investigation of the individual grains embedded in a polycrystal with a sub-micron spatial resolution under the surface of bulk samples. With the advantages of the PXM, the local phase of crystalline materials, the local orientation and, therefore, the grain and phase boundary structures, the local defect distributions, including elastic and plastic strains, were studied for the nickel-based superalloy after cyclic loading.

The PXM geometry and relative orientation of the sample to the beam are shown in Figure 7-1b. Two samples were prepared. Sample (I) was the reference

sample (before cyclic loading) and Sample (II) was after N=250, which was within the cyclic softening stage. The PXM results for the specimens before and after cyclic loading are shown in Figures 2a and b, respectively.

7.3. Results and Discussion

Bulk Property

The lifetime of the aged alloy was about 3,000 cycles. The difference of the peak stresses (squares) of the same fatigue cycle between + 1% and – 1% strains as a function of fatigue is shown in Figure 7-3. The cyclic hardening/softening behavior is noticed. The transition cycle was about the 25^{th}-fatigue cycle.

The temperature differences (circles) between these two strains (+/- 1% strains) of the aged alloy, recorded simultaneously, are in the bottom of Figure 7-3 for the comparison. The similar residual-stress effect (Wong *et al.* 1998; Quinn *et al.* 2004) on the temperature evolution is found as detailed in Chapter 5.

Volume-average Anisotropic-lattice Strains

A statistical understanding of the microstructure evolution during fatigue loading was advanced by *in-situ* neutron-diffraction experiments, which eliminate the possible differences due to sample preparations. The *in-situ* neutron-diffraction measurements during the experiments were performed to study the bulk-average-property and the lattice-stain evolution during fatigue-damage process. The macroscopic stresses at 1% strain are presented in Figure 7-3.

The neutron experiments conducted at + 1% strain of the fatigue cycles are present in terms of the lattice-strain development along crystallographic directions in the matrix-200 and nano-precipitates-*011* (Figures 7-4 and 5), respectively. The lattice parameter of the alloys before the cyclic loading determined from neutron diffraction is equal 0.3605 nm, which is further used for the PXM-diffraction-peak refinement.

The bulk-average stress evolution (Figure 7-3) shows that there are two stages along the cyclic loading in this study: cyclic hardening in the first 25 cycles and then cyclic softening. Via the neutron-diffraction-profile analysis at the macro-scale, the anisotropy of the non-monotonic lattice-strain evolution is revealed (Figures 7-4 and 5).

The lattice strains of the matrix grow along the crystallographic directions during the cyclic hardening up to the onset of cyclic softening typically occurs after N=30, after which a volume-average lattice strain in the matrix saturates and even slightly decreases. The features of the matrix-lattice strain are very similar to the lattice-strain evolution of the annealed alloy during the cyclic hardening and softening stages as detailed in Chapter 5.

The lattice-strain evolution of the {*200*} plane under + *1%*-tension (*Pt 7*) in both transverse and loading directions is presented in Figures 7-4a and b, respectively. In the early fatigue cycles, the lattice strain-and-stress relationships show an essentially linear behavior. The evolution of other f.c.c. peaks, such as the

[*111*] and [*311*] follow the similar linear relationship (Huang *et al*. 2009 unpublished).

The lattice-strain (ε^{nano}) evolution of the nano precipitates along the 011 direction shows a different feature. There is no linear lattice strain-stress relationship. On the other hand, a hysteresis loop is seen in both loading and transverse directions under tension at + 1% (Figures 7-5a and b).

The hysteretic lattice strain-stress relationship is also seen in Figures 7-5c and d when the compression stresses are applied. Although the nano precipitates have greater strength than the matrix, detailed in Chapter 6, the non-monotonic lattice-strain evolution of the nano precipitate indicates the strain inhomogeneity which comes from the fatigue damage upon cyclic loading. It is also evident in terms of the peak-width evolution as discussed below.

Nano-precipitate-peak-width Evolution

The peak-width of the nano precipitate is shown in Figure 7-6a. The intrinsic peak-broadening of the nano-size crystalline grains have several origins, such as the change of the particle size, dislocations, microstrain broadening, inhomogeneous of the lattice strains, and so on (Budrovic *et al.* 2004). Since, in my current study, there is no clear TEM picture to prove the dislocation yet, a reasonable straightforward contribution of the observed peak-width evolution (Figure 7-6b) could be the strain-inhomogeneity of the nano particles induced by the surrounded matrix. The inhomogeneity agrees with the lattice-strain evolution (Figures 7-5) discussed above.

Matrix-diffraction-peak-width Evolution

Upon fatigue damage, there are hard patterned-dislocation groupings and the soft interiors with the randomly-distributed dislocations (Mughrabi 1983). It is known that the randomly-distributed dislocations correspond to the Gaussian-broadening components in the reciprocal space (Zehetbauer, 1993; Hughes and Hansen, 1993; Krivoglaz, 1996; Barabash; 2001, and Schafler *et al*., 2005). Meanwhile, the patterned-dislocation structure with the planar-dislocation walls could be detected by the Lorentzian-broadening components.

To quantify the dislocation evolution, the formula detailed in Chapter 5 is applied based on Barabash's (2001, 2003) and Krivoglaz's methods (1996). More specifically, the dislocation calculations set forth in here are based on the peak-width change of the [*200*] peaks, which is known to be most sensitive to the plastic deformation (Hutchings *et al.* 2005). In Figure 7-6b, the dislocation density (n) and the distance between the patterned-dislocation planar-wall structures (D) are estimated at the maximum tension of + *1%* (*Pt 7*). Upon cyclic hardening, the dislocation density increases accordingly in both directions. The formation of the new patterned-dislocation-planar walls also decreases the averaged-distance (D) between them. After the 25^{th} cycle, the invariant of D indicates that the averaged size of the patterned-dislocation-planar-wall structure start to stabilize. However, the density of the randomly-distributed dislocations (n) keeps fluctuating during the fatigue cycles.

The question now becomes - how can we quantify the local spatially-varying microstructure after cyclic loading at the microscale? To understand the anisotropic

evolution of the inhomogeneous internal-strain fields and the detailed spatially-resolved microstructure, the materials are further explored via the PXM.

Inhomogeneous Distributions of Internal Strains and Geometrically-necessary Dislocations at the Micro Scale

Distinct inhomogeneous dislocation distributions are formed during (cyclic) plastic deformation (Poulsen *et al.* 2005). The PXM method is well suited for the analysis of such inhomogeneous deformation-induced structures at the microscale. Laue patterns from the perfect undeformed crystal contain sharp Laue spots. The formation of the statistically-stored dislocations (SSD), geometrically-necessary dislocation (GNDs), and geometrically-necessary boundaries (GNBs) causes both the local-strain fluctuations and strongly correlated long-range mesoscopic rotations within the grain or subgrain correspondingly (Barabash *et al.* 2003; Ice and Barabash 2007). Such correlated deformation spreads the conditions for X-ray scattering in the orientation space in the vicinity of each (*hkl*) lattice-plane normal and causes streaking of the Laue spot. When GNDs form, each (*hkl*) Laue spot is strongly elongated (streaked) in the certain direction, depending on the mutual orientation between the GNDs slip system and the direction of the incident beam. The details of the streaked Laue patterns analysis can be found elsewhere (Barabash *et al.* 2003; Ice and Barabash 2007). When the orientation of the lattice changes with depth, different layers incoherently scatter X-rays. Thus, the above described differential aperture X-ray microscopy (DAXM) is applied to find the depth-dependent orientation change.

The Laue patterns of the specimens before and after the cyclic loading are shown in Figures 7-3a and b, respectively. Before the cyclic loading, the relatively sharp and round diffraction spots corresponding to a perfect crystal are seen (Figure 7-3a). The elongated streaks in Figure 7-3b indicate the formation of GNDs dislocation populations after the cyclic loading (Bei *et al.* 2008).

The plastic responses of the material in the grain can be described by the formation of the patterned cell-block dislocation structure in the material to relax the stress field induced from the cyclic loadings. This is also observed by Gopinath *et al.* (2009). Their TEM results on the nickel-based precipitate-strengthened alloys, subjected to the cyclic loading, show that the grains have split into differently oriented fragments (sub-grains) due to subdivision (Liu *et al.* 1998).

To further study the different types of the microstructures, PXM was applied with the 3D depth-resolved DAXM technique to follow the accumulation of the lattice rotation, GNDs, GNBs, and grain subdivision as a function of the depth, the distances to the boundaries and to the fracture surface. The indexed Laue patterns were analyzed at different depths to investigate the locall texture and strain gradient distribution. This is discussed below.

Real-space Orientation Map and Pole Figures

Automated indexing is performed by carefully comparing the pattern of angular differences between reflections corresponding to different possible crystal orientations. Typically the groups of least 10 Laue spots with different (*hkl*s) are

compared until a match is found (Chung and Ice 1999). With an identified face-centered-cubic (f.c.c.) structure, the indexation process was converged (Figures 7-3b). A local crystallographic texture in the polycrystalline specimens was, then, determined, based on the local orientation. The lattice parameter used for indexation equal to 0.3605 nm was taken from the neutron-diffraction results. As a result of the indexation (Chung and Ice 1999), the real-space orientation map of the specimen is reconstructed over the larger area (Fig. 7-7). The reconstructed pole figure is shown in Figure 7-7a. The pole figure offers the information about the sample orientation distribution function with high resolution on local orientations. The locations of the (001), (100), and (010) poles are identified (Figure 7-7b).

The measured gradual orientation distributions around these three poles are zoomed in to further reveal the local-strain distribution at higher resolution (Figures 7-7c, d, and e). The orientation distributions around these three poles are practically orthogonal to each other. Orientation fluctuations around all three poles are within the range of 0.4 ~ 0.75 degrees.

The presence of the geometrically-necessary boundary (GNB) is indicated by the two groups of the diffractions with an abrupt orientation change (Figure 7-7a), indicating the existence of the GNB embedded beneath the sample surface.

Three-dimensional depth-resolved measurements were performed in locations that contained at least two grain subdivisions using a knife-edge type differential aperture. It is possible to reconstruct the in-depth scan and reveal the distribution of GNDs and GNBs within the grain subdivisions, as shown in Figures 7-7f. The

orientation differences at very large distances are shown in the reconstructed real-space maps (Figure 7-7f). Such orientation differences in different sub-grains could possibly result from the stress incompatibilities at the grain boundaries, caused by the grain-grain interactions under cyclic. The existence of these orientation differences over large distances is in agreement with the low-energy-dislocation-structure (LEDS) principle. Thus, the alternating point-to-point misorientations are impossible when simultaneously a gradient towards another orientation appears (Kulmann-Wilsdorf 1992).

Angle Rotation as a Function of Depth Revealing the GNBs

Using the high-spatial resolution of the PXM (~ 0.5 micrometer), the 1st and the 2nd subdivisions was investigated in detail as shown in Figure 7-8.

A schematic depth-resolved scan is shown in Figure 7-8a. The indexed Laue patterns corresponding to different depths under the sample surface are presented in Figures 7-8b, c, d. Near the surface, the lattice orientation (grain subdivision 1) is close to 333. At the depth of 10 micrometers, the diffraction from both subdivisions 1 and 2 are observed simultaneously (Figs. 7-8c and f). The second group of the diffraction spots corresponding to the deeper located lattice orientation is marked in purple. At the depth of 15 - 30 micrometers the group of the diffraction spots from the near-surface subdivision vanished. The diffraction spots resulting from the near-surface subgrain vanish between 15 - 30 micrometers below the surface.

An important result of the in-depth grain subdivision study with PXM is the detection of orientation distribution at and near the grain boundaries. The depth-dependent orientation distribution function (Figure 7-9) shows the in-depth lattice rotation.

The change of the lattice orientation as a function of the distance from the surface and from the near-surface boundary (highlighted by a blue arrow) demonstrates that the lattice-rotation changes gradually in the sub-grain near the surface (Subdivision 1). However, it practically does not change in the embedded sub-grain (Subdivision 2) beneath the surface. The inset pole figure depicts two groups of the indexed orientations from subdivisions 1 and 2, respectively. There is an abrupt rotation of $\approx 4^{o}$ between the subgrains. The results validate that the discontinuous angle distribution is the evidence of the boundary between two fatigue-induced grain-subdivisions.

The difference between the depth-dependent orientation distribution near the boundary observed in the above two subdivisions probably arises from the change in geometrical constraints and from their different orientations. The number of constraints increases as a function of the depth away from the surface. The observed in-depth gradient results in cumulative rotations and formation of GNDs, and occupies regions within the length-scale about 10 ~ 30 μm. The lattice rotation and grain subdivisions are also evident the cyclic-loading damage. They indicate the evolution of a hierarchical depth-dependent dislocation mesoscopic substructure,

evolving as a result of the translational-rotational movement of the grain with the free surface during the cyclic loadings due to both shear and rotation.

7.4. Summary

The in-situ neutron experiments show that the matrix-dislocation-density fluctuation changes the residual stress upon cyclic loading. The bulk thermo-mechanical observations agree with the neutron results. Hence, high-spatial resolution synchrotron X-ray microbeam experiments were applied to characterize the cyclic-loading-induced microstructure evolution of the matrix near the grain boundaries of the Ni-based polycrystalline superalloy. The spatially-resolved microstructure demonstrates the formation of the cumulative local texture induced by cyclic loading at the micro-scale. The cyclic-deformation-induced geometrical-necessary dislocations and boundaries were found. A distribution of geometrical-necessary dislocations is strongly influenced by the geometrical constraints from the surrounding grains and by the grain orientation. The PXM findings correlate with the neutron diffraction results.

Chapter 8: Fatigue-damage Transitions of the Annealed and the Aged Alloys

The purpose of this final Chapter is to revisit two key universal phenomena observed from both of the annealed and the aged alloys subjected to the cyclic loading, detailed in Chapters 5 and 7, respectively. The first phenomenon is the cyclic hardening-softening transition (Figure 8-1), and the second is the temperature differences between the tension-to-compression states (Figure 8-2). The results, presented in Chapters 5 and 7, are compared in this Chapter. There are two temperature-difference transitions. The 1st transition correlates to the cyclic hardening/softening. The discussion, in Chapters 5 and 7, suggests that the dislocation evolution is responsible for the cyclic hardening-softening phenomenon in the early fatigue-damage stage. The 2nd transition might indicate that the fatigue-induced microcracks start to play a more significant role during the higher fatigue cycles.

8.1. Introduction

It is clear that fatigue damage depends on many details of the microstructure. What atomic structures are basically responsible for fatigue damage? Mughrabi (2009) concludes that the dislocation activity is responsible for the degradation during the cyclic loading. On the other hand, Guinier (1989) addressed the importance of the microcracks for the fatigue damage. Although the formation of the microcracks might begin as early as the 5% of the fatigue life (Thompson 1959), so far, there is no direct

evidence of the microcracks because of the difficulty in preparing suitable samples (Guinier 1989).

8.2. Results and Discussion

To answer the challenge posed above, the temperature-evolution results are compared in order to add one more perspective to detect the fatigue-damage phenomena. Wong *et al.* (1988) had demonstrated the capability of monitoring temperature responses to examine the plastic deformation. Moreover, Quinn *et al.* (2004) concluded the thermo-mechanical relationship as described in Equation 8-1:

$$\Delta T = \frac{-\alpha T}{\rho C}\left(1 - \frac{1}{\alpha E^2}\frac{\partial E}{\partial T}\sigma_m\right)\Delta\sigma \,. \tag{8-1}$$

ΔT is the temperature response subjected to the mechanical deformation. α is the thermal expansion. C is the heat capacity. E is the Young's modulus. σ_m is the residual stress introduced by the plastic deformation. $\Delta\sigma$ is the stress change due to the elastic deformation, which can be referred in our study as the lattice-strain evolution (shown in Figures 5-6 and 7-4 for annealed and aged alloys, respectively). Based on the measured lattice strain, the thermo-mechanical responses can be estimated with the modified Stanley and Chen's equation (1985):

$$\Delta T = \frac{-\alpha E_{111} T}{\rho C(1-2\upsilon)}\left(\frac{\varepsilon_{111}^{loading} + \varepsilon_{111}^{transverse}}{2}\right) \times \frac{Volume\ of\ the\ Deformed\ Specimen}{Whole\text{-}specimen\ Volume} \tag{8-2}$$

E_{111} is the 111-lattice modulus, calculated in Chapter 3. $\nu = 0.31$ is the Poisson ratio of nickel. After cyclic loading, it is practical no texture development in our system as shown in Chapter 4. There is also no texture development subjected to tension-compression-fatigue experiments in other alloy systems, simulated by Turkmen *et al.* (2002). Hence, the lattice strains (ε_{111}) of grains in orthogonal directions (oriented to loading and transverse directions, respectively) are averaged. Thermal expansion ($\alpha = \frac{\gamma \rho C_V}{3E}$) is a function of Grüneisen parameter ($\gamma \equiv \frac{\partial(ln\,\omega_{Debye})}{\partial(ln\,V)}$), where ω_{Debye} is Debye frequency and V is the volume. Based on the generalized Hooke's law, discussed in Chapter 2, the temperature responses after the thermo-elastic relationship (Equation 8-2) are calculated with the updated volume strain, $\Delta V = (1+\varepsilon_{111})(1-\upsilon\varepsilon_{111})^2 - 1$, (Dieter 1986). The results are shown in Figure 8-2 for annealed (red line) and aged (blue line) alloys, respectively. Note that the linear lattice strain-stress relationships are seen in both the annealed (Figure 5-6) and the aged (Figure 7-4) alloys. Qualitative agreements between the measured and the calculated temperature evolution can be found as the 1st transition at the 25th and 100th fatigue cycles for the aged and annealed alloys, respectively. Since the dominant effect on the temperature evolution is the plastic deformation, the contributions from the dislocations and the microcracks are discussed below.

The 1st transition, shown in Figure 8-2, correlates to the cyclic hardening and softening [Figures 5-8(c) and Figure 7-6(b)]. The cause of the 1st-temperature

transition could relate to the dislocation developments and rearrangements, accordingly (detailed in Chapters 5 and 7). However, the amplitudes of the dislocation evolution during the 2nd-temperature transition can not reflect the levels of the temperature transitions during the greater fatigue cycles. In Equation 8-1, the residual stress could be the convolution of the dislocation and microcrack evolutions. The discrepancy between the dislocation-parameter and temperature-difference evolutions might indicate that the microcrack effect becomes more significant during the 2nd-temperature transition. If there are sufficient microcracks, the measured engineering stress might act on different local cross section, altered by these microcracks. A schematic understanding is shown in Figure 8-3. Figures 8-3(a) and (b) illustrate the deformation subjected to the tension and compression, respectively. The dominant deformation mechanism is the dislocation activities, as concluded by Mughrabi (2009). Upon the greater fatigue cycles, during the 2nd-temperature-transition cycles, the microcracks (Guinier 1989) make the local-stress distributions become inhomogeneous [Figures 8-3(c) and (d)].

To compare with the illustrations presented above, the P-ratio (Equation 5-9) evolution upon cyclic loading should be reminded. The P-ratio is calculated from two groups of the grains, oriented in orthogonal directions, subjected to loading modes [Figure 5-7(a)]. The P-ratio during the early fatigue cycles keeps the similar values of 0.31 ($=\nu_{nickkel}$). During the 2nd-temperature transition, the P-ratio increases to about 0.4 under the tension-loading mode. Meanwhile, the P-ratio decreases to about 0.2 under the compression-loading mode. This irreversible divergence of the P-ratio

indicates that there are more inhomogenous stress distributions in the fatigued-damaged alloys upon greater fatigue cycles. This could be the evidence of the local inhomogeneity introduced by microcracks. Moreover, the PXM results, discussed in Chapter 7, also confirm the formation of the local inhomogeneity in the fatigued specimen.

8.3. Summary

The results concluded in this Chapter indicate that the dislocation evolution is responsible for the cyclic hardening-softening phenomenon in the early fatigue-damage stage. The 2nd-temperature transition indicates that the fatigue-induced microcracks might be more significant during the higher fatigue cycles.

The P-ratio proposed in this dissertation can reveal the fatigue-damage stages because it is irreversible during the higher fatigue cycles. Quite the opposite, the other parameters, such as the macroscopic stress, temperature, thermal conductivity, and microscopic lattice strain and dislocation parameters, are reversible during the fatigue deformation.

Chapter 9: Conclusions

In this dissertation, the mechanical behavior of the nickel-based alloys is studied. The applications of the in-situ neutron-diffraction experiments reveal the lattice-strain and the dislocation-parameter evolution upon the deformation. The connections between the macroscopic-bulk-thermomechanical behavior and microscopic characteristics, obtained from the diffraction results, are concluded. Ex-situ small-angle neutron-scattering and electron microscopy results support the neutron diffraction results. Moreover, in addition to the cyclic hardening and softening, a 2^{nd}-temperature transition upon the greater fatigue cycles is found from both of the annealed and the aged alloys. This 2^{nd}-temperature transition is never reported before. The conclusions of the specific results are listed below.

1. The crystallographic-slip and the associated dislocation activities play the major role during the plastic deformation of the studied alloys, including the annealed and the aged specimens.
2. In-situ neutron-diffraction results, refined by GSAS with the pseudo-Voigt function, simultaneously distinguish the Gaussian and Lorentzian peak components for monitoring the density of dislocations and the average distance between patterned-dislocation structures, respectively.
3. For the monotonic-tensile experiments on the annealed alloy, there was practically no accumulation of the dislocations in the elastic region (Stage I). Within 370 ~ 750 MPa, the dislocation hardening was the major strengthening

mechanism. Above 750 MPa, the patterned-dislocation spacing evolved differently with dislocation density because the mechanical properties of dislocations within the walls are stiffer than those inside the cells, as described by Mughrabi's composite model.

4. The same analysis method on the identical setup of the in-situ neutron-diffraction experiments is applied to study the cyclically-deformed alloys. For the same level of the applied stress, there are less dislocation density and greater patterned-dislocation spacing of the cyclically-deformed sample than that of the monotonically-deformed specimen.
5. The microscopic ensemble-averaged neutron results and the bulk-property evolution upon cyclic loading show the non-monotonic development of the fatigue-induced dislocation sub-structures.
6. The evolution of the dislocation structure and lattice strain reflects three distinct stages in the fatigue-damage development as cyclic hardening, softening, and saturation.
7. The bulk cyclic hardening is the consequence of the increase of the dislocation density and the formation of the patterned-dislocation structures. The lattice-spacing development during fatigue is accompanied by the thermoelastic effect on the heat absorption and generation.
8. The anisotropy between the loading and the transverse direction and the dislocation-structure parameters demonstrate the irreversible fatigue-deformation activities. The tension-to-compression asymmetry of the lattice-

strain and dislocation-substructure-parameter evolution in the stage 3 ($1,000^{th}$ ~ $2,500^{th}$ fatigue cycles) reveals a significant Bauschinger effect.

9. The lattice-strain evolution together with the change of the dislocation parameters and temperature dependence suggest that the second-order-type structural transformation occurs in the dislocation sub-structure during the stage 3 (the saturation cycles within the $1,000^{th}$ ~ $2,500^{th}$). The non-monotonic behavior during the saturation cycles shows the residual-stress-evolution effect upon the dislocation-density fluctuations.
10. The tension deformation on the aged alloys, strengthened by the nano precipitates, is studied via in-situ neutron diffraction experiments.
11. Upon the greater stresses, both the matrix and the nano particles are plastically deformed. The irreversible of neutron-diffraction-peak broadening of both the matrix and the nano particles was found.
12. The onset of the peak-profile broadening shows the nano precipitates plastically deform at the higher stress level than that of the matrix. The results suggest the particle-shearing is the hardening mechanism of the studied aged alloy.
13. Small-angle neutron scattering (SANS) was used to quantify the deformation of the nano precipitates of the alloy. A theoretical model for the SANS intensity distribution was developed to provide the quantitative structure information, such as the morphology of the precipitates and the average

distance between the precipitates. The plastically-deformed nano particles show the change of the shapes, but invariance of the size.

14. The fatigue behavior of the aged alloy is studied via in-situ neutron-diffraction experiments. The bulk cyclic-hardening and softening stages of the aged alloy correlate with the dislocation-parameter and lattice-strain evolution of the matrix.
15. The creation of the randomly-distributed dislocation and the formation of the patterned-dislocation structure are observed via in-situ neutron-diffraction experiments.
16. The bulk cyclic-hardening-and-softening evolution agrees with the matrix-dislocation fluctuations. The evolution of the microstructure changes the residual stress as a function of the fatigue cycle. Hence, similar to the annealed alloy, the thermo-mechanical evolution shows the corresponding non-monotonic transitions.
17. Upon cyclic loading, the non-monotonic nano-particle-diffraction evolution of the aged alloy shows the inhomogeneity of the nano particles. The results suggest the fatigue damages of the nano particles.
18. High-spatial resolution synchrotron X-ray microbeam experiments were applied to characterize the cyclic-loading-induced microstructure evolution of the matrix near the grain boundaries.
19. The spatially-resolved microstructure demonstrates the formation of the cumulative local texture induced by cyclic loading at the micro-scale.

20. The cyclic-deformation-induced geometrical-necessary dislocations and boundaries were found. A distribution of geometrical-necessary dislocations is strongly influenced by the geometrical constraints from the surrounding grains and by the grain orientation. The PXM findings correlate with the neutron diffraction results.

Chapter 10: Future Work

The texture measurements should be applied for the complete pole figures. The information can update the contrast factors according to tensile and compressive deformation to improve the present dislocation calculations. The High-Pressure Preferred Orientation Diffractometer at the Los Alamos National Laboratory would be a good choice for the complete-pole-figure measurements.

The local deformation should be extensively investigated to identify different types of deformation-dependent strain distributions. Both high-resolution transmission-electron and synchrotron X-ray microbeam will be good selections for the detailed-local-morphology examination.

A more sensitive temperature measurement with high spatial resolution should be coupled with the mechanical tests to verify/refine the characterization presented in Chapters 5, 7, and 8. The infrared camera would be a good approach to further characterize the temperature evolution of the alloys subjected to the deformation.

The modeling efforts of the small-angle-neutron-scattering-data analysis presented in Chapter 6 should be improved in order to consider the morphology of the interfaces between different phases subjected to the deformation.

All the presented experiments should be revisited in the high-temperature environment because the nickel-based superalloys are designed for the applications at elevated temperatures. The current room-temperature results can be used as reference.

The tension-tension fatigue experiments should be studied because the industrial components, such as the hoists, cranes, and clamps, are used under a tension-tension-loading mode.

The aging parameters of the precipitation should be investigated to understand the precipitation kinetics. The fist step can be the study of the aging-time effect. The kinetics of the precipitation can be explored with the reported research methods, such as SANS, in this dissertation.

The fracture-mechanism research should be conducted to advance the current understanding of the deformation mechanisms of the alloys.

List of References

Abdu-Latif, A. and Saanouni, K., 1996. Micromechanical modeling of low cycle fatigue under complex loadings 2. applications. *International Journal of Plasticity*, **12**, 1123-1149.

Agnew, S. R. and Weertman, J. R., 1998. Cyclic softening of ultrafine copper. *Materials Science and Engineering A*, **244**, 145-153.

Allen, S. M. and Thomas, E. L., 1999. *The Structure of Materials*. John Wiley & Sons, Inc.

Ardell, A. J., 1985. Precipitation hardening. *Metallurgical Transactions A*, **16**, 2131-2165.

Arya, A., Dey, G. K., Vasudevan, V. K., and Banerjee, S., 2002. Effect of chromium addition on the ordering behavior of Ni-Mo alloy: experimental results vs. electronic structure calculations, *Acta Materialia*, **50**, 3301-3315.

Ashby, M. F., 1972. A first report on deformation-mechanism maps. *Acta Metallurgica*, **20**, 887-897.

Ashby, M. F., 1989. On the engineering properties of materials. *Acta Metallurgica,* **37**, 1273-1293.

ASM Metal Handbook, 1973. 8th edition. Am. Soc. Metals, Columbus, Ohio.

Baczmanski A. and Braham C., 2004, Elastoplastic properties of duplex steel determined using neutron diffraction and self-consistent model, *Acta Materialia,* **52**, 1133-1142.

Balzar D. and Ledbetter, H., 1993. Voigt-function modeling in fourier-analysis of size-broadened and strain-broadened x-ray-diffraction peaks. *Journal of Applied Crystalline,* **26**, 97-103.

Balzar, D., Audebrand, N., Daymond, M. R., Fitch, A., Hewat, A., Langford, J. I., Le Bail, A., Louer, D., Masson, O., McCowan, C. N., Popa, N. C., Stephens, P. W. and Toby, B. H., 2004, Size-strain line-broadening analysis of the ceria round-robin sample. *Journal of Applied Crystallography*, **37**, 911-924.

Barabash R. I. and Krivoglaz, M. A., 1982. On the theory of x-ray and thermal-neutron scattering in strongly distorted crystals containing dislocation loops, *Physics of Metals*, **4**, 417-428.

Barabash R. I. and Klimanek, P., 1999. X-ray scattering by crystals with local lattice rotation fields, *Journal of Applied Crystallography,* **32**, 1050-1059.

Barabash, R. I., 2001, X-ray and neutron scattering by different dislocation ensembles. *Material Science Engineering A,* **309-310**, 49-54.

Barabash, R. I., Ice, G. E., Walker, F., 2003. Quantitative microdiffraction from deformed crystals with unpaired dislocations and dislocation walls. *Journal of Applied Physics*, **93,** 1457-1464.

Bay, B., Hansen, N., Hughes, D. A., Kuhlmann-Wilsdorf, D. A. D., 1992, Overview no. 96: evolution of fcc deformation structures in polyslip. *Acta Metallurgica et Materialia,* **40**, 205.

Bei, H., Barabash**,** R. I., Ice, G. E., Liu, W., Tischler, J., and George, E. P., 2008. Partially resolved strain measurements in Mo-alloy micropillars by differential aperture x-ray microscopy, *Applied Physics Letters*, **93**, 071904.

Benson, M. L., Liaw, P. K., Saleh, T. A., Choo, H., Brown, D. W., Daymond, M. R., Huang, E-W., Wang, X.-L., Stoica, A. D., Buchanan, R. A., and Klarstrom, D. L., 2006, Deformation-induced phase development in a cobalt-based superalloy during monotonic and cyclic deformation, *Physica B*, **385-386**, 523-525.

Bernier, J. V. and Miller, M. P., 2006. A direct method for determination of the mean orientation-dependent elastic strains and stresses in polycrystalline materials from strain pole figure, *Journal of Applied Crystallography*, **39**, 358-368.

Bian, L., Taheri, F., and Lu, Y., 2008. Analytical and experimental evolutions of the influence of fracture surface roughness, its sliding actions and the associated plasticity on fatigue crack propagation. *International Journal of Plasticity*, **24**, 302-326.

Biermann, H., Ungar, T., Pfannenmuller, T., Hoffmann, G., Borbely, A., and Mughrabi, H., 1993. Local variations of lattice parameter and long-range internal stresses during cyclic deformation of polycrystalline copper. *Acta Metallurgica et Materialia*, **41,** 2743-2753.

Borbely, A., Driver, J. H., and Ungar, T., 2000. An X-ray method for the determination of stored energies in texture components of deformed metals; Application to cold worked ultra high purity iron, *Acta Mater*ialia, **48**, 2005-2016.

Bourke, M. A. M., Dunand, D. C., and Ustundag, E., 2002. SMARTS- a spectrometer for strain measurement in engineering materials. *Applied Physics A,* **74**, 1707-1709.

Bridier, F., McDowell, D. L., Villechaise, P., and Mendez, J., 2009. Crystal plasticity modeling of slip activity in Ti-6Al-4V under high cycle fatigue loading. *International Journal of Plasticity,* **25**, 1066-1082.

Brown, D. W., Bourke, M. A. M., Clausen, B., Holden, T. M., Tome, C. N., and Varma, R., 2003. A neutron diffraction and modeling study of uniaxial deformation in polycrystalline Beryllium. *Metallurgical and Materials Transaction A,* **34**, 1439-1449.

Brown, L. M., 2000. Dislocation plasticity in persistent slip bands. *Material Science Engineering A*, **285**, 35-42.

Brown, L. M., 2004. A discussion of the structure and behavior of dipole walls in cyclic plasticity. *Philosophical Magazine*, **84**, 2501-2520.

Brown, L. M., 2006. Dislocation bowing and passing in persistent slip bands. *Philosophical Magazine,* **86**, 4055-4068.

Budrovic, Z., Van Swygenhoven, H., Derlet, P. M., Petegem, S. V., and Schmitt, B., 2004. Plastic deformation with reversible peak broadening in nanocrystalline nickel. *Science*, **304**, 273-276.

Cantrell, J. H., 2006. Quantitative assessment of fatigue damages accumulation in wavy slip metals from acoustic harmonic generation. *Philosophical Magazine*, **86**, 1539-1554.

Chen, L. J., Liaw, P. K., Wang, H., He, Y. H., McDaniels, R. L., Jiang, L., Yang, B., ad Klarstrom, D. L. (2004). Cyclic deformation behavior of HAYNES HR-120 superalloy under low-cycle fatigue loading. *Mechanics of Materials,* **36**, 85-98.

Chung, J. S. and Ice, G. E., 1999. Automated indexing for texture and strain measurement with broad-band pass x-ray microbeams. *Journal of Applied Physics*, **86**, 5249-5255.

Clausen, B., Lorentzen, T., Bourke, M. A. M., and Daymond, M. R., 1999. Lattice strain evolution during uniaxial tensile loading of stainless steel, *Materials Science and Engineering A,* **259**, 17-24.

Clausen, B., Lorentzen, T., and Leffers, T., 1998. Self-consistent modeling of the plastic deformation of FCC polycrystal and its implications for diffraction measurements of internal stresses, *Acta Materialia*, **46**, 3087-3098.

Davidson, D. L. and Lankford, J. 1992. Fatigue crack growth in metals and alloys: mechanisms and micromechanics. *International Materials Reviews,* **37**, 45-76.

Daymond, M. R., Bourke, M. A. M., Von Dreele, R. B., Clausen, B., and Lorentzen, T., 1997. Use Rietveld refinement for elastic macrostrain determination and for evaluation of plastic strain history from diffraction spectra. *Journal of Applied Physics*, **82**, 1554-1562.

Daymond, M. R., Tome, C. N., and Bourke, M. A. M., 2000. Measured and predicted intergranular strains in textured austenitic steel, *Acta Materialia*. **48**, 553-564.

Daymond, M. R., Preuss, M. and Clausen, B., 2007. Evidence of variation in slip mode in a polycrystalline nickel-base superalloy with change in temperature from neutron diffraction strain measurements, *Acta Materialia,* **55**, 3089-3012.

Dieter G. E., 1986. *Mechanical Metallurgy*, 3rd edition, McGraw-Hill, New York.

Dingli, J. P., Abdul-Latif, A., and Saanouni, K., 2000. Predictions of the complex cyclic behavior of polycrystal using a self-consistent modeling. *International Journal of Plasticity,* **16**, 411-437.

Doherty, R. D., Hughes, D. A., Humphreys, F. J., Jonas, J. J., Juul Jenson, D., Kassner, King, W. E., McNelley, T. R., McQueen, H. J., Rollett, A. D., 1997. Current issues in recrystallization: a review. *Materials Science and Engineering A*, **238**, 219-274.

Egami, T. and Billinge, S. J. L., 2003. *Underneath the Bragg peaks structural analysis of complex materials.* Pergamon Materials Series. Elsevier Ltd.

Eshelby, J. D., 1957. The determination of the elastic field of an ellipsoidal inclusion and related problems. *Proceedings of the Royal Society A,* **241**, 376-396.

Erickson, G. L., 1990. Polycrystalline cast superalloys. *ASM Handbook*, 10th edition, **1**, 981-990.

Essmann, U. and Mughrabi, H., 1979. Annihilation of dislocations during tensile and cyclic deformation and limits of dislocation densities. *Philosophical Magazine A*, **40**, 731-756.

Essmann, U., Gosele, U., and Mughrabi, H., 1981. A model of extrusions and intrusions in fatigues metals 1. point-defect production and the growth of extrusions. *Philosophical Magazine A*, **44**, 405-426.

Fleischer, R. L., 1987. Number of active slip systems in polycrystalline brass-implications for ductility in other structures, *Acta Metallurgica*, **35**, 2129-2136.

Gell, M. and Duhl, D. N., 1986. *Advanced High-temperature Alloys*, ASM International, Materials Park, OH.

Giordano, R., Grasso, A., and Teixeira, J., 1991. Small-angle neutron-scattering in lysozyme solutions, *Physical Review A,* **43**, 6894-6899.

Girifalco, L. A., 2000. *Statistical Mechanics of Solids*, Oxford University Press.

Gleiter H. and Hornbogen, E., 1967. Formation of coherent ordered precipitates in Ni-Cr-Al-alloy, *Zeitschrift fur Metallkunde*, **58**, 157-158.

Gopinath, K., Gogia, A. K., Kamat, S. V., Balamuralikrishnan, R., and Ramamurty, U., 2009. Low cycle fatigue behavior of a low interstitial ni-base superalloy. *Acta Materialia*, **57**, 3450-3459.

Groma, I., 1998. X-ray line broadening due to an inhomogeneous dislocation distribution, *Physical Review B*, **57**, 7535-7542.

Guinier, A. and Julien, R., 1989. *The Solid State from Superconductors to Superalloys*, Oxford Science Publications.

Haasen, P., 1996. *Physical Metallurgy*, 3rd edition, Cambridge University Press.

Hansen, N. and Hughes, D. A., 1995. Analysis of large dislocation populations in deformed metals, *Physics Status Solid B*, **149**, 155-172.

Hansen, N., 2001. New discoveries in deformed metals. *Metallurgical and Materials Transactions A,* **32**, 2917-2935.

Hansen, N., 2005. Boundary strengthening over five length scales. *Advanced Engineering Materials*, **7**, 815-821.

HASTELLOY® C-22HS™ alloy Manual, 2005. (http://www.haynesintl.com/pdf/h2122.pdf).

Heidelbach, F., 2001. Materials science – watching grains deform, *Science*, **291**, 2330-2331.

Hertzberg, R. W., 1983. *Deformation and Fracture Mechanics of Engineering Materials*, **2**nd edition, John Wiley & Sons, Inc.

Hill, R. 1965. A self-consistent mechanics of composite materials, *Journal of the Mechanics and Physics of Solids*, **13**, 213-222.

Hirsch, P. B., and Whelan, M. J., 1960. A kinematical theory of diffraction contrast of electron transmission microscope images of dislocations and other defects. *Philosophical Transactions of the Royal Society of London A*, **252**, 499-529.

Holden, T., Tome, C. N., and Holt, R. A., 1998. Experimental and theoretical studies of the superposition of intergranular and macroscopic strains in Ni-based industrial alloys. *Metallurgical Transaction A*, **29**, 2967-2973.

Hollingsworth, M. D., 2002. Crystal engineering: from structure to function, *Science*, **295**, 2410-2413.

Höppel, H. W., Zhou, Z. M., Mughrabi, H. Valiev, R. Z., 2002, Microstructural study of the parameters governing coarsening and cyclic softening in fatigues ultrafine-grained copper, *Philosophical Magazine A*, **82**, 1781-1794.

Hornbogen, E., 2001. Precipitation hardening-the oldest nanotechnology. *Metals,* **55**, 522-526.

Howie, A. and Whelan, M. J., 1962. Diffraction contrast of electron microscope images of crystal lattice defects. III. Results and experimental confirmation of the dynamical theory of dislocation image contrast. *Proceedings of the Royal Society London A*, **267**, 206-230.

Huang, E-W., Clausen, B., Wang, Y.D., Choo, H., Liaw, P. K., Benson, M. L., Pike, L. M., and Klarstrom, D. L., 2007. A neutron-diffraction study of the low-cycle fatigue behavior of Hastelloy C-22HS™ alloy. *International J. of Fatigue.* **29**, 1812-1819.

Huang, E-W., Wang, Y. D., Clausen, B., Benson, M. L., Liaw, P. K., Choo, H., and Pike, L. M., 2007. A non-destructive hkl-planes analysis of Haynes® C-22HS™ alloy study, *Key Engineering Materials*, **345-346**, 1311-1314.

Huang, E-W., Barabash, R. I., Wang, Y. D., Clausen, B., Li, L., Liaw, P. K., Ice, G. E., Ren, Y., Choo, H., Pike, L. M., and Klarstrom, D. L., 2008. Plasticity behavior of a nickel-based alloy under monotonic-tension and low-cycle-fatigue loading. *International Journal of Plasticity*, **24**, 1440-1456.

Huang, E-W., Barabash, R., Jia, N., Wang, Y. D., Ice, G. E., Clausen, B., Horton, J., and Liaw P. K., 2008. Slip-system-related dislocation study from in-situ neutron measurements. *Metallurgical and Materials Transactions A*, **39**, 3079-3088.

Huang, E-W., Liaw, P. K., Porcar, L., Liu, Y., Kai, J.-J., Liu, Y.-L., and Chen, W.-R., 2008. Study of nano-precipitates in a nickel-based superalloy using small-angle neutron scattering and transmission electron microscopy, *Applied Physics Letter*, **93**, 161904.

Huang, E-W., Barabash, R. I., Clausen, B., Kai, J.-J., Liu, Y.-L., Liaw, P. K., Ice, G. E., 2009. Fatigue-induced reversible/irreversible structural-transformation study of a nickel-based alloy using in-situ neutron-diffraction and thermal characterization. *International Journal of Plasticity*, (submitted).

Huang, E-W., Barabash, R. I., Liu, W., Kai, J.-J., Liu, Y.-L., Liaw, P. K., Ice, G. E., 2009. Cyclic-loading-induced accumulation of geometrically necessary dislocations near grain boundaries in a ni-based superalloy. *JOM*, (submitted).

Huang, E-W., Liu, F. X., and Liaw, P. K. (unpublished). Using IR-camera to study the deformation of HASTELLOY.

Huang, M., Rivera-Diaz-del-Castillo, P. E. J., Bouaziz, O., Van der Zwaag, S., 2009. Modeling the steady state deformation stress under various deformations using a single reversible thermodynamics based formulation. *Acta Materialia,* **57,** 3431-3438.

Hughes, D. A. and Hansen, N., 1993. Microstructural evolution in nickel during rolling from intermediate to large strains. *Metallurgical Transaction.* **24A**, 2021-2037.

Humphreys, F. J., 2001. Review: Grain and subgrain characterization by electron backscatter diffraction. *Journal of Materials Science*, **36**, 3833-3854.

Humphreys, F. J. and Hatherly M., 2004. *Recrystallization and Related Annealing Phenomena*, 2nd edition. Elsevier.

Hutchings, M. T., Withers, P. J., Holden, T. M., and Lorentzen, T., 2005. *Introduction to the characterization of residual stress by neutron diffraction*. Taylor and Francis Group.

Hutchinson, J. W., 1970. Elastic-plastic behaviour of polycrystalline metals and composites. *Proceedings of Royal Society London A*, **319**, 247-272.

Hutchinson, J. W., 1976. Bounds and self-consistent estimates for creep of polycrystalline materials, *Proceedings of Royal Society London A*, **348**, 101-127.

Ice, G.E. and Barabash, R.I., 2007. White Beam Micro Diffraction and Dislocations Gradients, in series: *Dislocations in Solids*, **13**, 500-601.

Jakobsen, B., Lienert, U., Almer, J., Shastri, S. D., Sorensen, H. O., Gundlach, C., and Pantleon, W., 2006. Formation and subdivision of deformation structures during plastic deformation. *Science,* **312**, 889-892.

Jia, N., Peng Lin, R., Wang, Y. D., Johansson, S., and Liaw, P. K., 2008 Micromechanical behavior and texture evolution of duplex stainless steel studied by neutron diffraction and self-consistent modeling. *Acta Materialia*, **56**, 782-793.

Jiang, J. Z., Kato, H., Ohsuna, T., Saisa, J., Inoue, A., Saksl, K., Franz, H., Stahl, K., 2003. Origin of nondetectable x-ray diffraction peaks in nanocomposite CuTiZr alloys. *Applied Physics Letters,* **83**, 3299-3301.

Jiang, L., Wang, H., Liaw, P. K., Brooks, C. R., and Klarstrom D. L., 2004. Temperature evolution during low-cycle fatigue of ULTIMET alloy: experiment and modeling. *Mechanics of Materials,* **36**, 73-84.

Jiang, Y., Feng, M. and Ding, F., 2005. A reexamination of plasticity-induced crack closure in fatigue crack propagation. *International Journal of Plasticity*, **21**, 1720-1740.

Kang, G. Z., Liu, Y. J., Ding, J., and Gao, Q., 2009. Uniaxial ratcheting and fatigue failure of tempered 42CrMo steel: Damage evolution and damage-coupled visco-plastic constitutive model. *International J. Plasticity*, **25**, 838-860.

Kaplan, H. I. and Laird, C., 1967. On the mechanism of stage I crack propagation in fatigue. *Transactions of the Metallurgical Society of AIME*, **239**, 1017-1025.

Kim, W. H. and Laird, C., 1978. Crack nucleation and stage I propagation in high strain fatigue – II. mechanism. *Acta Metallurgica*, **26**, 789-799.

Kocks, U. F., Tome, C. N., and Wenk, H.-R., 1998. *Texture and Anisotropy: Preferred Orientation in Polycrystals and Their Effects on Materials Properties*, Cambridge University Press.

Krivoglaz, M. A., 1969. *Theory of X-Ray and Thermal Neutron Scattering by Real Crystals*, **1**st edition, Plenum.

Krivoglaz, M. A., Ryaboshapka, K. P., and Barabash, R. I., 1970. Theory of x-ray scattering by crystal containing dislocation walls, *Physics of Meals and Metallography,* **30**, 1134-1140.

Krivoglaz, M. A., 1996. *X-Ray and Neutron Diffraction in Nonideal Crystal*, **1**st edition, Springer.

Kuhlmann-Wilsdorf, D., 1962. A new theory of work hardening. *Transactions of Metallurgical Society of AIME*, **224**, 1047-1062.

Kuhlmann-Wilsdorf, D. and Laird, C., 1977. Dislocation behavior in fatigue. *Materials Science and Engineering A*, **27**, 137-156.

Kuhlmann-Wilsdorf, D., 1999. The theory of dislocation-based crystal plasticity. *Philosophical Magazine A*, **79**, 955-1008.

Kumar, A., Jayakumar, T., Raj, B., and Ray, K. K., 2003. Correlation between ultrasonic shear wave velocity and Poisson's ratio for isotropic materials. *Acta Materialia*, **51**, 2417-2426.

Laird, C., Charsley, P. and Mughrabi, H., 1986. Low-energy dislocation-structure produced by cyclic deformation. *Materials Science Engineering,* **81**, 433-450.

Laird, C. and Smith, G. C., 1962. Crack propagation in high stress fatigue. *Philosophical Magazine,* **7**, 847-857.

Lakes, R. S., Lee, T., Bersie, A., and Wang, Y. C., 2001. Extreme damping in composite materials with negative-stiffness inclusions. *Nature*, **410**, 565-567.

Larson, A. C. and Von Dreele, R. B., 2004. General structure analysis system. *Los Alamos National Laboratory Report LAUR*, 86-748, 160-165.

Larson, B. C., Yang, W., Ice, G. E., Budai, J. D., and Tischler, J. Z., 2002. Three-dimensional x-ray structural microscopy with submicrometre resolution. *Nature*, **415**, 887-890.

Larson, B. C., Tischler, J. Z., El-Azab, A., Liu, W., 2008. Dislocation density tensor characterization of deformation using 3D x-ray microscopy. *Journal of Engineering Materials and Technology*. **130**, 0210241.

Lebensohn, R. A. and Tome, C. N., 1993. A self-consistent anisotropic approach for the simulation of plastic-deformation and texture development of polycrystals-application to zirconium alloys, *Acta Metallurgica Materialia,* **41**, 2611-2624.

Levine, L.E., Larson, B.C., Yang, W., Kassner, M.E., Tischler, J.Z., Delos-Reyes, M.A., Fields, R.J., Liu, W. 2006, X-ray microdiffraction measurements of individual dislocation cell elastic strains in deformed single-crystal copper, *Nature Materials*, **5,** 619-622

Lindner, P. And Zemb, Th., 2002. *Neutron, X-rays and light: scattering methods applied to soft condensed matter*, 1st edition, North-Holland.

Liu, Q., Jensen, D. J., and Hansen N., 1998. Effect of grain orientation on deformation structure in cold-rolled polycrystalline aluminum, *Acta Materialia*, **46**, 5819-5838.

Lorentzen, T., Daymond, M. R., Clausen, B., and Tome, C. N., 2002. Lattice strain evolution during cyclic loading of stainless steel. *Acta Materialia,* **50,** 1627-1638.

Lu, Y. L., Pike, L. M., Brooks, C. R., Liaw, P. K., and Klarstrom, D. L., 2007. Strengthening domains in a Ni-21Cr-17Mo alloy. *Scripta Materialia,* **56**, 121-124.

Liu, Q., Jensen, D. J., and Hansen, N., 1998. Effect of grain orientation on deformation structure in cold-rolled polycrystalline aluminium, *Acta Materialia*, **46**, 5819-5838.

Margulies, L., Winther, G., and Poulsen H. F., 2001. In situ measurement of grain rotation during deformation of polycrystals. *Science*, **291**, 2392-2394.

Miller, M. P., Bernier, J. V., Park, J.-S., and Kazimirov, 2005, Experimental measurement of lattice strain pole figures using synchrotron x rays. *Review of Scientific Instruments*, **76**, 113903.

Mott, N. F., 1958. A theory of the origin of fatigue cracks. *Acta Metallurgica*, **6**, 195-197.

Mughrabi, H., 1983. Dislocation wall and cell structures and long-range internal stresses in deformed metal crystals. *Acta Metallurgica*, **31**, 1367-1379.

Mughrabi, H., 2000, On the grain-size dependent of metal fatigue: outlook on the fatigue of ultrafine-grained metals. *Investigations and Applications of Severe Plastic Deformation*, Lowe, T. C. and Valiev, R. Z., eds., Kluwer Academic Publishers, Netherlands, 241-251.

Mughrabi, H. and Pschenitzka, F., 2005. Constructed glide and interaction of bowed-out screw dislocations in confined channels. *Philosophical Magazine,* **85,** 3029-3045.

Mughrabi, H., 2009. Cyclic slip irreversibilities and the evolution of fatigue damage. *Metallurgical and Materials Transaction A*, **40**, 1257-1279.

Neumann, P., 1974. New experiments concerning the slip processes at propagating fatigue crack – I. *Acta Metallurgica*, **22**, 1155-1165.

Nix, W. D., Gibeling, J. C., and Hughes, D. A., 1985. Time-dependent deformation of metals. *Metallurgical Transaction A*, **16**, 2215-2226.

Olson, G. B., 1997. Computational design of hierarchically structured materials. *Science*, **277**, 1237-1242.

Pang, J. W. L., Holden, T. M., Wright, J. S., and Mason, T. E., 2000. The generation of intergranular strains in 309H stainless steel under uniaxial loading, *Acta Materialia,* **48**, 1131-1140.

Philips, B. R. 2001, *Crystals, Defects and Microstructures Modeling Across Scales*, Cambridge University Press.

Poulsen, H. F., Lienert, U., and Pantleon, W., 2005. Characterization of orientation distributions of individual grains within deformed metals. *Materials Science Technology*, **21**, 1397-1400.

Quinn, S., Dulieu-Barton, J. M., and Langlands, J. M., 2004. Progress in thermoelastic residual stress measurement. *Strain*, **40**, 127-133.

Read, W. T. and Shockley, W., 1950. Dislocation models of crystal grain boundaries, *Physical Review*, **78**, 275-289.

Rietveld, H. M., 1967. Line profiles of neutron powder-diffraction peaks for structure refinement, *Acta Crystalline*, **22**, 151.

Rittel, D., Wang, Z. G. and Merzer, M., 2006. Adiabatic shear failure and dynamic stored energy of cold work. *Physical Review Letter,* **96**, 07552.

Santisteban, J. R. Daymond, M. R., Edwards, L., James, J. A. J., 2006, ENGINX: A third generation neutron strain, *Journal of Applied Crystalline*, **39**, 812–825.

Sato, J., Omori, T., Oikawa, Ohnuma, I., Kainuma, R., and Ishida, K. 2006. Cobalt-base high-temperature alloys. *Science*, **312**, 90-91.

Schafler, E., Simon, K., Bernstorf, S., Hanak, P., Tichy, G., Ungar, T., and Zehetbauer, M. J., 2005. A second-order phase transformation of the dislocation structure during plastic deformation determined by in situ synchrotron X-ray diffraction. *Acta Materialia,* **53**, 315-322.

Segall, R. L., Partridge, P. G., and Hirsch, P. B., 1961. The dislocation distribution in face-centred cubic metals after fatigue. *Philosophical Magazine*, **6**, 1493-1513.

Šitter, P., Luka' sˇ, P., Neov, D., Daymond, M. R., Nova'k, V., and Swallowe, G. M., 2002. Stress-induced martensitic transformation in Cu-Al-Zn-Mn polycrystal investigated by two in-situ neutron diffraction techniques, *Materials Science and Engineering A***, 324**, 225-234.

Stanley, P. and Chan, W. K., 1985. Quantitative stress analysis by means of the thermoelastic effect. *Journal of Strain Analysis*, 20, 129-143.

Stephens, P. W., 1999. Phenomenological model of anisotropic peak broadening in powder diffraction. *Journal of Applied Crystalline*, **32**, 281-289.

Sun, Y., Barabash, R. I., Choo, H., Liaw, P. K., Lu, Y. Brown, D. W., and Ice, G. E., 2007. Multiscale plastic deformation near a fatigue crack from diffraction. *Solid State Phenomena*, **129**, 151-156.

Suortti, P., Ahtee, M., and Unonius, L., 1979. Voigt function fit of x-ray and neutron powder diffraction profiles, *Journal of Applied Crystalline,* **12**, 365-369.

Suzuki, Y. and Egami, T., 1985. Shear deformation of glassy metals: breakdown of Cauchy relationship and anelasticity. *Journal of Non-Crystalline Solids*, **75**, 361-366.

Szekely, F., Groma, I., and Lendvai, J., 2001. Changes in the dislocation density fluctuations during plastic deformation. *Scripta Materialia*, **45**, 55-60.

Tahara, M., Kim, H. Y., Hosoda, H., and Miyazaki, S., 2009. Cyclic deformation behavior of a Ti-26 at.% Nb alloy. *Acta Materialia*, **57**, 2461-2469.

Talleb, L. and Hauet, A., 2009. Multiscale experimental investigations about the cyclic behavior of the 204L SS. *International Journal of Plasticity*, **25**, 1359-1385.

Taylor, G. I.., 1938. Plastic strain in metals*, Journal of Institute of Metals,* **62**, 307-324.

Thompson, N., 1959, *Fracture*, edited by Averbach, Technology Press.

Tomkins, B., 1968. Fatigue crack propagation – an analysis. *Philosophical Magazine,* **18**, 1041-1066.

Tomota, Y., Tokuda, H., Adachi, Y., Wakita, M., Minakawa, N., Moriai, A., and Morii, Y., 2004. Tensile behavior of TRIP-aided multi-phase steels studied by in situ neutron diffraction. *Acta Materialia*, **52**, 5737-5745.

Turkmen, H. S., Dawson, P. R., and Miller, M. P., 2002. The evolution of crystalline stresses of a polycrystalline metal during cyclic loading. *International Journal of Plasticity*, **18**, 941-969.

Ungar, T., Groma I., and Wilkens, M., 1989, Asymmetric x-raay-line broadening of plasticity deformed-crystals. 2. evaluation procedure and application to[001]-cu crystals, *Journal of Applied Crystalline,* **22**, 26-34.

Ungar, T., Biermann, H., and Mughrabi, H., 1993. Dislocation distributions as seen by X-ray line profiles. *Materials Science and Engineering A*, **164**, 175-179.

Ungar, T., Dragomir, I., Revesz, A. and Borbely, A., 1999. The contrast factors of dislocations in cubic crystals: the dislocation model of strain anisotropy in practice. *Journal of Applied Crystalline*, **32**, 992-1002.

Valiev, R. Z., Islamgaliev, R. K., and Alexandrov, I. V., 2000, Bulk nanostructured materials from severe plastic deformation, *Progress in Materials Science*, **45**, 103-189.

Von Dreele, R. B., Jorgensen, J. D., and Windsor, C. G., 1982, Rietveld Refinement with spallation neutron powder diffraction data, *Journal of Applied Crystalline*, **15**, 581-589.

Von Dreele, R. B., 2004. General structure analysis system. *Los Alamos National Laboratory Report,* LAUR 86-748, 160-165.

Wang, Y. D., Tian, H. B., Stoica, A. D., Wang, X.-L., Liaw, P. K., and Richardson, J. W., 2003. The development of grain-orientation-dependent-residual stresses in a cyclically deformed alloy. *Nature Materials,* **2**, 101-106.

Wang, Y. D., Wang, X.-L., Stoica, A. D., Almer, J. D., Lienert, U., and Haeffner, D. R., 2002, Separating the recrystallization and deformation texture components by high-energy X-rays, *Journal of Applied Crystalline,* **35**, 684-688.

Wang, Y. D., Peng, R. L., and McGreevy, R. L., 2001. A novel method for constructing the mean field of grain-orientation-dependent residual stress, *Philosophical Magazine Letter*, **81**, 153-163.

Wang, Y. D., Peng, R. L., Almer, J. D., Oden, M., Liu, Y. D., Deng, J. N., He, C. S., Li, Q. L., and Zuo, L., 2005, Grain-to-grain stress interactions in an electrodeposited iron coating, *Advanced Materials*, **17**, 1221-1226.

Weertman, J. R., 2002. *Mechanical Behavior of Nanocrystalline Metals in Nanostructured Materials: Processing, Properties, and Potential Applications*, William Andrew.

Wenk, H. R., Grigull, S., 2003. Synchrotron texture analysis with area detectors. *Journal of Applied Crystalline*, **36**, 1040-1049.

Will, G., 2006. *Powder Diffraction: The Rietveld Method and The Two-Stage Method*, **1**st edition, Springer.

Wilm, A., 1911, Zeitschrift für de gesamte Hüttenkunde. *Metallurgie*, **8**, 225-227.

Wong, A. K., Dunn, S. A., and Sparrow, J. G., 1988. Residual stress measurement by means of the thermoelastic effect. *Nature*, **332**, 613-615.

Wu, L, Jain A., Brown, D. W., Stoica, G. M., Agnew, S. R., Clausen, B., Fielden, D. E., and Liaw, P. K., 2008. Twinning-detwinning behavior during the strain-controlled low-cycle fatigue testing of a wrought magnesium alloy, ZK60A. *Acta Materialia,* **56**, 688-695.

Yang, B., Liaw, P. K., Morrison, M., Liu, C. T., Buchanan, R. A., Huang, J. Y., Kuo, R. C., Huang J. G., and Fielden, D. E., 2005. Temperature evolution during fatigue damage. *Intermatetallics,* **13**, 419-428.

Zehetbauer, M., 1993. Cold work-hardening in stage-IV and stage-V of fcc metals. 2. model fits and physical results. *Acta Metallurgica et Materialia,* **41**, 589-599.

Zhang, P., Duan, Q. Q., Li, S. X., Zhang, Z. F., 2008. Cyclic deformation and fatigue cracking behaviour of polycrystalline Cu, Cu-10wt% Zn and Cu-32wt% Zn. *Philosophical Magazine,* **88**, 2487-2503.

Zener, C., 1937. Internal frication in solids. *Physical Review,* **52**, 230-235.

Zener, C., 1938. Internal friction in solids II. General theory of thermoelastic internal friction. *Physical Review,* **53**, 90-98.

Appendix

Table 1-1. The composition of the HASTELLOY® C-22 HS™ alloy

HASTELLOY C-22 HS	Ni	Cr	Mo	W	Fe	C
Weight Percentage	61	21	17	1*	2*	0.01*
*maximum						

Table 2.1 Direction cosines for principal directions in a cubic lattice

Direction	$l_1, x = \langle 100 \rangle$	$l_2, y = \langle 010 \rangle$	$l_3, z = \langle 001 \rangle$
$v = \langle 100 \rangle$	1	0	0
$v = \langle 110 \rangle$	$1/\sqrt{2}$	$1/\sqrt{2}$	0
$v = \langle 111 \rangle$	$1/\sqrt{3}$	$1/\sqrt{3}$	$1/\sqrt{3}$

Table 2-2: classification of different methods (Will 2006)

	Profile fitting method	**Whole-pattern decomposition**	**Rietveld refinement method**
Aim of analysis	Pattern decomposition	Pattern decomposition and refinement of unit cell parameters	Structure refinement
Range of analysis	Local peaks or peak clusters	Whole pattern	Whole pattern
Peak position	Independent parameters	Function of unit cell parameters	Function of unit cell parameters
Integrated intensities (profile area)	Independent parameters	Independent parameters	Function of structural parameters
Initial parameters required to start refinement	Nil	Approximate unit cell parameters	Initial structural parameters (structural model)

Table 2-3: Profile shape functions commonly used in profile fitting programs (Will 2006)

Gaussian	$G = I_0 \exp\left(-\ln 2\left(\frac{2\Theta - 2\Theta_0}{w}\right)^2\right)$
Lorentzian	$L = I_0\left(1+\left(\frac{2\Theta - 2\Theta_0}{w}\right)^2\right)^{-n}$ where $n = 1;\ 1.5;\ 2$
Pseudo-Voigt function	$V = \eta L + (1-\eta)G$ $(0 \le \eta \le 1)$
Parameters:	2Θ = peak position I_0 = peak intensity $w = \frac{\text{Full width half maximum (FWHM)}}{2}$ m = shape parameter

Table 3-1: Slip system considered in the current study

Edge dislocation	**slip plane**			**Burgers vector**		
Slip system no.	h	K	l	u	V	w
1	1	1	1	1	$\bar{1}$	0
2	1	1	1	0	1	$\bar{1}$
3	1	1	1	1	0	$\bar{1}$
4	$\bar{1}$	1	1	1	1	0
5	$\bar{1}$	1	1	0	1	$\bar{1}$
6	$\bar{1}$	1	1	1	0	1
7	1	1	$\bar{1}$	1	$\bar{1}$	0
8	1	1	$\bar{1}$	0	1	1
9	1	1	$\bar{1}$	1	0	1
10	1	$\bar{1}$	1	1	1	0
11	1	$\bar{1}$	1	1	0	$\bar{1}$
12	1	$\bar{1}$	1	0	1	1
Screw dislocation	**dislocation line**			**Burgers vector**		
Slip system no.	τ_x	τ_y	τ_z	u	V	w
1	1	$\bar{1}$	0	1	$\bar{1}$	0
2	0	1	$\bar{1}$	0	1	$\bar{1}$
3	1	0	$\bar{1}$	1	0	$\bar{1}$
4	1	1	0	1	1	0
5	1	0	1	1	0	1
6	0	1	1	0	1	1

Table 3-2: Material parameters used in VPSC simulations for the alloy: Q denotes the thermal-expansion coefficient; τ_0 and θ_1 are the critical resolved stress and the hardening parameter, respectively; C_{11}, C_{12} and C_{44} are the single crystal elastic constants.

Q (*10^{-6})	**τ (MPa)**	**θ (MPa)**	Single crystal elastic constants (GPa)		
			C_{11}	C_{12}	C_{44}
18	135	450	303.0	210.0	106.0

Table 3-3: the probability of the active slip system {*hkl*}<*uvw*> of the grains which could diffract to the detection banks

The grain oriented to the loading direction						
H	***k***	***l***	***u***	***v***	***w***	**Probability**
1	1	1	0	1	$\bar{1}$	7.60%
1	1	1	1	0	$\bar{1}$	24.14%
$\bar{1}$	1	1	1	0	1	33.28%
1	1	$\bar{1}$	0	1	1	14.69%
1	$\bar{1}$	1	0	1	1	8.49%
The grain oriented to the transverse direction						
H	***k***	***l***	***u***	***v***	***w***	**Probability**
1	1	1	0	1	$\bar{1}$	0.81%
1	1	1	1	0	$\bar{1}$	29.20%
$\bar{1}$	1	1	0	1	$\bar{1}$	6.37%
$\bar{1}$	1	1	1	0	1	40.14%
1	1	$\bar{1}$	0	1	1	23.48%

Table 3-4: The slip-system-dependent contrast factor, screw dislocation density (n), edge dislocation-wall spacing (D) of the specifically-oriented grain in the loading direction at 825 MPa.

$\vec{b}_i$	Detection-bank directions	Contrast Factor		n (10^8cm^{-2})	D (nm)
		edge wall	random screw		
[100]	loading	0.27	0.19	142 (± 1.5)	785 (± 16)
[010]	transverse	0.25	0.18	148 (± 1.6)	762 (± 15)

Table 5-1: The stresses (MPa) of the specific fatigue cycles during the Stage 3

Fatigue cycles / **Loading Status**	*1,000th*	*1,500th*	*2,000th*	*2,500th*
Tension *(+ 1%)*	*544.2*	*544.5*	*543.6*	*540.8*
Compression *(- 1%)*	*-536.5*	*-537.3*	*-537.7*	*-538.1*

Table 6-1: The Structural information of the nano precipitates (unit: Å)

Aged alloys (containing nano precipitates)	Undeformed		Deformed (30% elongation)	
	SANS	TEM	SANS	TEM
Inter-precipitate distance (L)	148.3 ± 1.0	158.8	147.1 ± 2,8	135.3
variance of L (σ)	81.0 ± 0.6	75.8	95.2 ± 1.2	85.9
Radius of the precipitates (R)	57.5 ± 0.5	60.0 [7]	64.1 ± 1.9	64.7
variance of R (δ)	13.1 ± 0.2	50.0 [7]	13.6 ± 0.4	51.2
Aspect ratio of the precipitates (ε)	0.67 ± 0.03	0.64	0.58 ± 0.03	0.50
Volume ($Å^3$)	$(3.57\pm0.36)\times10^5$	3.29×10^5	$(3.70\pm0.67)\times10^5$	3.68×10^5

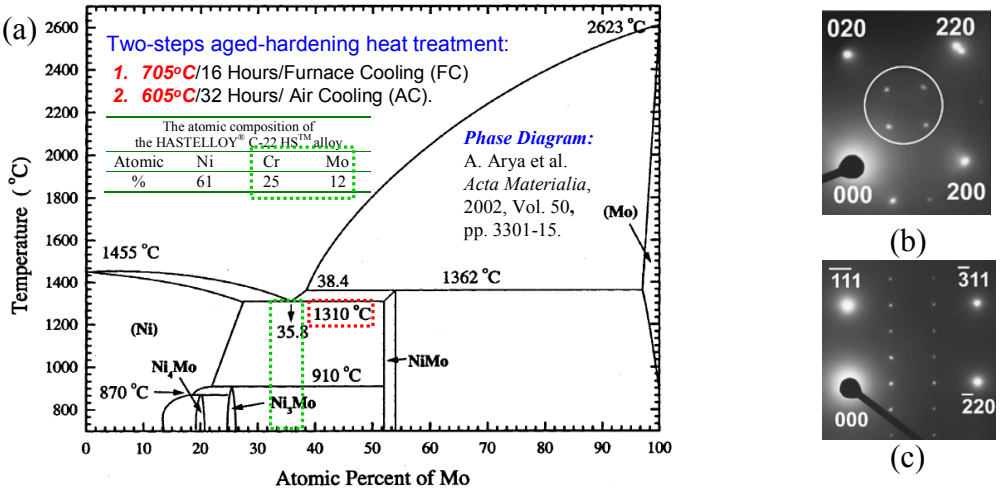
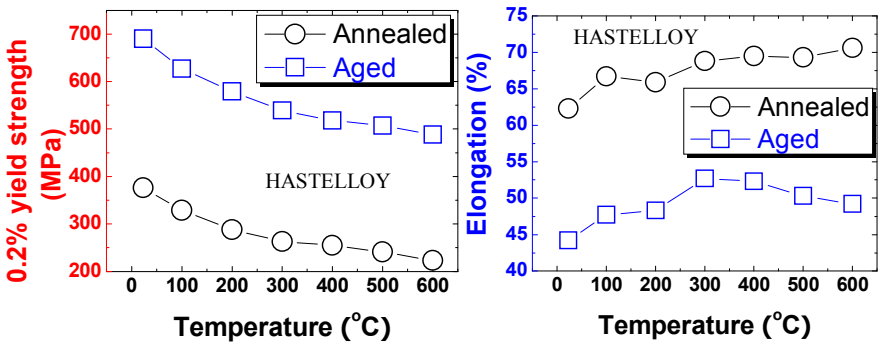


Figure 1-1 (a) The phase diagram of the precipitation treatment (Arya *et al.* 2002). TEM diffraction of the aged alloys (Lu *et al.* 2007): (b) [001] zone-axis diffraction pattern, and (c) [112] zone-axis diffraction pattern. The marked diffraction spots are from the f.c.c. matrix. The weaker diffraction at the centers are from the $Ni_2(Cr, Mo)$ precipitates.



(a) (b)

Figure 1-2: The mechanical properties as a function of the temperature of the annealed and the aged alloys, respectively. (a) The yield strength. (b) The elongation.

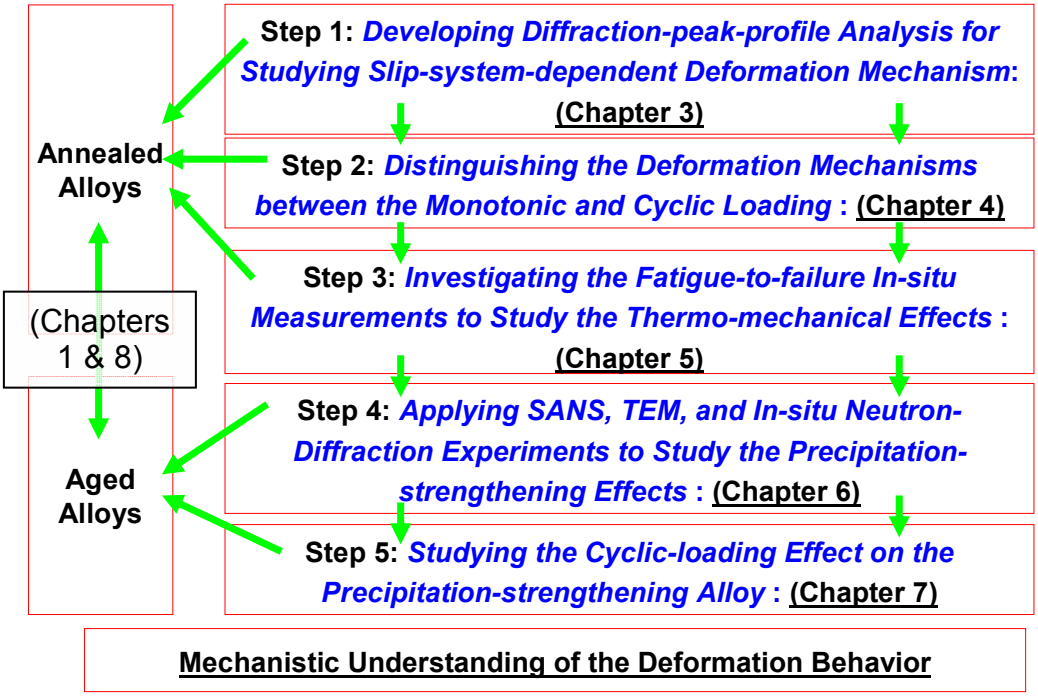


Figure 1-3: Summary of the research plans.

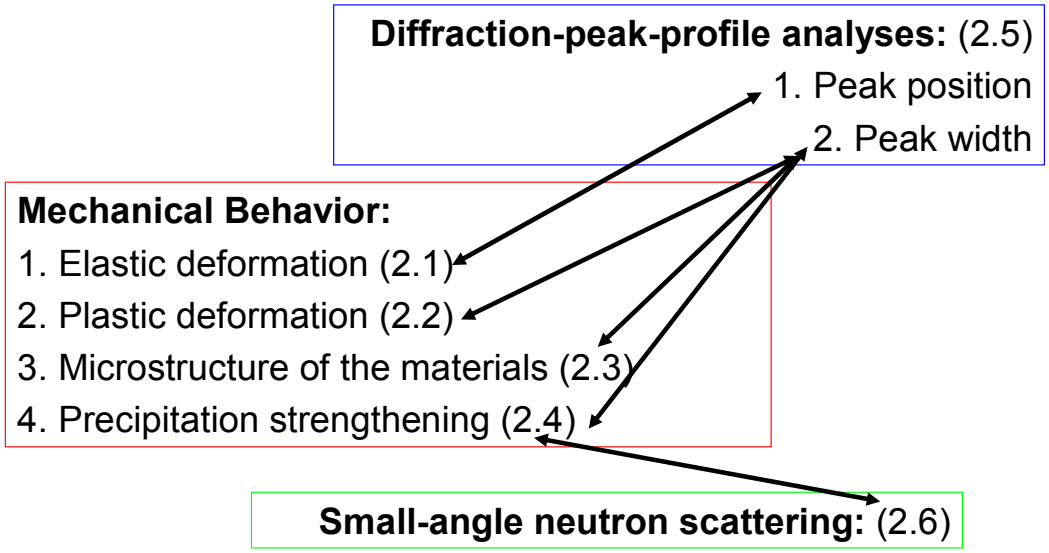


Figure 2-1: The outline of Chapter 2

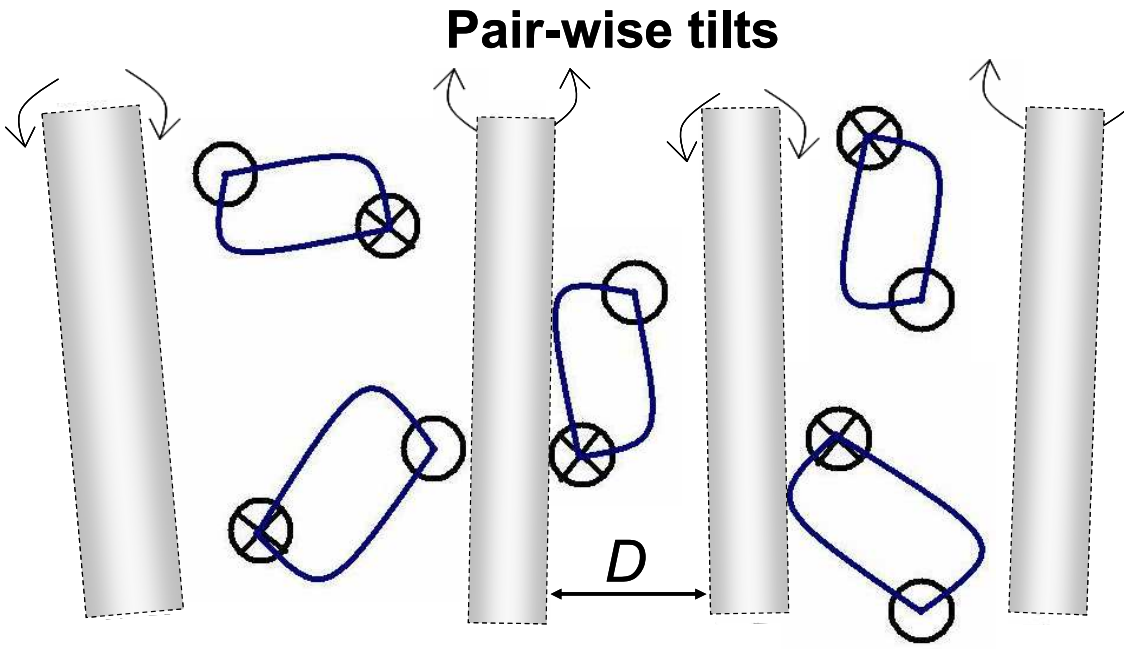
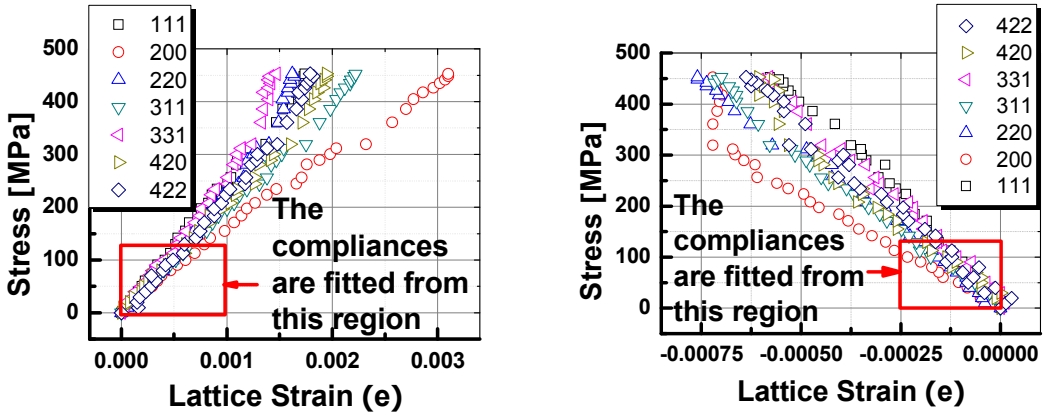


Figure 3-1: The sketch of the patterned structure with dislocation walls and the randomly distributed dislocations. Each wall creates the pair-wise tilt between two adjacent regions. The shadow regions near each wall indicate where strain field from dislocations within the wall are significant.



(a) Loading direction (b) Transverse direction

Figure 3-2: The lattice strain-stress curves of *hkl* 111, 200, 220, 311, 331, 420, and 422. The linearity starts to deviate about 370 MPa, corresponding to the 0.2% yield strength. (a) Loading and (b) Transverse directions.

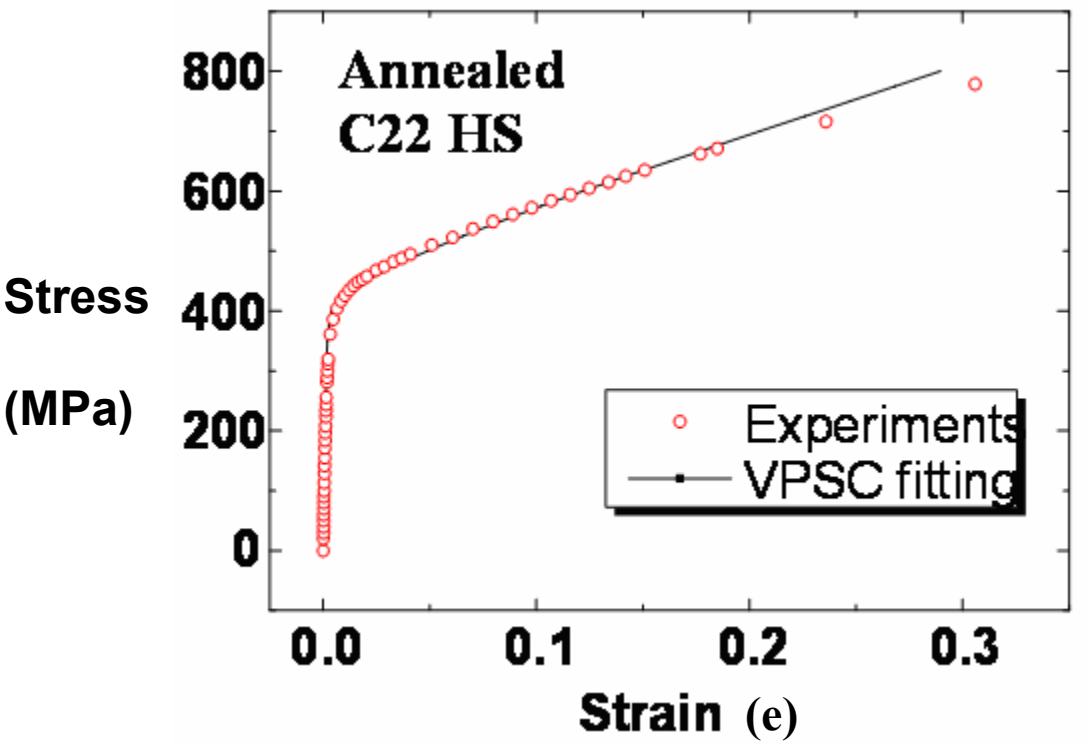
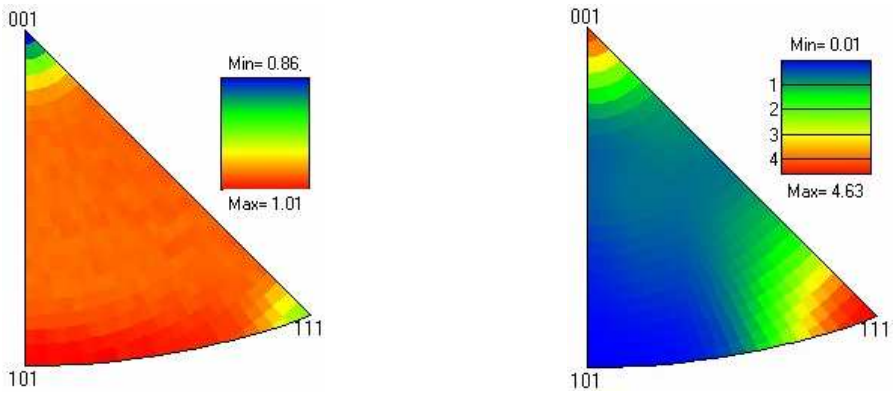


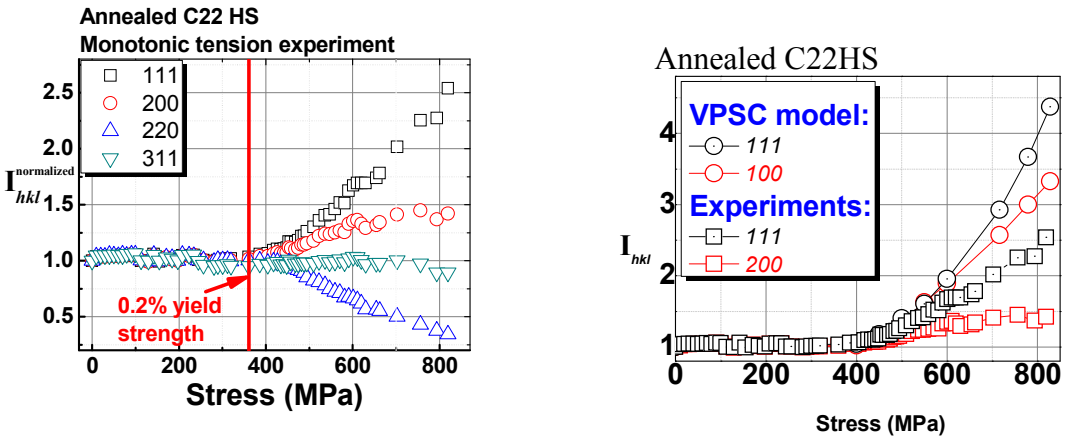
Figure 3-3: Stress-strain curve of the alloy for a monotonic-tension experiment. The measurements are depicted in open symbols, and VPSC fitting is in a solid line.

The VPSC-simulated, inverse-pole figures along the loading direction



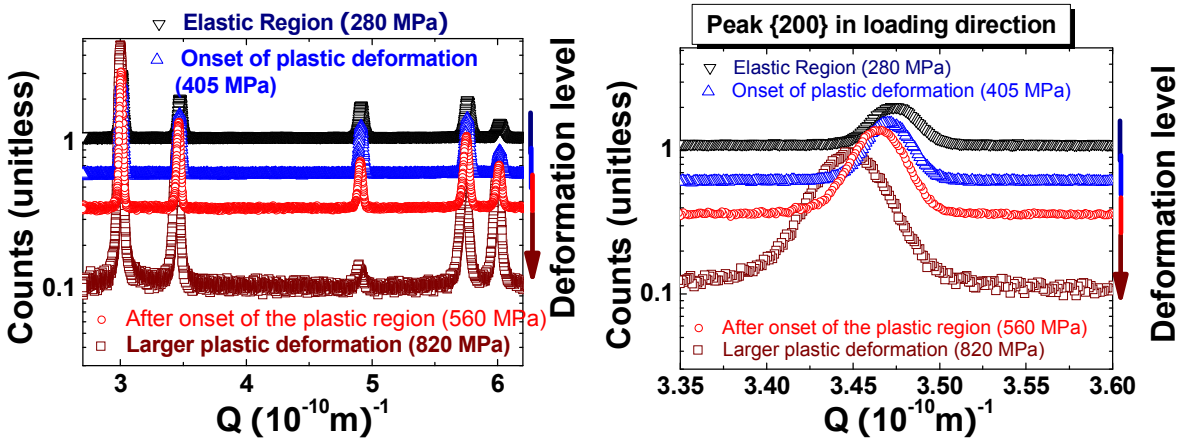
(a) Initial (b) After plastic deformation

Figure 3-4: The simulated inverse pole figures of the alloy in two different states: (a) initial texture within the elastic region, and (b) after the onset of the plastic deformation at about 825 MPa of the stress-strain curve in Figure 3-2.



(a) (b)

Figure 3-5: (a) The normalized integrated intensity, using Equation (3-2), versus true stress. For clarity, the data is plotted for the loading direction. The perpendicular red line represents the macroscopic 0.2% yield strength. (b) The simulated VPSC texture development along loading direction. There is a stronger texture in {111} pole than that of {100} pole as measured in (a).



(a) (b)

Figure 3-6: (a) The selected diffraction profiles measured along loading direction in a sequence from top-to-bottom at the stress: 280, 405, 560, and 820 MPa, respectively. (b) The enlargement of the peaks {200} from (a) in different loading levels. There are clear changes in peak positions, intensity and widths, where the sources of the peak-width broadening may come from the randomly-distributed dislocations and dislocation walls. Note that the raw data in (a) and (b) includes instrumental broadening. For calculations of dislocation structure parameters, the peak width was corrected to take into account of the instrumental broadening. Thus, the broadening induced from dislocation substructures can be refined. For example, the peak-broadening induced by the dislocation-related structure is about 45% of the value shown in (b) at the larger plastic deformation level of 820 MPa.

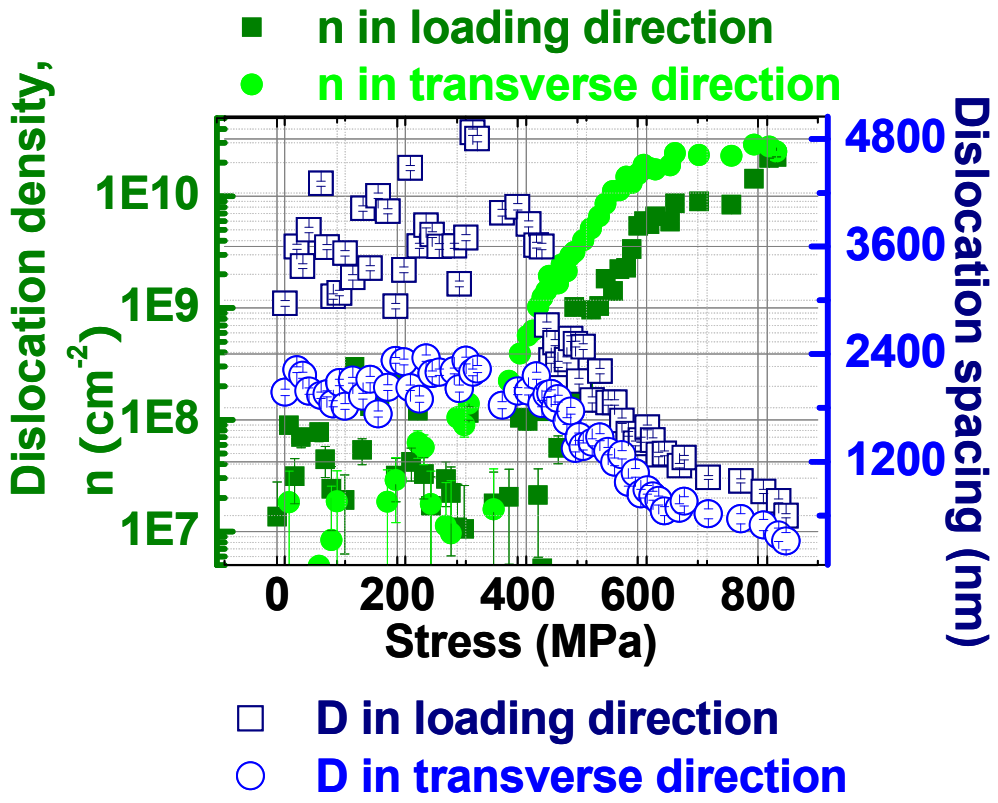
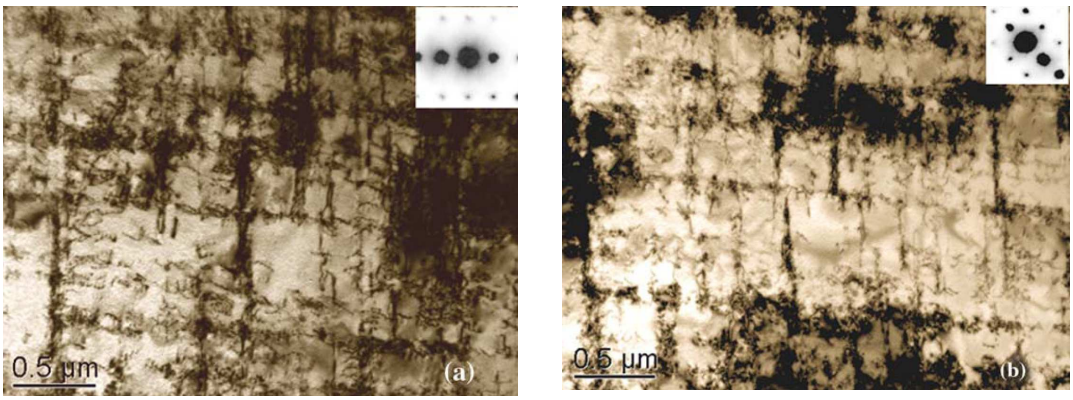


Figure 3-7: The trends of the dislocation wall spacing evolution (□ in the loading direction and ○ in the transverse direction) and density evolution (■ in the loading direction and ● in transverse direction).



(a) (b)

Figure 3-8: TEM images obtained from the sample after 40 pct deformation demonstrating the formation of the hierarchical dislocation structure with walls and some part of random dislocations between them: (a) diffraction vector g = [*111*], electron beam direction, B, near [$\bar{1}\bar{1}2$]; and (b) g = [*200*], B near [*001*], foil normal near (*001*). Due to different orientations of the diffraction vector, some dislocations become invisible at one of the images. Note that the dislocation walls are {*110*} and are not aligned on {*001*}.

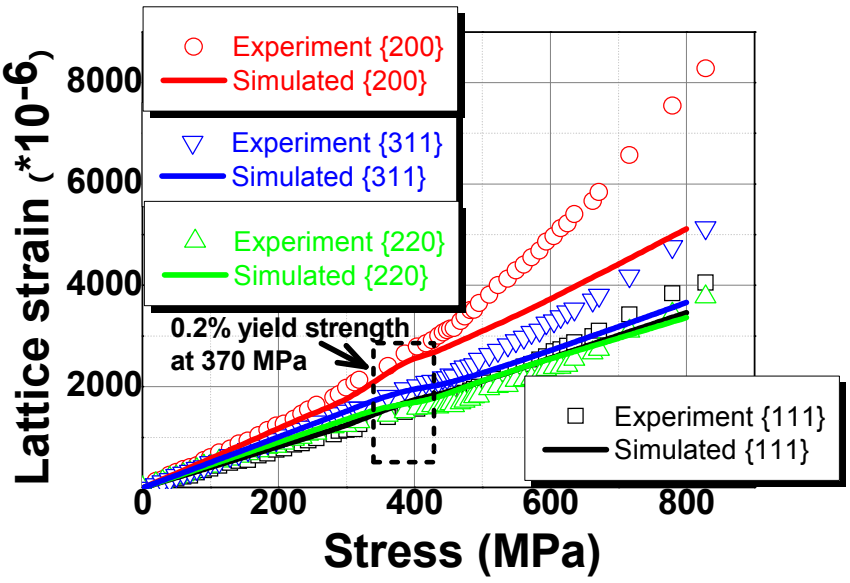


Figure 3-9: Response of the measured (symbols) and the simualted (lines) lattice strains to the load along the loading direction for {111} in ■ , {200} in ●, {220} in ▲, and {311} in ▼. The simulated and the experimental results show qualitative equivalence as the {200} in ● increases fastest, while the {110} in ■ increases the least. Quantitatively, the simulation and the measurements almost match correspondingly to stress up to 370 MPa. However, the simulated lines start to show less lattice-strain responses deviated from the measured data about 400 MPa. Although the qualitative trends keep the same from the simulated to the measured, the simulated {200} lattice-strain is about 2,500 με less than that of the measured at stress equals to 800 MPa.

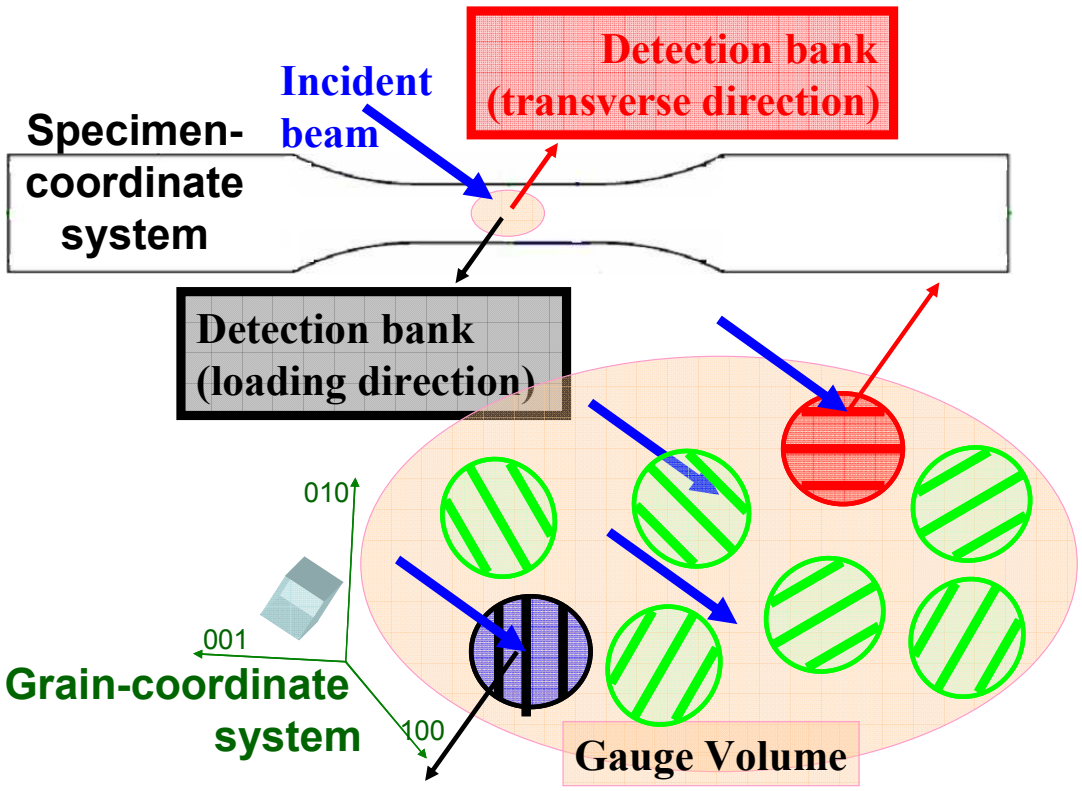
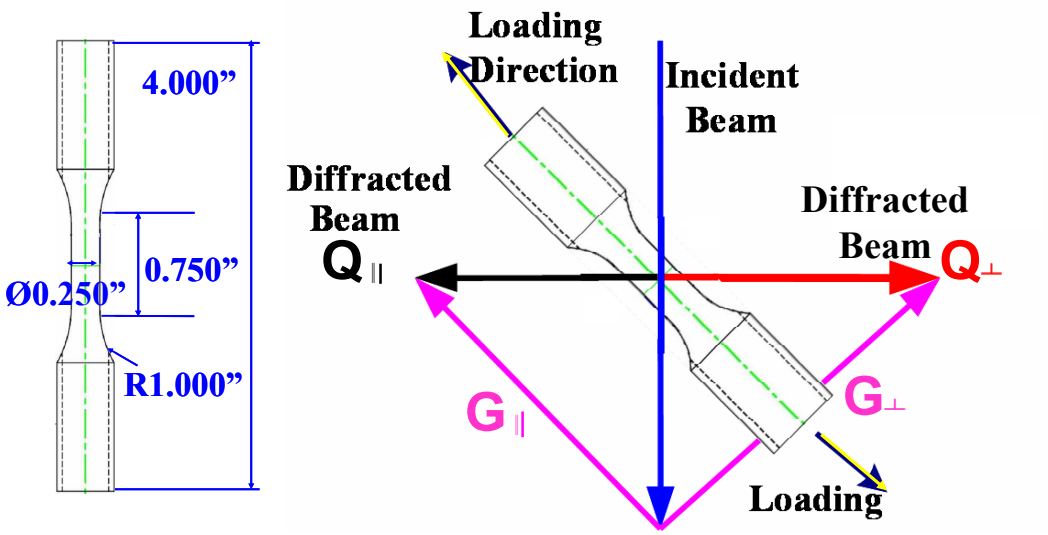
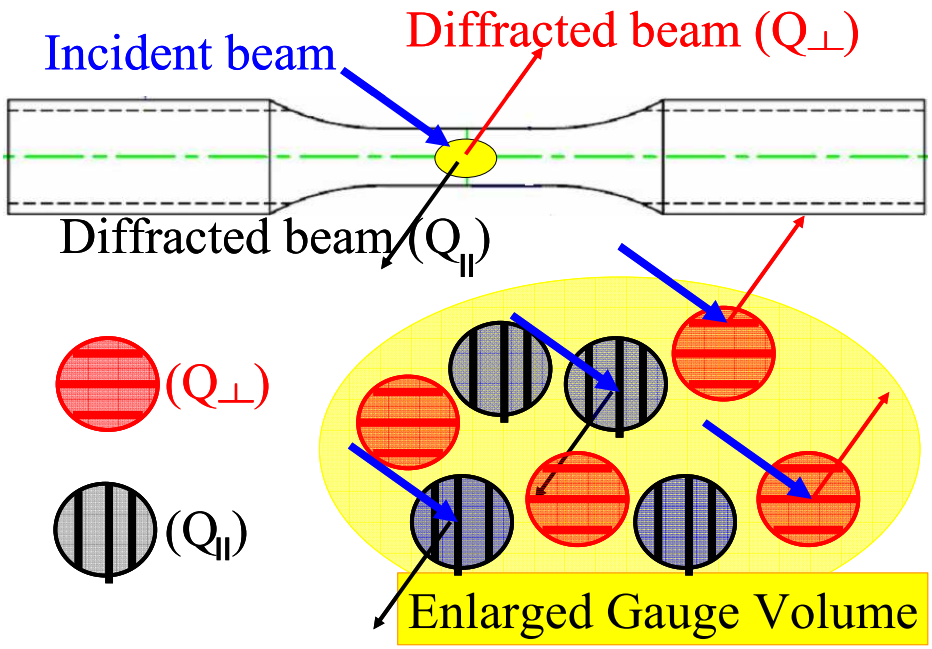


Figure 3-10: The simulated grains reorient after deformation as the grain-orientation system (bottom-left). Only the specifically-oriented grains are assumed to be measured at specific part of Debye ring from the gauge volume (bottom-right). The directions are based on the specimen-coordinate system, fixed by two detection banks as shown on top.

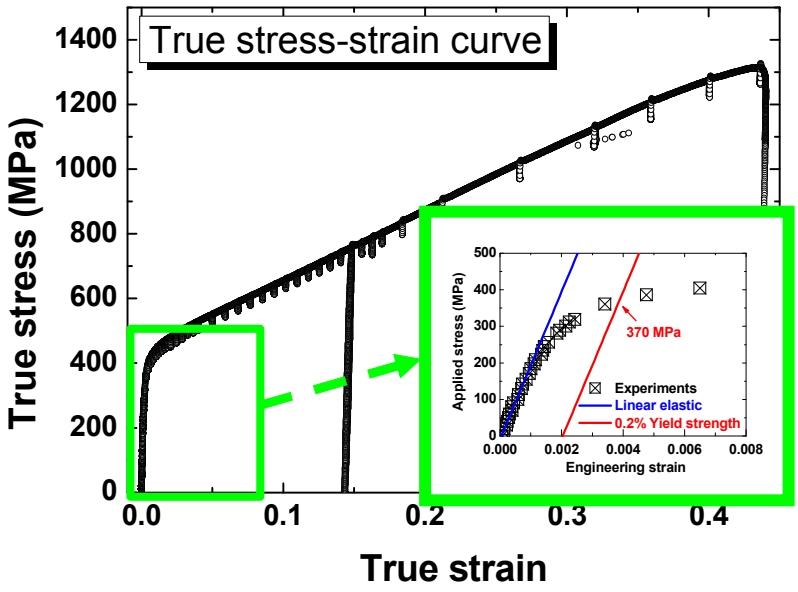


(a) Specimen geometry (b) Neutron beam path



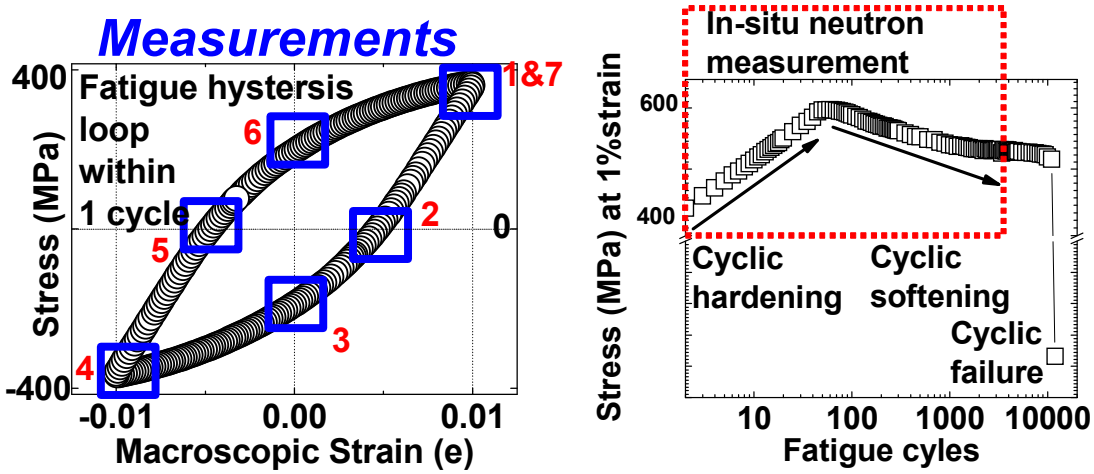
(c) Schematic grain-oriented-dependent diffraction

Figure 4-1: (a) The geometry of the specimen. (b) A schematic view of the neutron beam path for measurement. (c) The schematic plot shows that only the grains satisfying Bragg’s condition diffract the incident neutrons to the detector banks. The grains with {*hkl*} planes along loading direction ($Q_{//}$) are shown in gray. The grains with {*hkl*} planes in the transverse direction ($Q_{\perp}$) are shown in red.



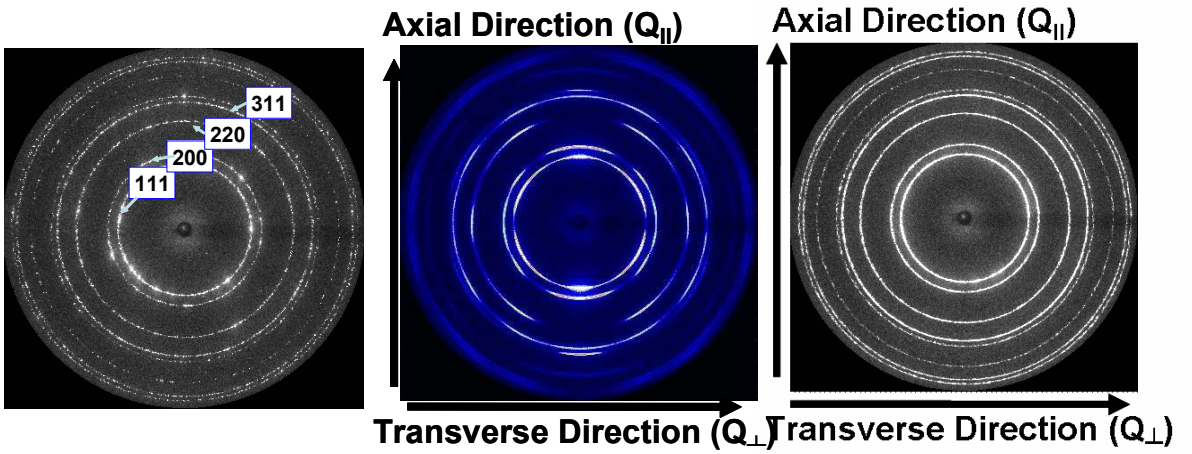
Monotonic tension experiments

Figure 4-2: True stress-true strain curve of the alloy for the monotonic experiment. The intersection is the enlargement of the early straining curve to show the onset of the plastic deformation.



(a) Seven Measurements (b) Cyclic loadings

Figure 4-3: (a) Seven measurements of the low-cycle-fatigue experiments within one fatigue cycle. (b) Stress at 1% strain (Measurement 1) is plotted as a function of fatigue cycles. Several in-situ neutron experiments were conducted within 1,500 fatigue cycles. In the beginning, the stress increase as fatigue cycle increases until 600 MPa at 100th cycle, and then decreases.



(a) Undeformed (b) Tension-deformed (c) Cyclic-deformed

Figure 4-4: The high-energy synchrotron-diffraction patterns collected from the (a) undeformed alloy, (b) tensile-deformed specimen, and (c) cyclic-deformed specimen. As the arrows depicted, the intensity of different diffraction rings can be compared with respect to the axial and transverse directions.

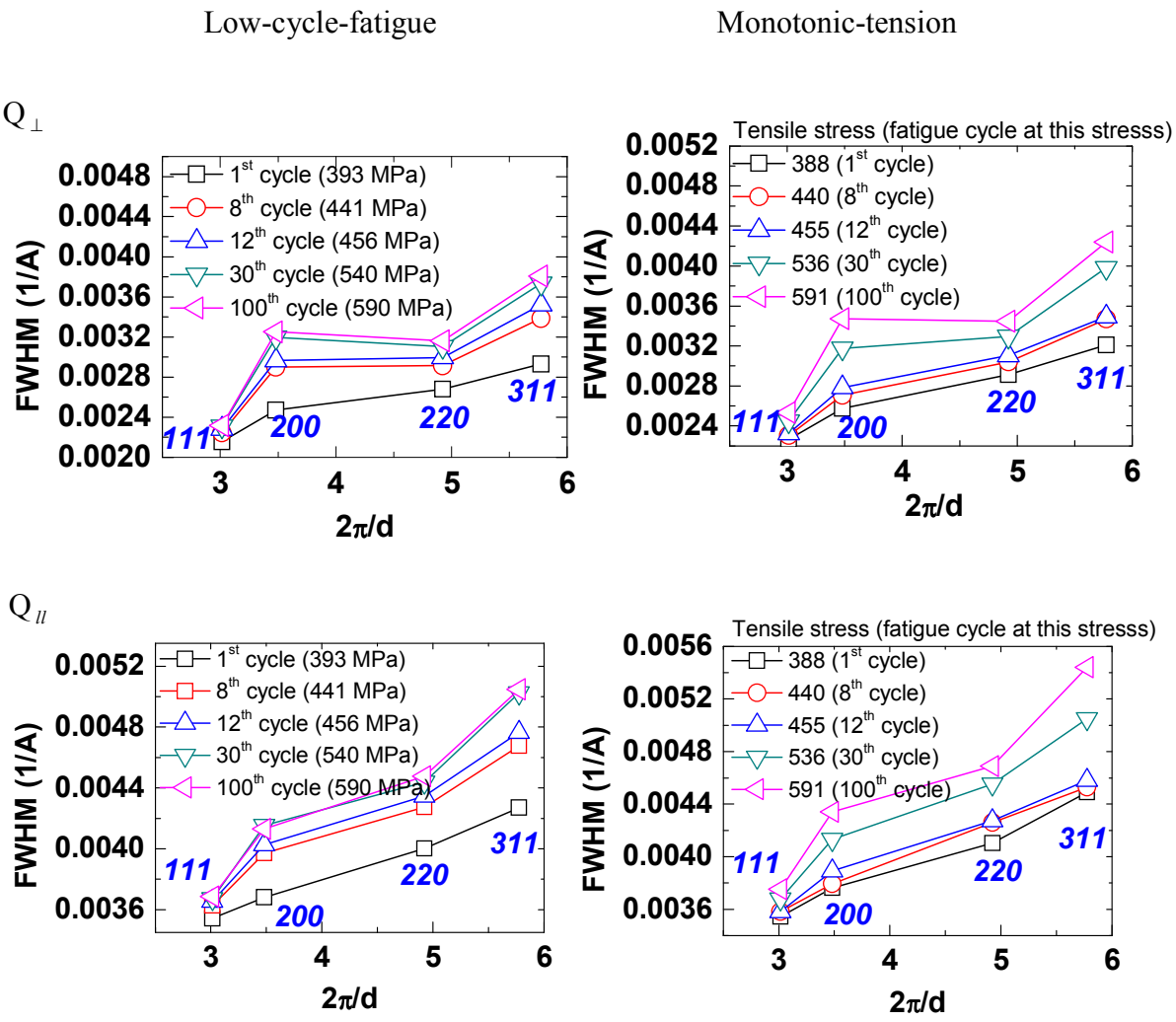
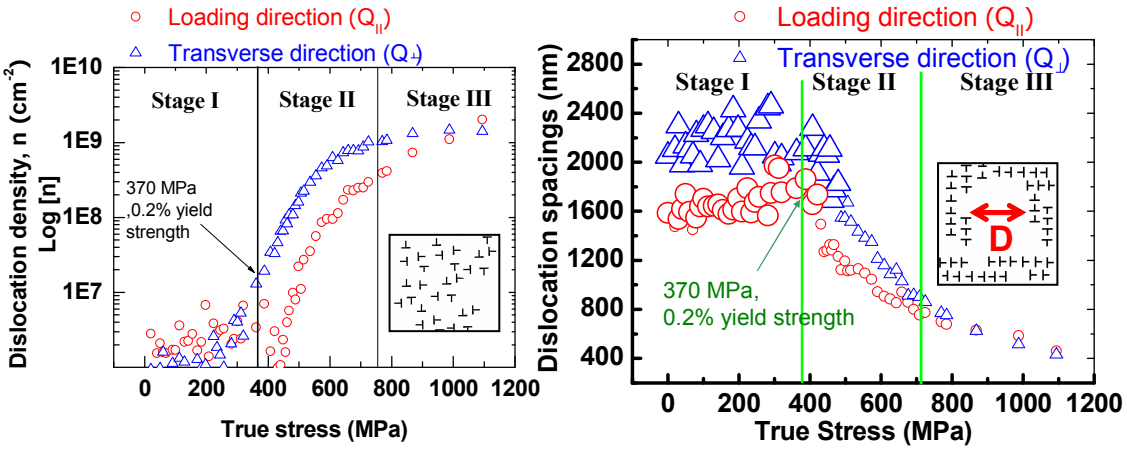


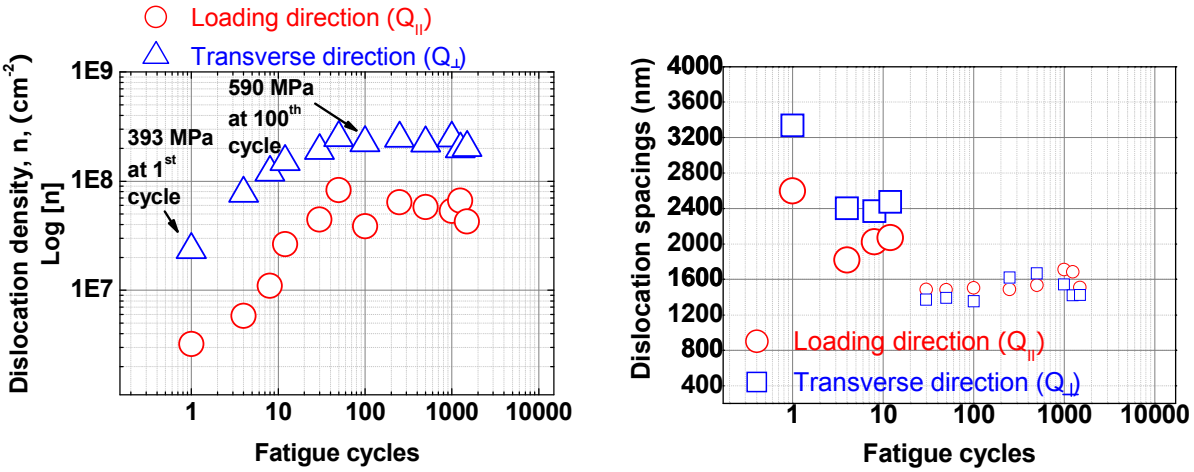
Figure 4-5: FWHM versus $2\pi/d$ for low-cycle-fatigue and monotonic-tension experiments in $Q_{\perp}$ and $Q_{//}$ directions.



(a) Dislocation density (b) Dislocation walls spacing

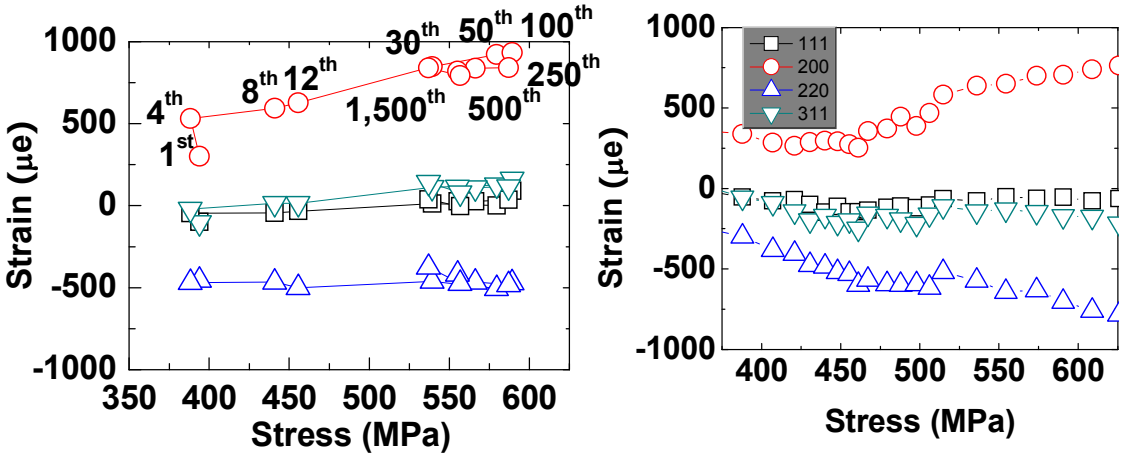
Figure 4-6: (a) The dislocation density versus true stress. The line between Stages I and II represents the macroscopic 0.2% yield strength. The inset shows a scheme of the randomly distributed dislocations at the bottom-right corner. (b) Dislocation-wall spacing within dislocation walls as a function of the true stress. The dislocation-wall spacing (D) is shown in the inset of the upper-right corner. The bigger legends of Figure (b) show the higher uncertainty for the size greater than 1,500 nm. For clarity, the data is plotted for along ($\|$) and ($\perp$) perpendicular to the loading direction.

Low-cycle-fatigue experiments



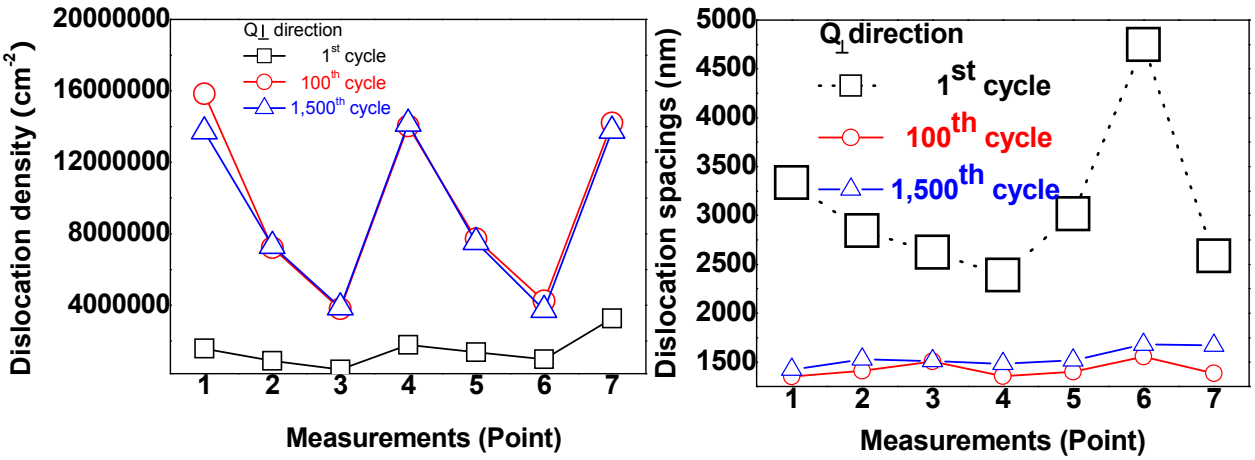
(a) Dislocation density (b) Dislocation walls spacing

Figure 4-7: (a) The dislocation density and (b) dislocation-wall spacings as a function of fatigue cycles at 1% strain. Note: the bigger legends of Figure (b) in early fatigue cycles show the greater fluctuations for the measured size greater than 1,500 nm. For clarity, the data is plotted for along ($\parallel$) and ($\perp$) perpendicular to the loading direction. The true stress is 393 MPa at 1st and 590 MPa at 100th fatigue cycles.



(a) Low-cycle-fatigue (b) Monotonic-tension

Figure 4-8: Intergranular strains as a function of true stress in the same stress levels (the elastic portion of the lattice strains were subtracted from the measured lattice strains) of (a) low-cycle-fatigue experiments at Measurement 1 (fatigue cycles are marked along Peak 200) and (b) monotonic-tension experiments.



(a) Dislocation density (b) Dislocation walls spacing

Figure 4-9: (a) The dislocation density and (b) the dislocation-wall spacing evolutions within one fatigue cycle at 1st (black), 100th (red), and 1,5000th fatigue cycles in $Q_{\perp}$ direction. The conditions of 7 measurements are shown in Figure 4-3(a) as the insert.

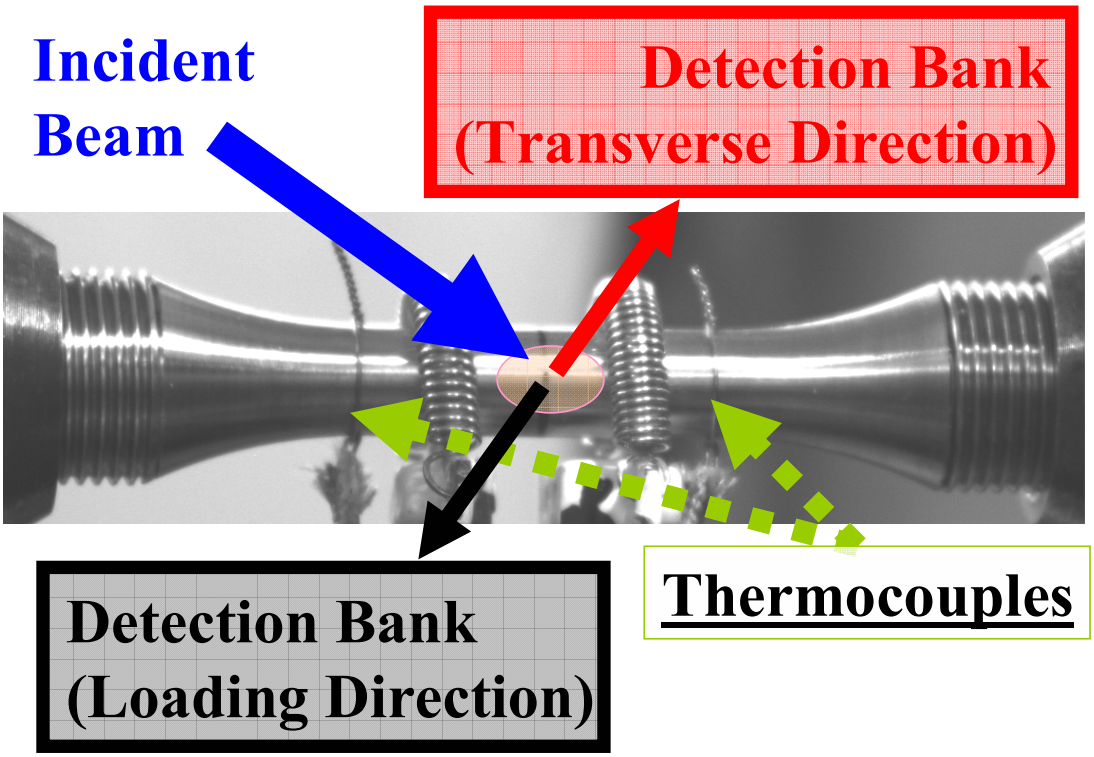


Figure 5-1: Photo of the in-situ measurement configuration at SMARTS. The schematic arrows show that the grains, in loading and transverse directions, satisfying Bragg's condition diffract the incident neutrons to the two orthogonal detector banks, respectively.

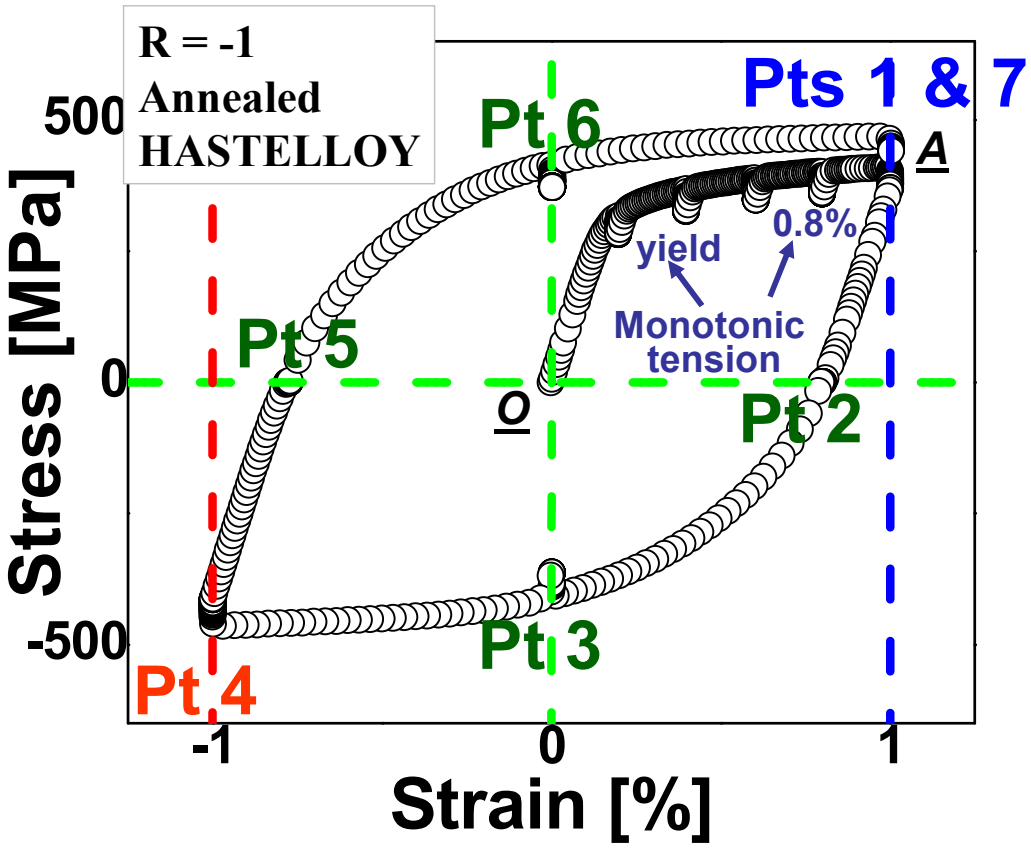


Figure 5-2: The stress-strain curves of the monotonic tension (***OA***) and the seven measurement *points* within the first fatigue cycle. At *0 MPa* are *Pts 2 and 5*, respectively; At *0%* strain are *Pts 3 and 6*, respectively; At *1%* strain are *Pts 1 and 7*; At - *1%* is *Pt 4*, respectively.

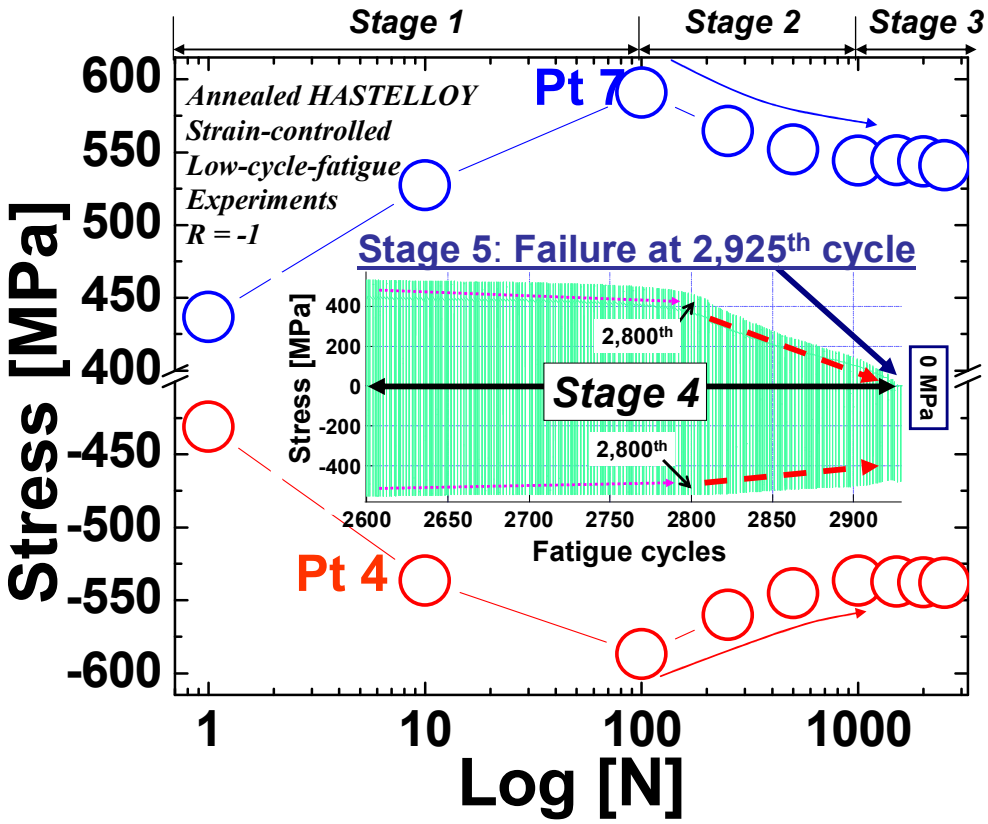


Figure 5-3: The stress evolution at the maximum tension (*Pt 7*) and compression (*Pt 4*) as a function of the fatigue cycle. Stage 1: cyclic hardening up to the 100^{th}-fatigue cycle. Stage 2: cyclic softening (100^{th} ~ $1{,}000^{th}$ cycles). Stage 3: saturation cycles ($1{,}000^{th}$ ~ $2{,}500^{th}$ cycles). The inset shows Stage 4 ($2{,}500^{th}$ ~ $2{,}924^{th}$ cycles), and Stage 5 as the specimen cyclically failed at the $2{,}925^{th}$ cycle.

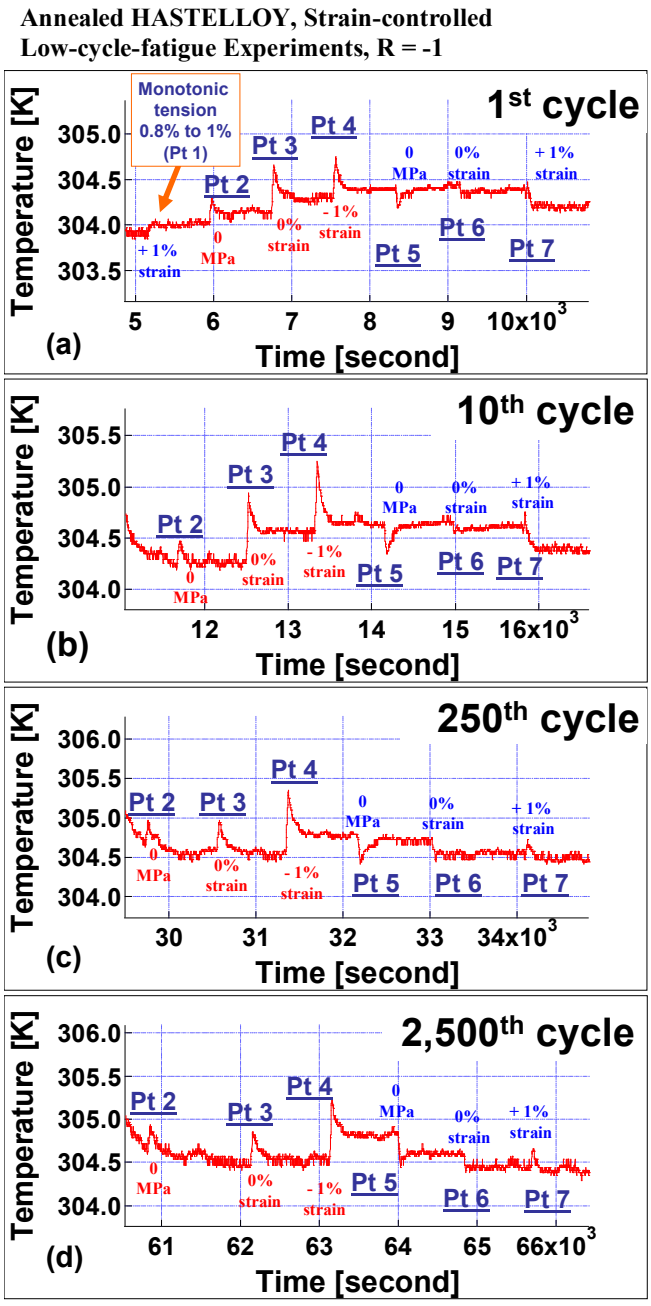


Figure 5-4: In-situ temperature measurements. The x-axis is the time of the overall in-situ experiments. The specific measurements are identified and marked accordingly as *Pts 2, 3, 4, 5, 6*, and *7*, individually. (a) The initial monotonic tension load and the *1st* fatigue cycle. (b) The 10th fatigue cycle. (c) The *250th* fatigue cycle. (d) The *2,500th* fatigue cycle. The increased background temperature in the beginning of the 10th, 250th, and 2,500th comes from the accumulated heating of the consecutive fatigue cycles prior to the start of *Pt1 (+ 1%* strain) of each measurement.

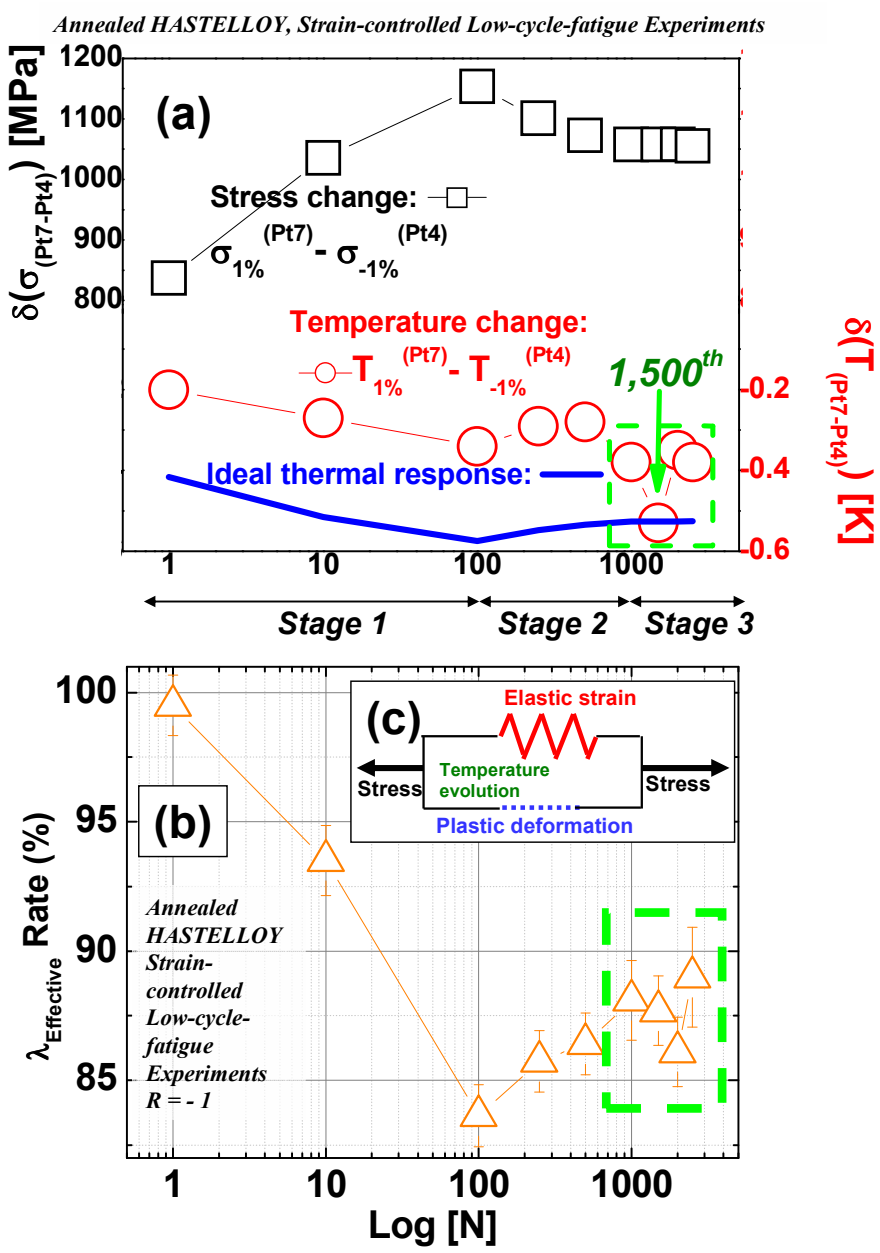


Figure 5-5: The bulk-parameter evolution. The changes from the maximum compression (*Pt 4*) to tension (*Pt 7*). Upper: stress differential of Pts 4 and 7 ($\delta\sigma$) in MPa within one fatigue cycle. Bottom: temperature differential (δT) in K. There is a non-monotonic temperature evolution after the 500^{th} fatigue cycle marked in the dashed box. The transition in this region is at the $1{,}500^{th}$ fatigue cycle.

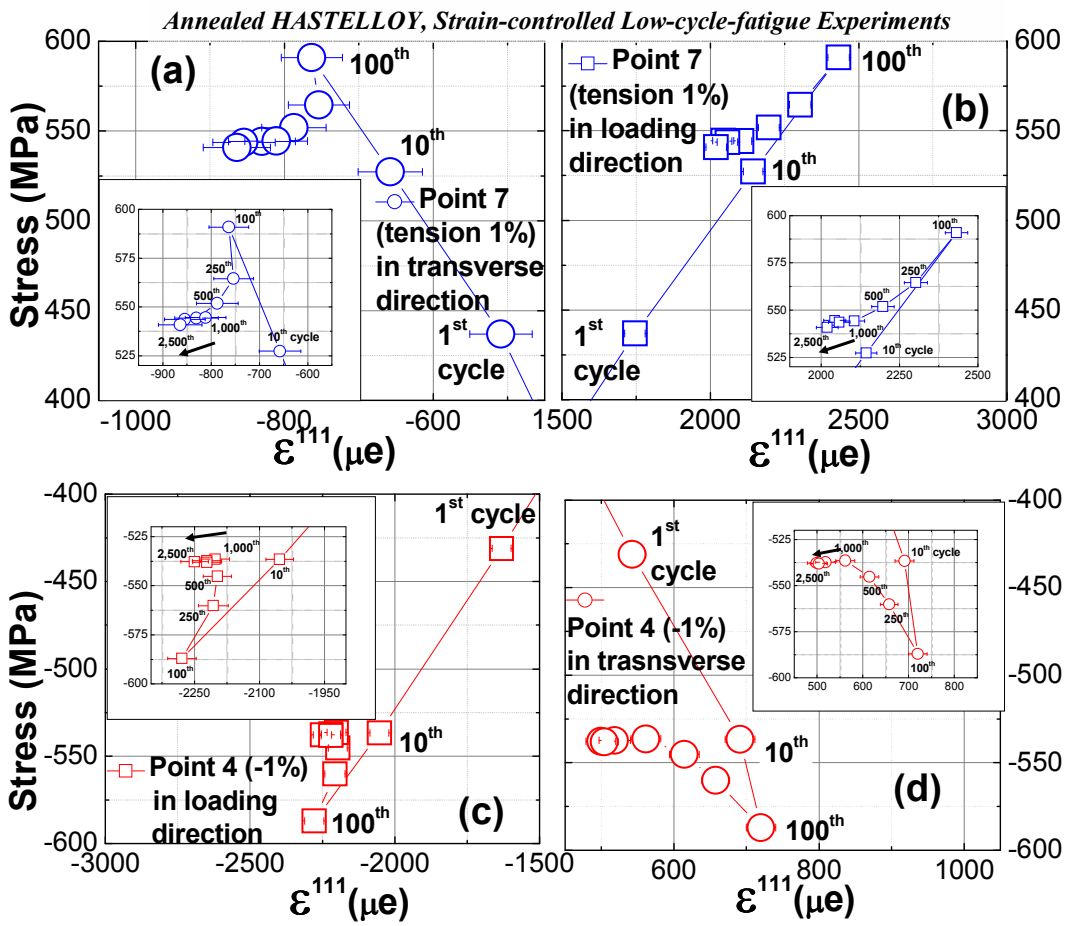


Figure 5-6: The *{111}* lattice strain (ε^{111}) -stress curves of the maximum tension (*Pt 7*) and compression (*Pt 4*) in loading and transverse directions, respectively. (a) $\varepsilon^{111}_{tension}$ in transverse direction. (b) $\varepsilon^{111}_{tension}$ in loading direction. (c) $\varepsilon^{111}_{compression}$ in loading direction. (d) $\varepsilon^{111}_{compression}$ in transverse direction.

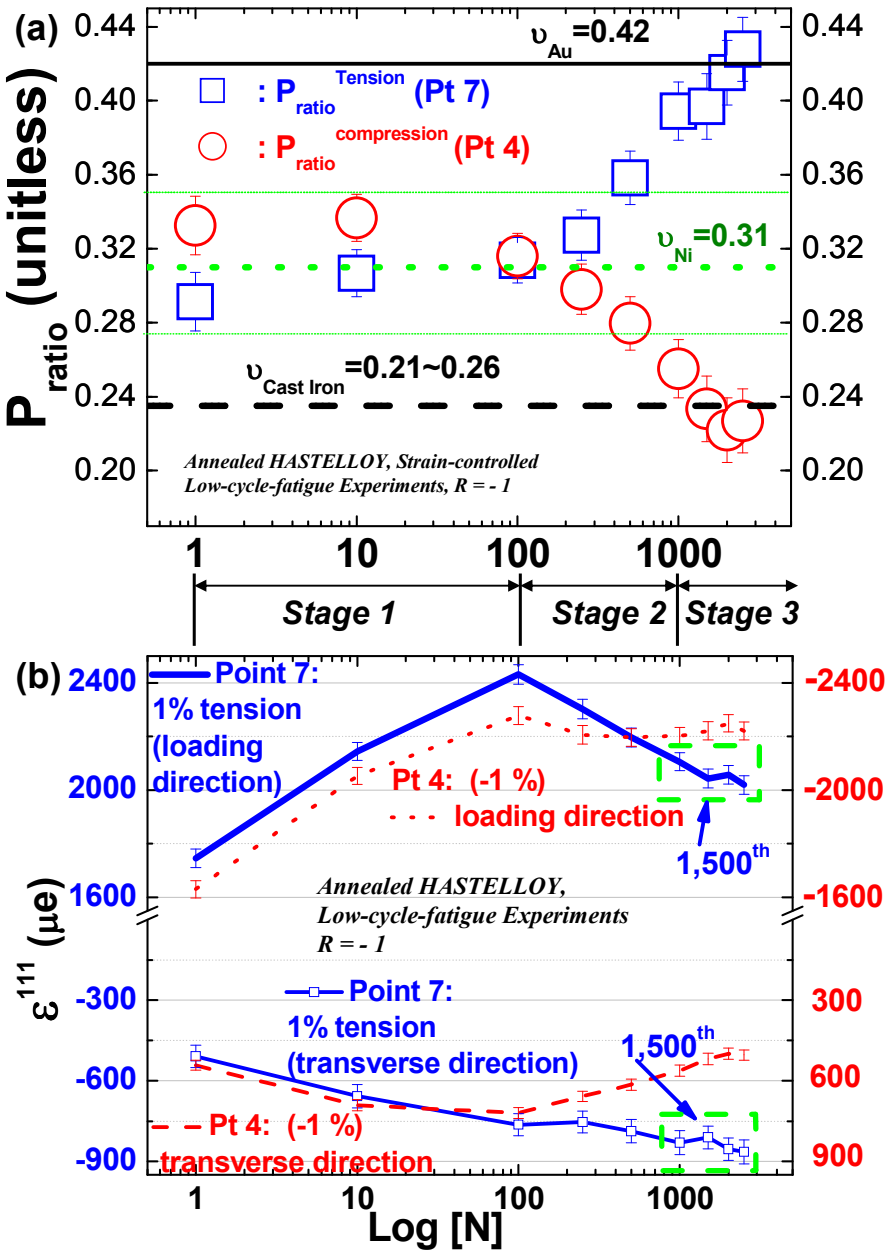


Figure 5-7. (a) The P-ratio of the tension ($P_{Tension}$: □) and compression ($P_{Compression}$:○), respectively. The Poisson ratio of Ni ($\nu_{Ni} = 0.31$), Au ($\nu_{Au} = 0.42$), and Cast Iron ($\nu_{Cast\ Iron} = 0.235 \pm 0.025$) are marked in green dot, black solid, and black dashed lines, respectively (Kumar *et al.* 2003). (b) The *{111}-lattice-strain* (ε^{111}) evolution of tension and compression in both loading and transverse directions.

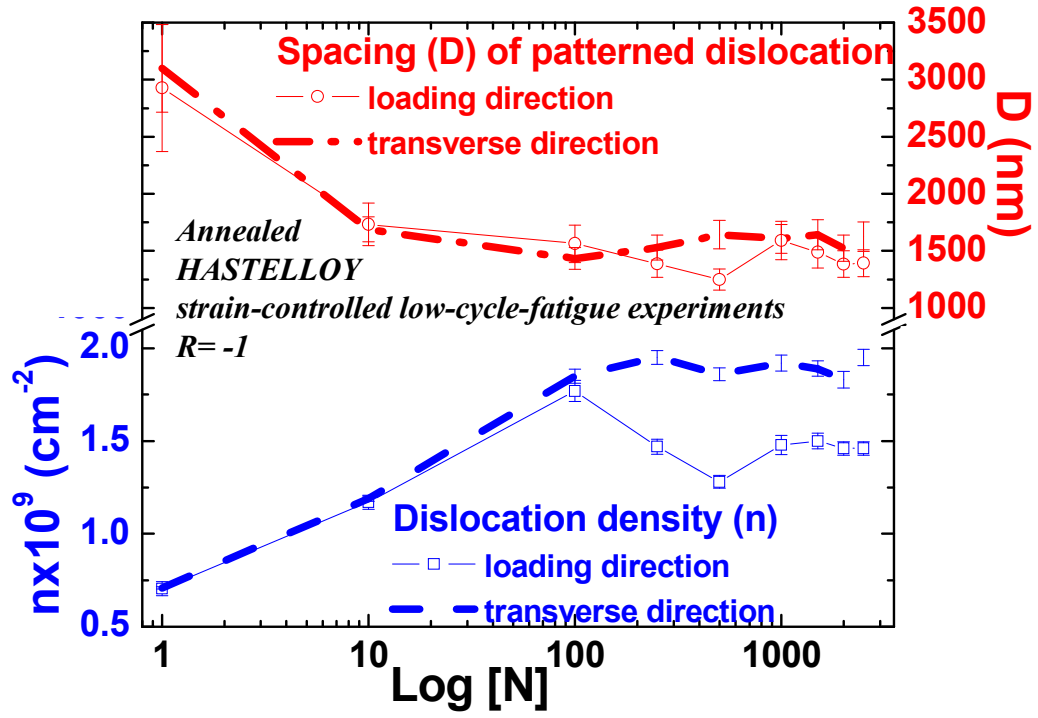


Figure 5-8: Dislocation-structure development. (a) The TEM of the specimen before cyclic loading. The randomly-distributed dislocations are depicted in the inset. (b) TEM of the patterned-dislocation structures and the randomly-distributed-dislocation interiors. The inset shows D is the spacing between the patterned-dislocation structures. (c) In-situ neutron-diffraction results: upper part: the evolution of the patterned-dislocation-structure size (D) in loading (open circle) and transverse directions (dashed-and-dotted line). Bottom: the density of the randomly-distributed dislocation (n) in the loading (open squares) and transverse (dashed line) directions.

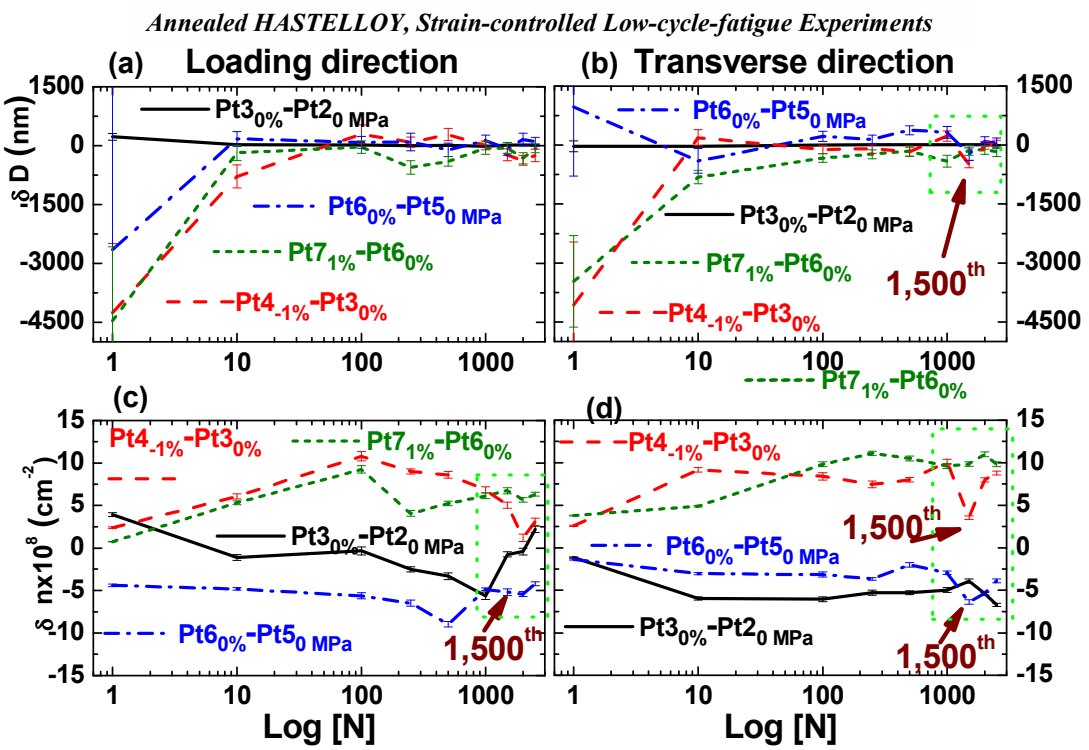


Figure 5-9: The dislocation-parameters fluctuation along the four paths within one fatigue cycle. Compression from zero stress (*Pt 2*) to zero strain (*Pt 3*): black solid lines; (2) Compression from zero strain (*Pt 3*) to maximum compression (*Pt 4*): red dashed lines; (3) Tension from zero stress (*Pt 5*) to zero strain (*Pt 6*): blue dashed-and-dotted lines, and (4) Tension from zero strain (*Pt 6*) to maximum tension (*Pt 7*): green dotted lines. (a) and (b): Fluctuations of the differential patterned-dislocation-wall-structure size (δD) in loading and transverse directions, respectively. (c) and (d): Fluctuations of the differential dislocation-density (δn) in loading and transverse directions, respectively.

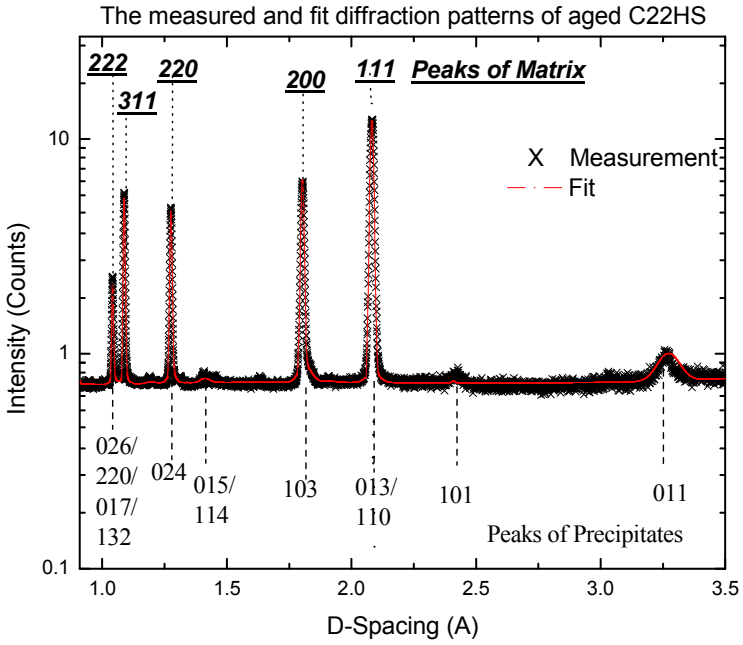


Figure 6-1: The Rietveld fitting of the neutron-diffraction patterns in the axial direction demonstrating that the undeformed alloy has two phases: f.c.c. matrix and Ni_2Mo precipitates. The peaks labeled in the upper part are the matrix diffraction peaks and the others labeled in the bottom part are the precipitates diffraction peaks.

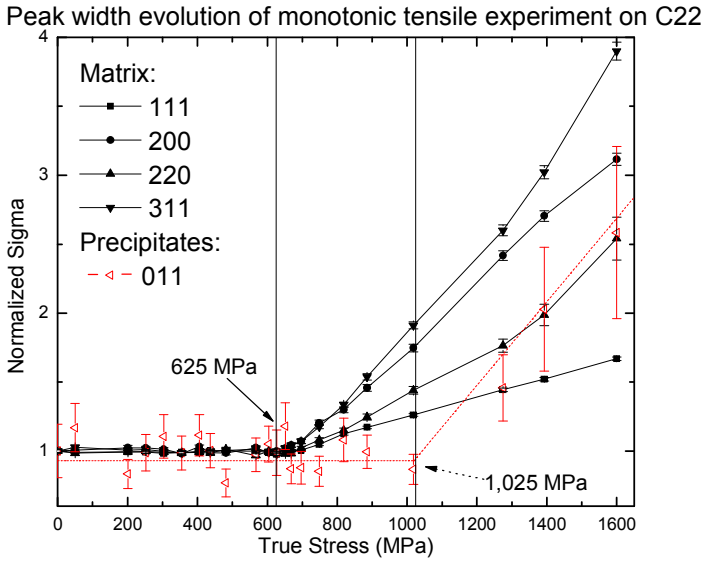


Figure 6-2: The peak-width evolution as a function of the true stress. The peak-widths of the matrix started to deviate around 0.2 % strain at 625MPa, where the plastic deformation began. The superlattice peak-width kept steady until 1,025 MPa, which indicates the density of the dislocation start to increase within the nano-precipitates at 1,025MPa.

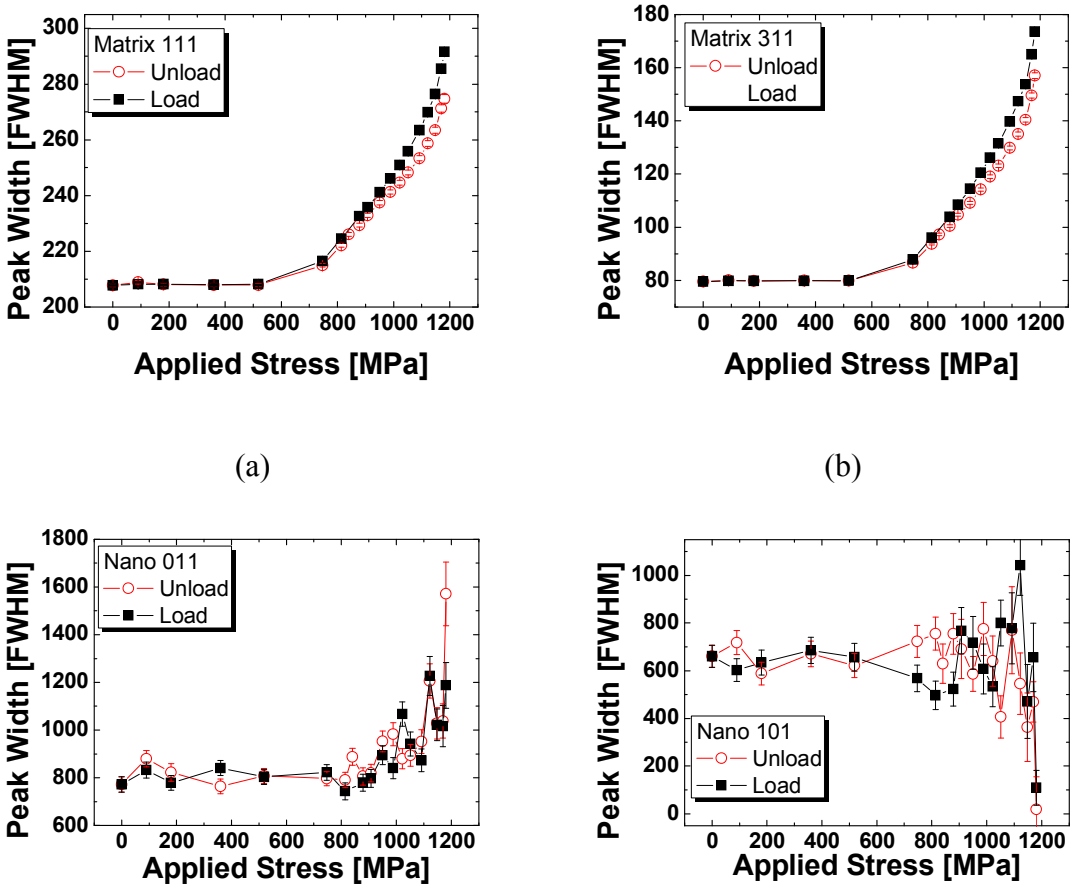


Figure 6-3: The peak-width evolution as a function of applied stress upon loading (in black solid square) and unloading (in red empty circle) of the matrix-peak [111] (a) and [311] (b) and the precipitate-peak [011] (c) and [101] (d), which are identified in Figure 6-1.

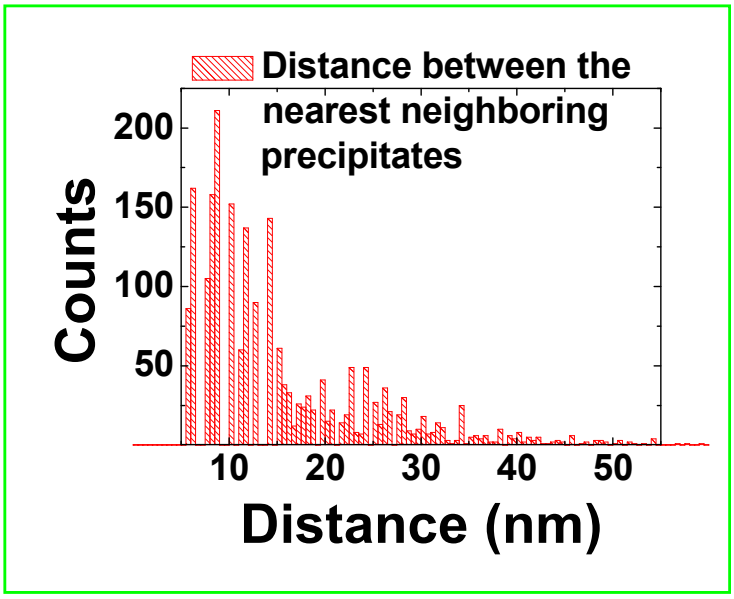


Figure 6-4: The distribution of the closest distance between the neighboring precipitates.

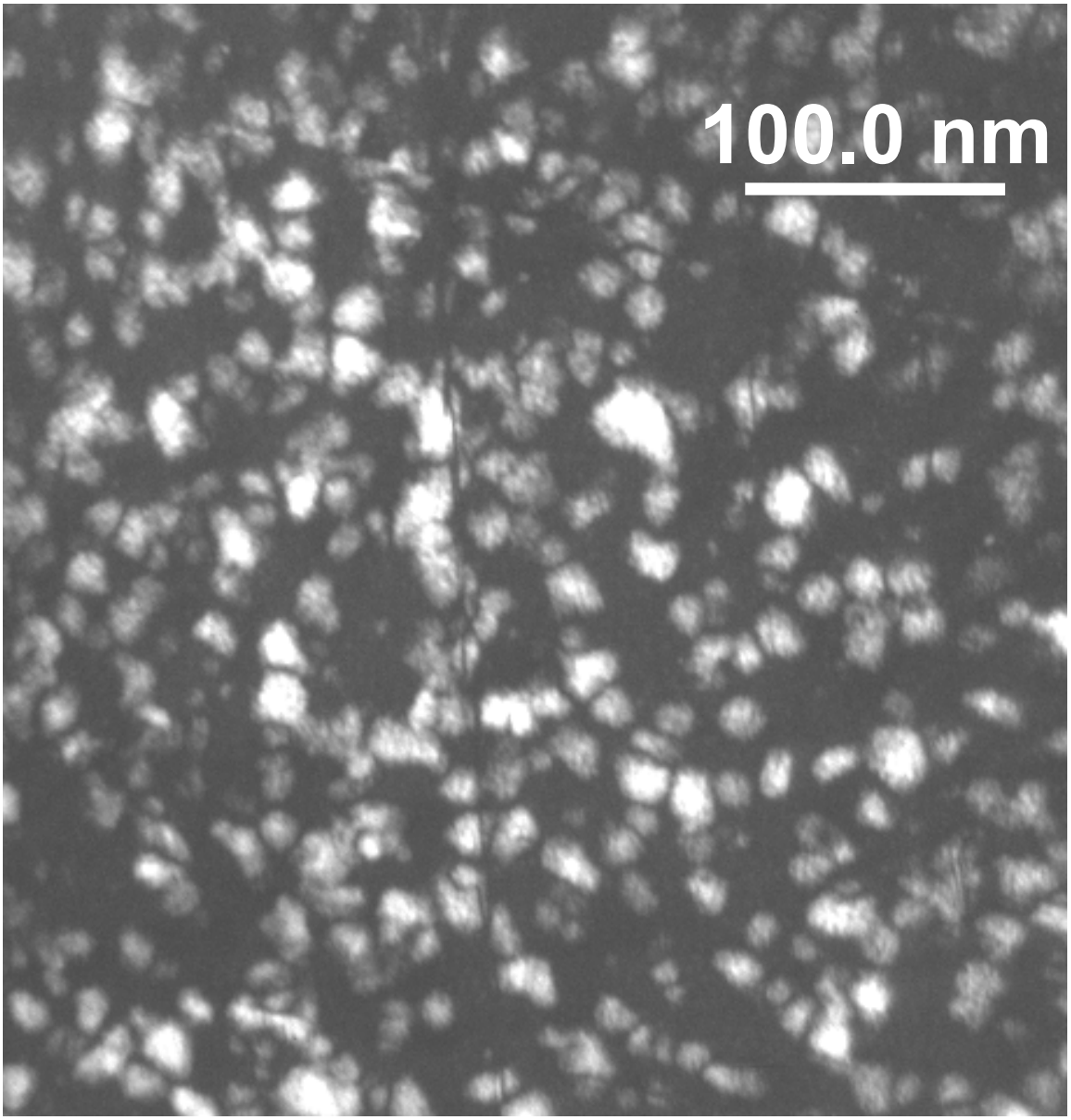


Figure 6-5: The dark-field-TEM results from the plastically-deformed specimen.

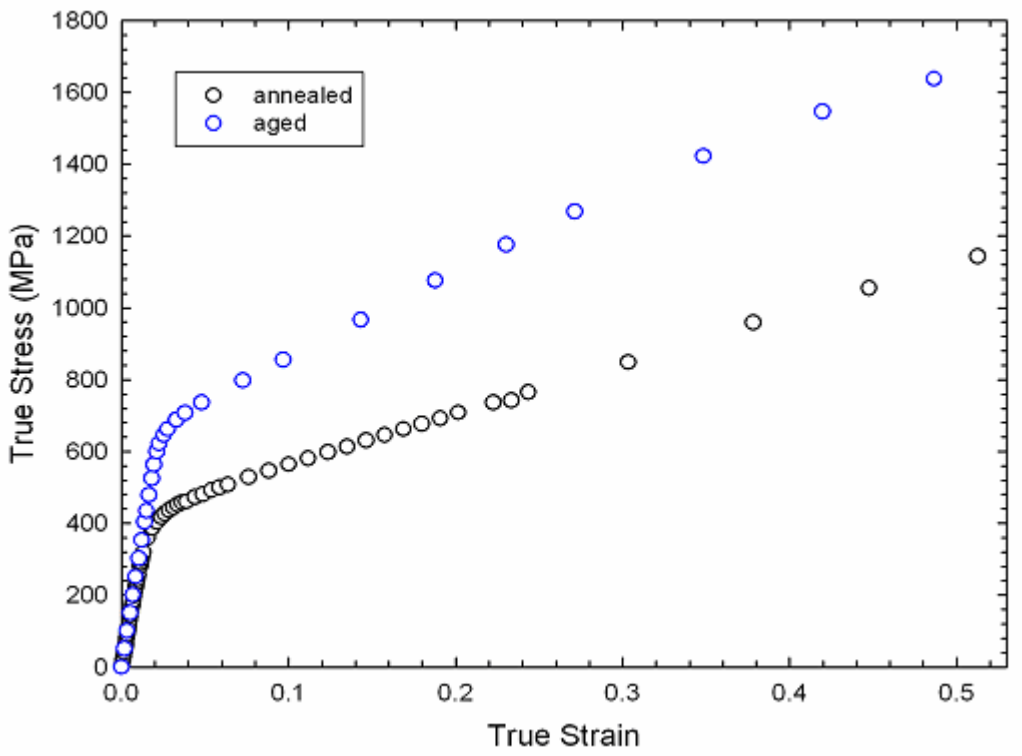


Figure 6-6: The true stress-strain curves of the annealed (in black) and the aged (in blue) samples. The monotonic tension experiment was carried out at room temperature with the strain rate at 0.001 /sec.

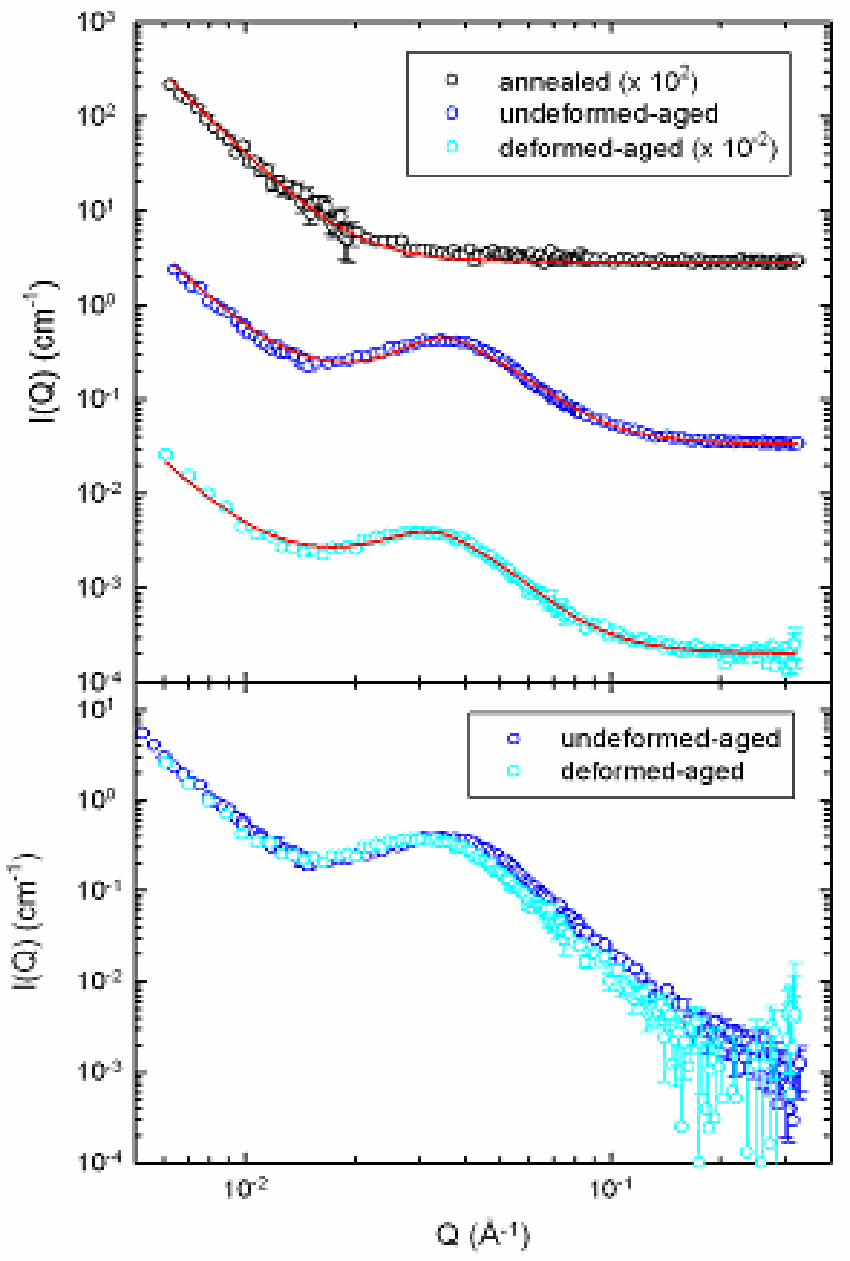


Figure 6-7: Top Panel: The SANS intensity distribution obtained from the annealed sample (black), the undeformed-aged sample (blue), and the 30%-elongated, deformed-aged sample (cyan) and fits (red lines). The curves have been displaced for the sake of better visibility. Bottom Panel: The coherent scattering obtained from the undeformed-aged sample (blue) and deformed-age sample (cyan).

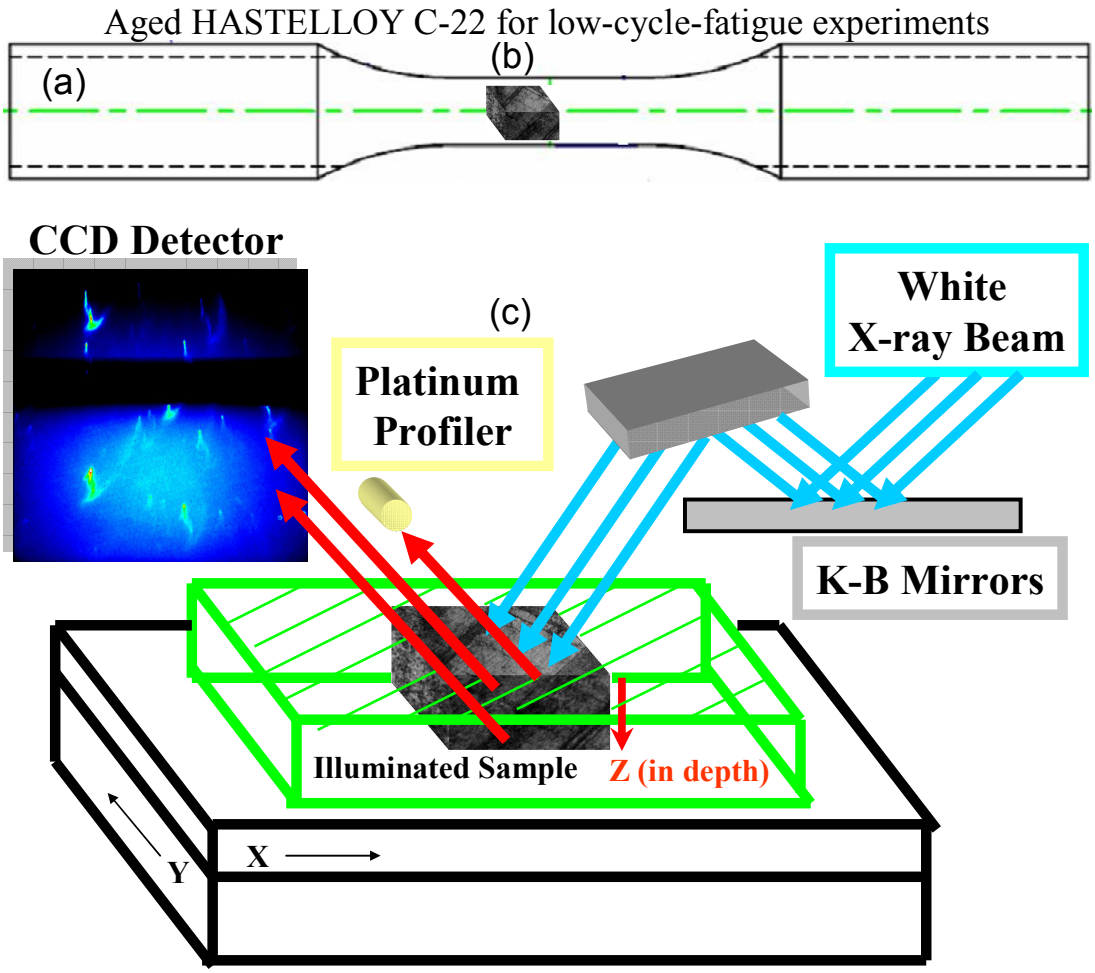


Figure 7-1: (a) The specimen for low-cycle-fatigue experiments. (b) The PXM specimen prepared in the middle of the specimen. (c) The geometry of the PXM measurements: a white X-ray microbeam collimated by K-B mirrors illuminates a deformed specimen on a sample holder. The holder can move in three-axis for framing the 3-dimnsional information. The Bragg diffraction from the sample is registered at the CCD area detector. A Pt wire profiler is controlled with a submicrometre step to resolve the spatial resolution

Aged HASTELLOY C-22 for low-cycle-fatigue experiments

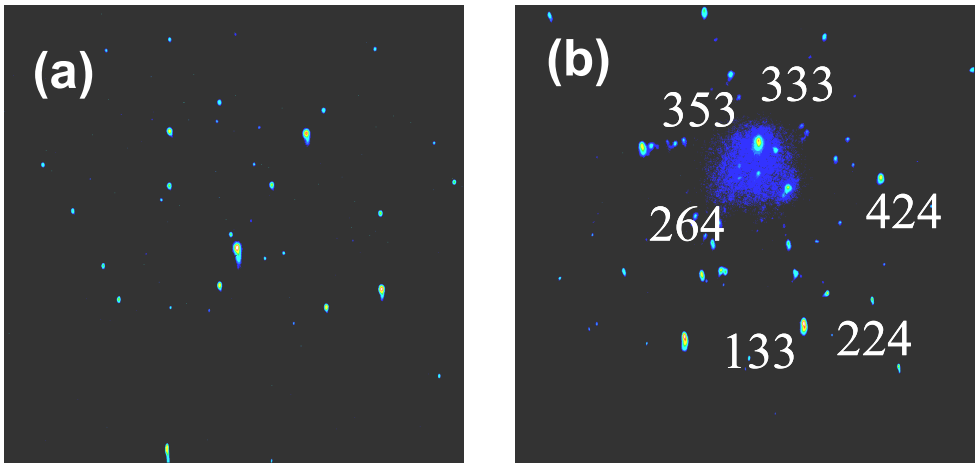


Figure 7-2: The Laue patterns (a) before and (b) after cyclic deformation.

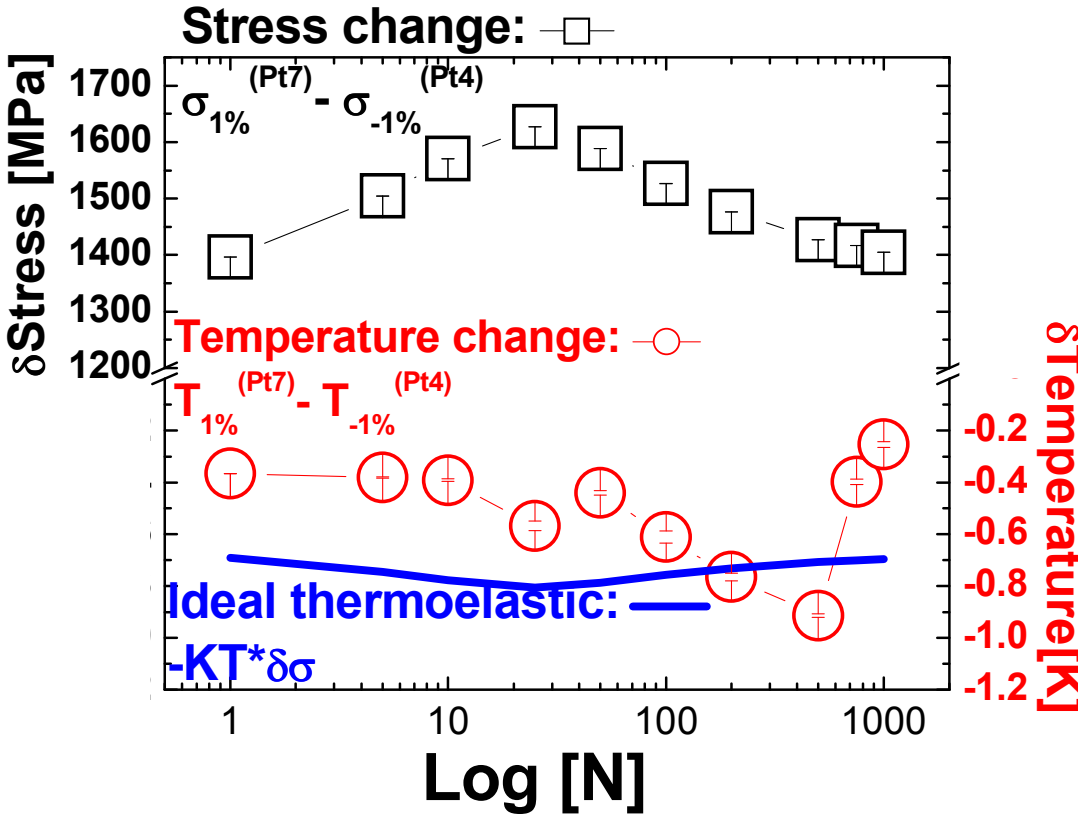


Figure 7-3: The bulk-parameter evolution. The changes from the maximum compression (*Pt 4*) to tension (*Pt 7*). Upper: stress differential of Pts 4 and 7 ($\delta\sigma$) in MPa within one fatigue cycle. Bottom: temperature differential (δT) in K. There are 2 non-monotonic temperature transitions at the 25th and the 500th cycles, respectively.

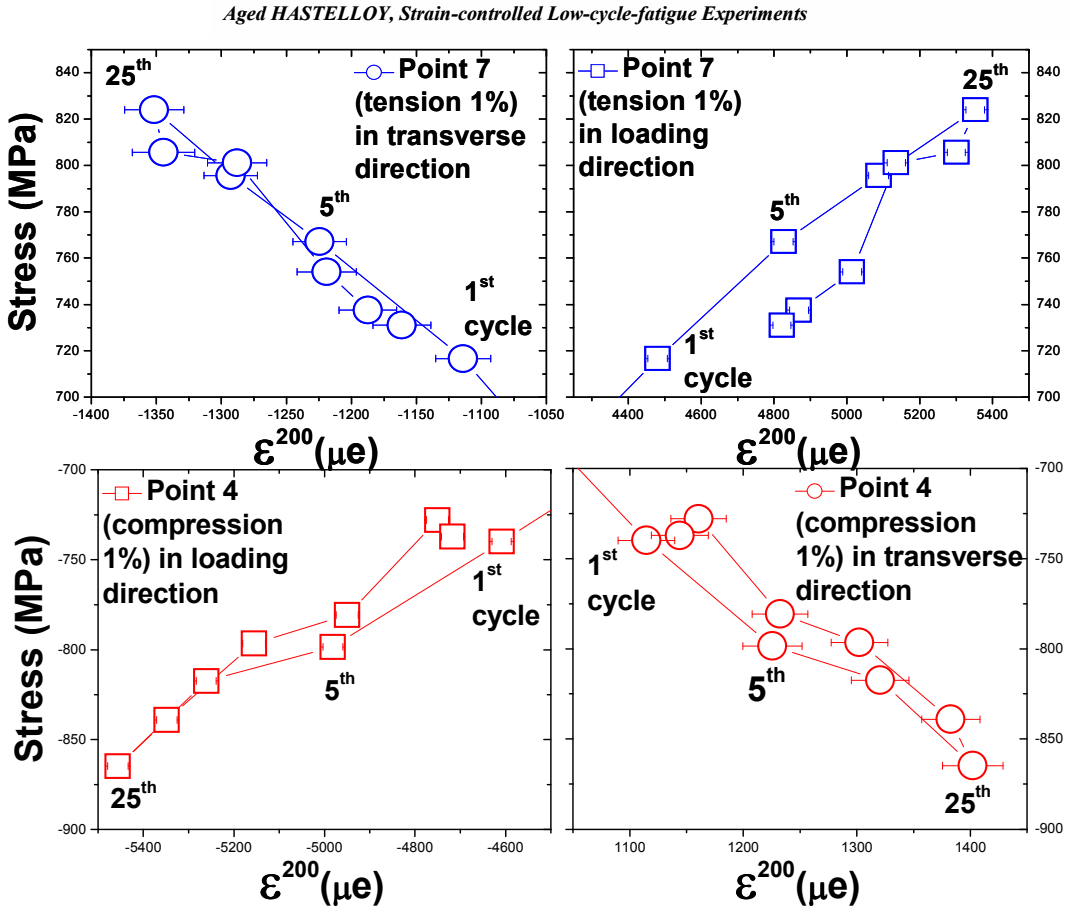


Figure 7-4: The matrix-{200} lattice strain (ε^{200}) -stress curves of the maximum tension (*Pt 7*) and compression (*Pt 4*) in loading and transverse directions, respectively. (a) $\varepsilon^{200}_{tension}$ in transverse direction. (b) $\varepsilon^{200}_{tension}$ in loading direction. (c) $\varepsilon^{200}_{compression}$ in loading direction. (d) $\varepsilon^{200}_{compression}$ in transverse direction.

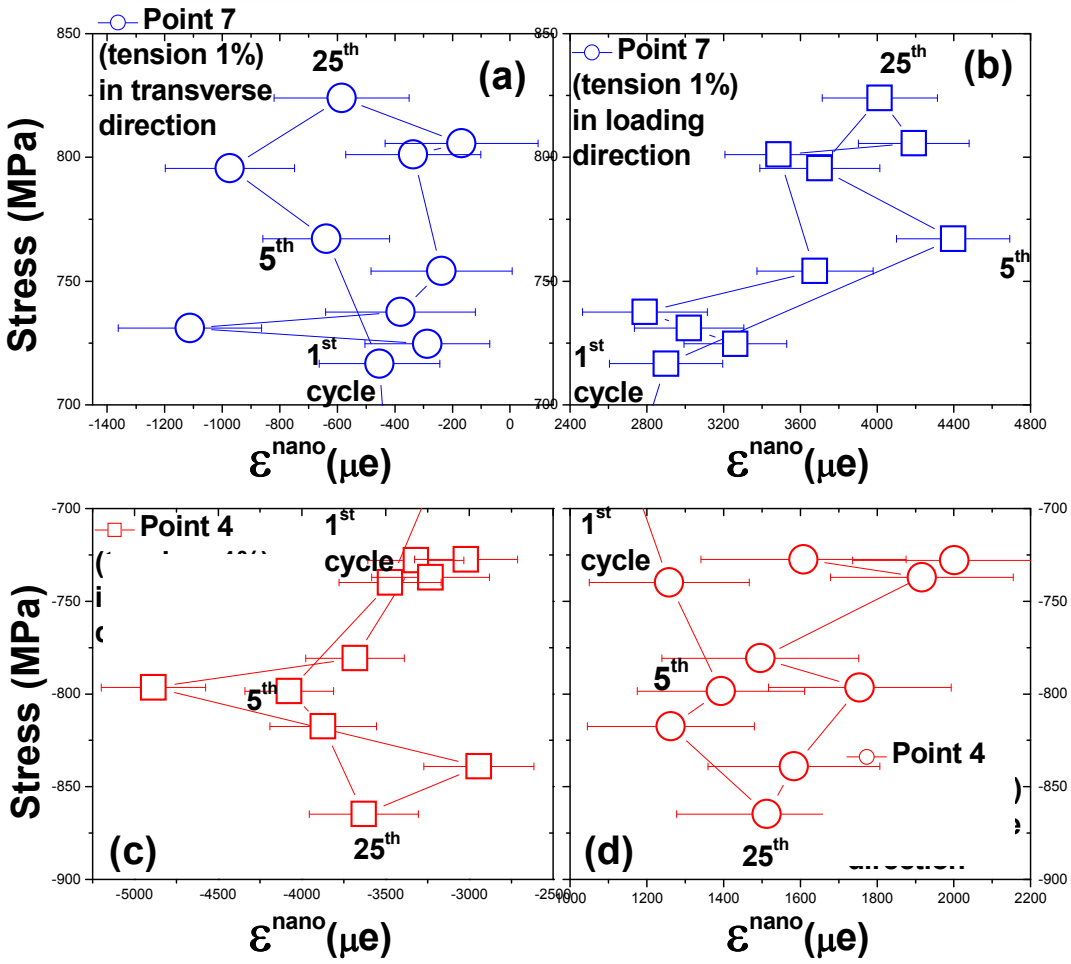
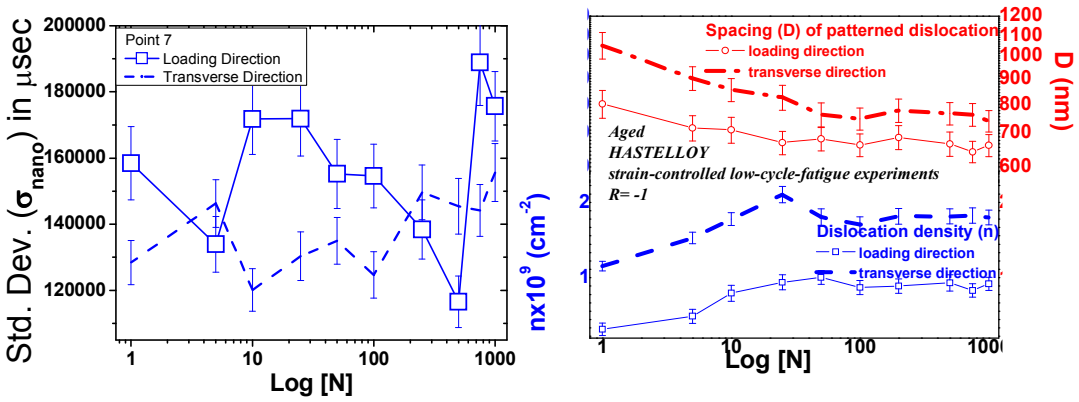


Figure 7-5: The precipitate-*{011}* lattice strain (ε^{nano}) -stress curves of the maximum tension (*Pt 7*) and compression (*Pt 4*) in loading and transverse directions, respectively. (a) ε^{nano} in transverse direction. (b) ε^{nano} in loading direction. (c) ε^{nano} in loading direction. (d) ε^{nano} in transverse direction.



(a) (b)

Figure 7-6: Microstructure evolution: (a) peak-width evolution of the nano precipitates. (a) dislocation-structure development of the matrix: the evolution of the patterned-dislocation-structure size (D) in loading (open circle) and transverse directions (dashed-and-dotted line). Bottom: the density of the randomly-distributed dislocation (n) in the loading (open square) and transverse (dashed line) directions.

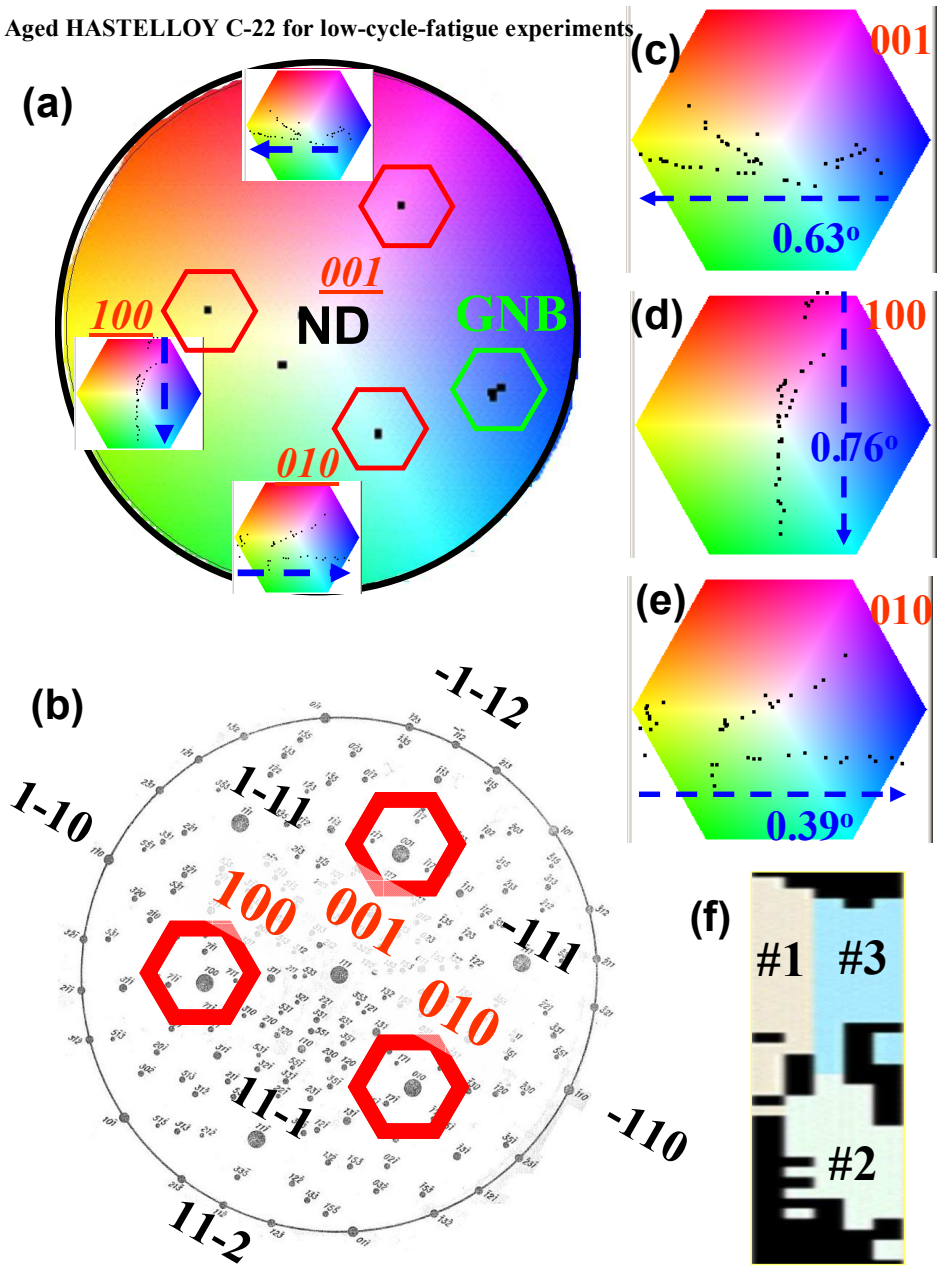


Figure 7-7: (a) reconstructed pole figure; (b) the Ewald's sphere with the (001),(010) and (100) poles; (c),(d),(e) the enlarged regions of the pole figures showing the orientation distribution around 001, 100, 010 poles;. (f) the reconstructed real space map showing the locations of the 3 probed grains.

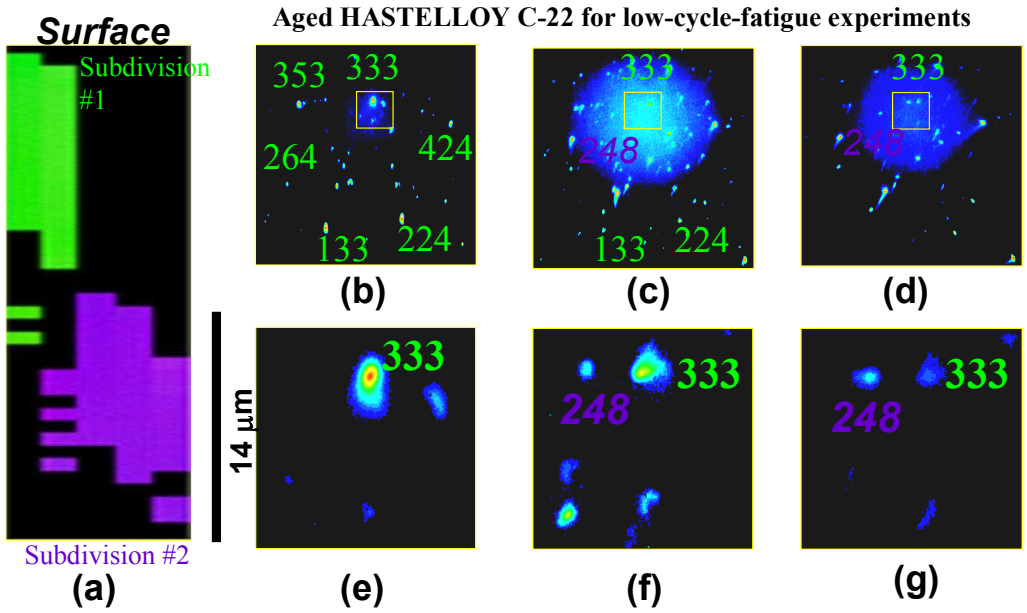


Figure 7-8: (a) The reconstructed contour map showing location of the GNB corresponding. Laue patterns from (b) grain subdivision 2, (c) boundary region between subdivisions 1 and 2, and (d) subdivision 2; enlarged regions around the centers of the Laue patters, (b), (c), and (d) are shown in (e), (f), (g), respectively.

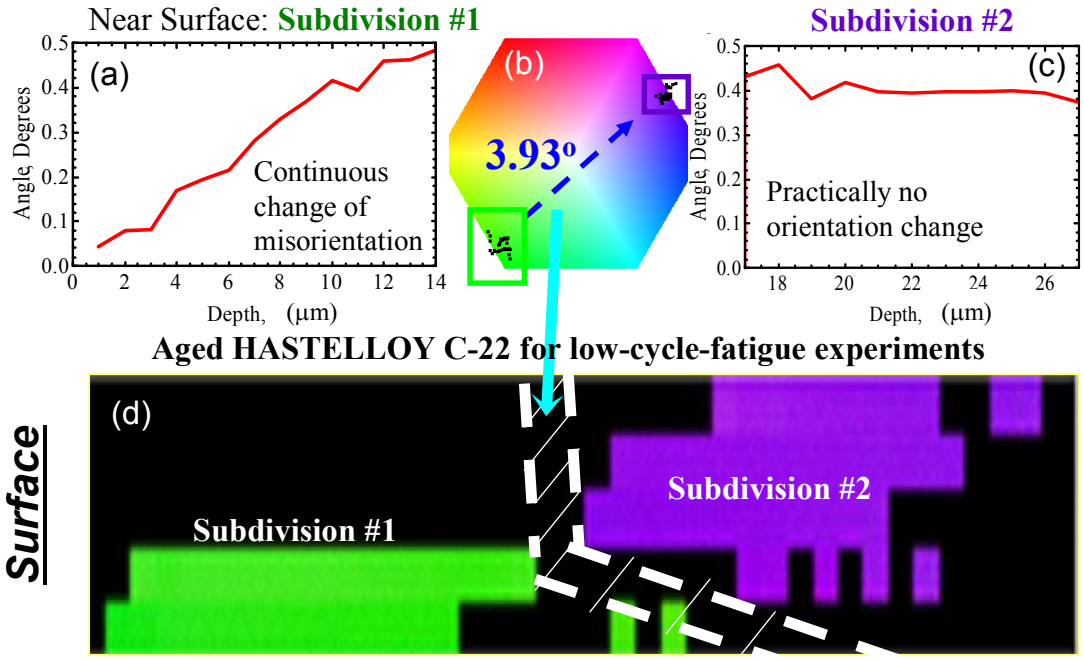


Figure 7-9: (a) Depth-dependent lattice rotations in subdivision 1. (b) the reconstructed pole figure from the boundary region. (c) depth-dependent angle evolution in subdivision 2. (d) the reconstructed real-space map of the two subdivisions.

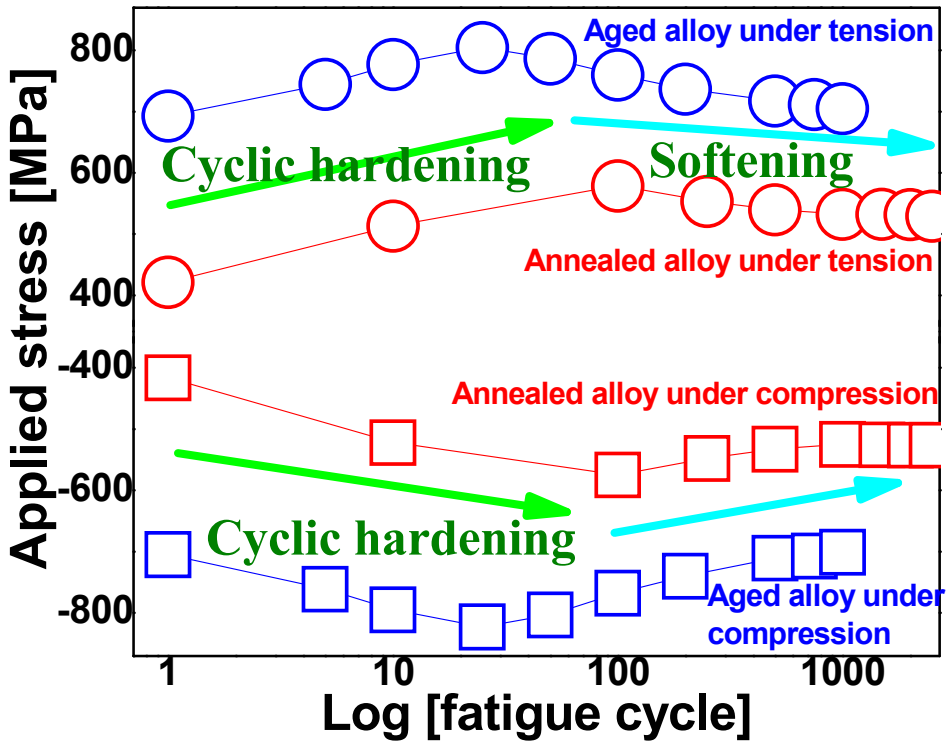


Figure 8-1: Cyclic hardening and softening are seen in both tension and compression of the annealed (red) and the aged (blue) alloys. The transitions are the 100^{th} and the 25^{th} cycles of the annealed and the aged alloys, respectively.

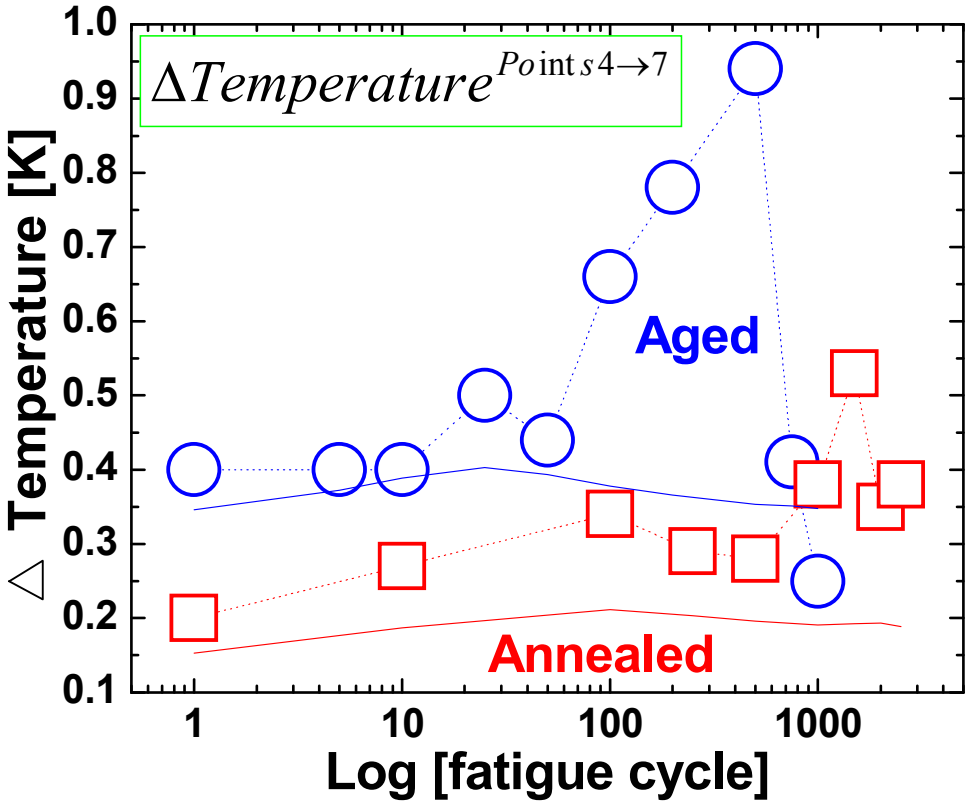


Figure 8-2: The two temperature transitions are seen in both of the annealed (red) and the aged (blue) alloys. The first transitions of both alloys correspond to the cyclic hardening-softening transitions as the 25th and the 100th, respectively. The second transitions have greater levels during the greater fatigue cycles. The calculated temperature responses (based on Equation 8-2) are blue (aged) and red (annealed) lines, respectively.

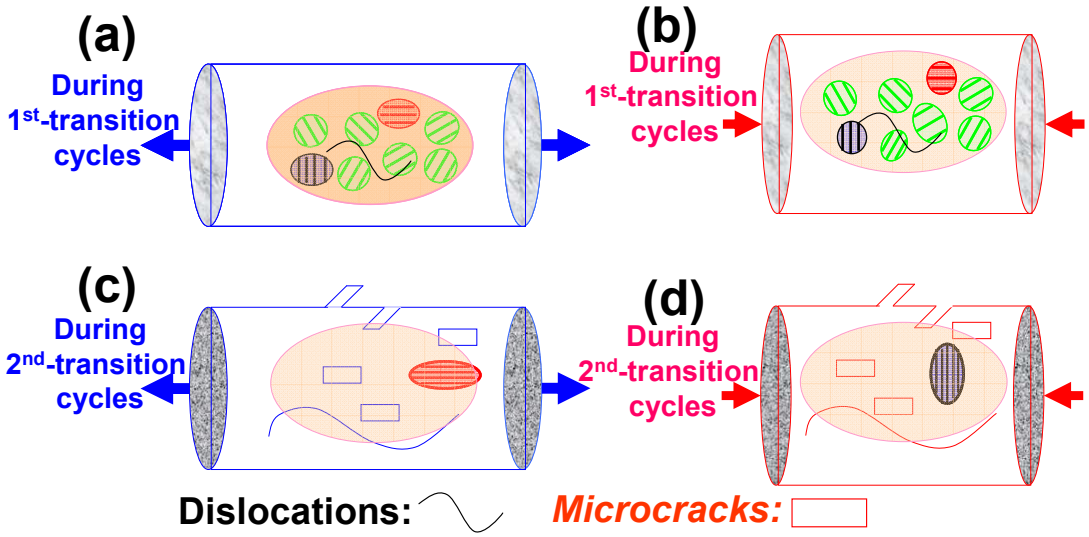


Figure 8-3: The fatigue damages are illustrated with the dislocations (curved lines) and microcracks (hollow squares). (a) and (b): the specimen in the first-transition cycles under tension and compression, respectively. (c) and (d): the second transition cycles under tension and compression, respectively.

Vita

E-Wen Huang was born in Taipei City, Taiwan. He graduated from Taipei Municipal Jianguo High School. He entered the Chang Gung University and graduated with a Bachelor of Science in Chemical Engineering. After performing his obligatory army service as a second lieutenant, he studied Materials Science and Engineering at the National Dong Hwa University under Dr. Ming-Show Wong. Dr. Yeong-Der Yao co-advised his master-thesis research at the Institute of Physics, Academia Sinica. He received a Master of Science with the Phi Tau Phi Scholastic Honor. Between 2003 and 2005, he majored in Industrial Engineering at the Texas A&M University in College Station and graduated with a Master of Engineering degree. He subsequently entered the University of Tennessee (UT) as a Ph.D. student in the Department of Materials Science and Engineering under Dr. Peter K. Liaw. In 2009, he received the Graduate Student Award for Excellence in Research from Dr. George Pharr, at the Materials Science & Engineering Honors Banquet at UT. Upon finishing his doctorate in Materials Science and Engineering, he will join the National Central University, Taiwan.